# Mechanics of the invasion of plasmodium falciparum merozoites into human erythrocytes


Thesis presented by

**Chimwemwe Msosa**

for the degree of

DOCTOR OF PHILOSOPHY

In the Department of Human Biology

UNIVERSITY OF CAPE TOWN

September 2022

Supervisor

Professor Thomas Franz

# Declaration

I, Chimwemwe Msosa, declare that this thesis titled ‘Mechanics of invasion of Plasmodium falciparum merozoites into human erythrocytes’ and the work presented in it is my own. I confirm that this work was done wholly or mainly while in candidature for a doctoral research degree at this University. I know the meaning of plagiarism and declare that all the work in the document, save for that which is properly acknowledged, is my own. I confirm that neither the whole work nor any part of it is being or is to be submitted for another degree in this or any other university. Where I have consulted the published work of others or included collaborative work, this is always clearly attributed.

CHIMWEMWE MSOSA

# Acknowledgements

I want to acknowledge and give my warmest thanks to my supervisor (Professor Thomas Franz), for his continuous support of my PhD study, for his patience, motivation, enthusiasm, and immense knowledge. His guidance and advice carried me through all the stages of writing this thesis.

Besides my supervisor, I would like to thank Dr Tamer Abdalrahman for his advice and Professor Kelly Chibale for welcoming me to his research group and group meetings which helped in defining this research project. My sincere thanks goes to Professor Kelly Rogers for the insightful comments and the hard questions. I would also like to thank all Staff and Postgraduate students at the University of Cape Town in the Division of Biomedical Engineering for making my research work enjoyable and for your brilliant comments and suggestions; many thanks to you.

I thank the National Research Foundation (NRF) of South Africa and the World Bank Staff Development Program for the research funding that made this PhD research study possible.

I would also like to give special thanks to my late Mother (Evelyn Msosa) and my family as a whole for their continuous support and understanding when I was undertaking this research project. Your prayers sustained me this far. Finally, I would like to thank God for his guidance day by day.

# Abstract

The invasion of the erythrocyte by malaria merozoites marks the pathogenesis of malaria. The invasion involves biomechanical interactions whereby the malaria merozoite exerts an actomyosin based force to push itself into the erythrocyte while inducing biochemical damage of the erythrocyte membrane, thus optimising its invasion efficiency. The mechanical aspects of invasion have received limited attention, limiting the mechanistic understanding of the invasion process. Studying the factors that impact the erythrocyte invasion mechanics experimentally may be challenging because of the need to replicate the in vivo conditions. In silico studies are a more accessible alternative to investigate the biomechanical aspects of the malaria merozoite's invasiveness. Hence this study aimed (i) to analytically and computationally investigate the mechanical factors that determine the invasiveness of a malaria merozoite during its entry into an erythrocyte, and (ii) to evaluate the impact of local membrane damage on an erythrocyte's regional and global mechanical properties, towards cell mechanics profiling of invasion blocking anti-malarial compounds that target erythrocyte membrane damage mechanism.

An analytical model based on the shell theory was developed to predict erythrocyte membrane mechanics during malaria merozoite wrapping. Equilibrium and governing equations were derived from membrane deformation and constitutive equations and solved using the Runge Kutta fourth-order method to obtain erythrocyte membrane principal stretch for determining erythrocyte membrane strains and stresses. The developed analytical model predicted the maximum indentation force of 1 pN and 8.5 pN for small and finite areal strain, respectively.

An erythrocyte membrane damage model was developed to investigate the impact of the malaria merozoite induced damage on the merozoite's invasiveness. The damage model incorporates a damage variable function into the Mooney Rivlin constitutive law for finite element analysis implementation. The model parameterises the duration and amount of erythrocyte membrane damage to allow a detailed evaluation of the impact of the damage amount and duration on the merozoite's invasiveness. The stability threshold of the developed damage model, determined analytically using Drucker's stability criteria, was used to determine the damage model's validity range and assess the impact of the damage. The nominal strain stability threshold was 1.19 and 1.98 for severe and minor erythrocyte membrane damage.

A finite element invasion model was developed to investigate the malaria merozoite's invasiveness based on the erythrocyte's deformability. The invasion model comprised erythrocyte membrane and cytoplasm, malaria merozoite, and tight junction. The merozoite's invasiveness was evaluated employing the energetics of all interacting structures. The impact of erythrocyte shape and membrane damage on the merozoite invasiveness was determined. An increase in erythrocyte sphericity and membrane damage led to a decrease and increase of the merozoite's invasiveness, respectively. The model predicted that a force of 11 pN was required for the merozoite to invade the erythrocyte.

Erythrocyte membrane damage is a possible target for disrupting the invasion process and can potentially be used for screening antimalarial compounds. Erythrocyte nanoindentation and

compression was assessed in finite element simulations to identify suitable biomechanical assays for erythrocyte membrane damage. Local erythrocyte membrane damage did not discernibly affect the forces for whole-erythrocyte compression. However, the nanoindentation force decreased by 57% in the presence of erythrocyte membrane damage. Hence, nanoindentation may be a suitable mechanical assay for malaria merozoite-induced erythrocyte membrane damage in screening new anti-malarial drugs.

# Contents

# List of Figures

# List of Tables

# Nomenclature

| Symbol | Description |
|---|---|
| Ǎ | Coefficients that define the 3D shape of the malaria merozoite |
| $A_0$ | Undeformed area of the erythrocyte membrane |
| $A_p$ | Projected area of the erythrocyte membrane |
| $A_s$ | Areal strain of the erythrocyte |
| $A_{s,max}$ | Maximum areal strain of the erythrocyte |
| $A_w$ | Wrapped surface area of the malaria merozoite |
| B | Left Cauchy deformation tensor |
| c | Stretch parameter |
| $C_{01}$ | Material parameter |
| $C_{10}$ | Material parameter |
| C3D10M | Ten-node modified quadratic tetrahedron elements |
| C3D8R | 8-node linear brick elements with reduced integration and hourglass control |
| $C_j$ | Material parameters of the tight junction |
| $c_s$ | Speed of sound |
| $C_t$ | Right Cauchy deformation tensor |
| $D_{fv}$ | Damage variable for the fibres |
| $d_i$ | Indentation depth |
| $D_m$ | Diameter of the tight junction |
| $D_{mv}$ | Damage variable for the matrix |
| E | Elastic modulus |
| ē | Clearance between the tight junction and the merozoite |
| Ẽ | Coefficients that define the 3D shape of the malaria merozoite |
| $E_i$ | Parasite indentation work |
| erf | Error function |
| $e_s$ | Shear strain |
| F | Deformation gradient tensor |
| $f_{ext}$ | External force vector |

| | |
|---|---|
| $F_i$ | Parasite indentation force |
| $f_i$ | Field function |
| $F_m$ | Objective function |
| $F_w$ | Parasite wrapping force |
| G | Coefficients that define the 3D shape of the malaria merozoite |
| $G_s$ | Shear modulus |
| h | Smoothing length |
| $h_t$ | The thickness of the erythrocyte membrane |
| $I_1$ | First strain invariant |
| $I_2$ | Second strain invariant |
| $I_i^J$ | Internal force vector |
| K | Compressibility of the erythrocyte membrane |
| $K_0$ | Initial bulk modulus |
| $k_1$ | Meridian curvature |
| $k_2$ | Circumferential curvature |
| m | Stretch parameter |
| $M_c$ | The coverage area of the erythrocyte membrane |
| $M_d$ | Width of the merozoite at the maximum indentation depth |
| $M^{NJ}$ | Mass matrix |
| $m_p$ | Material parameters for implementing the Mullin's effect |
| MR-$T_1$ | Meridian tension obtained using the Mooney Rivlin law |
| MR-$T_2$ | Circumferential tension obtained using the Mooney Rivlin law |
| $M_{st}$ | Structural tensors |
| n | Stretch parameter |
| N | Number of SPH particles |
| $N_{st}$ | Structural tensors |
| P | The pressure acting on the erythrocyte surface |
| $P_i^J$ | Applied load vector |
| R | Rotation matrix |
| R3D3 | Linear rigid triangular shell elements |
| $R_a$ | Malaria merozoite shape parameter |
| $R_b$ | Malaria merozoite shape parameter |

| | |
|---|---|
| $R_c$ | Relative compressibility |
| $R_d$ | Reduction factor |
| $r_i$ | The position vector of the particle of interest |
| $r_j$ | Particle's position vector in the neighbouring region |
| $r_m$ | The radius of the circular erythrocyte membrane |
| $r_p$ | Material parameters for implementing the Mullin's effect |
| S3R | Triangular shell elements with reduced time integration |
| $S_h$ | The entropy of the system |
| $T_1$ | Principal meridian tension |
| $T_2$ | Principal circumferential tension |
| $T_h$ | The absolute temperature of the system |
| U | Stretch tensor |
| $U_h$ | The internal energy of a system |
| $u^N$ | N degrees of freedom |
| $U_p$ | Particle velocity |
| $U_s$ | Shock velocity |
| v | Velocity |
| $V_0$ | Reference volume |
| x | x coordinate point on the surface of the malaria merozoite |
| y | y coordinate point on the surface of the malaria merozoite |
| z | z coordinate point on the surface of the malaria merozoite |
| $\beta$ | The ratio of material parameters |
| $\beta_1$ | Chemical damage parameter |
| $\beta_2$ | Strain or mechanical damage parameter |
| $\beta_3$ | Scaling parameter for the strain energy density function of the intact material |
| $\beta_p$ | Material parameters for implementing the Mullin's effect |
| $\Gamma$ | Linear coverage of the erythrocyte membrane |
| $\Gamma_c$ | Arch length on the malaria merozoite surface |
| $\Delta$ | Dimensionless parameter |
| $\delta$ | Kronecker delta function |
| $\eta$ | Damage variable for Mullin's effect |

| | |
|---|---|
| $\eta_m$ | Nominal volumetric compressive strain |
| $\theta$ | Polar angle for determining the shape of the merozoite |
| $\lambda_1$ | Meridian principal stretch |
| $\lambda_{1,max}$ | Maximum stretch in the meridian direction |
| $\lambda_2$ | Circumferential principal stretch |
| $\lambda_{2,max}$ | Maximum stretch in the circumferential direction |
| $\mu$ | Dynamic viscosity |
| $\mu_0$ | Initial shear modulus |
| $\mu_s$ | Shear stress |
| $\nu$ | Poisson's ratio |
| $\Xi_k$ | The strain energy of the intact material |
| $\xi_k$ | Material parameter |
| $\Xi_{max}$ | The maximum strain energy of the intact material |
| $\Xi_{min}$ | The minimum strain energy of the intact material |
| $\rho$ | The polar coordinate point on the surface of the malaria merozoite |
| $\rho_0$ | The initial polar coordinate point on the surface of the malaria merozoite representing a point at which the tight junction forms |
| $\sigma_1$ | Principal meridian stress |
| $\sigma_2$ | Principal circumferential stress |
| $\tau$ | Indentation time in seconds |
| $\varphi$ | Polar angles for determining the shape of the merozoite |
| $\varphi_d$ | Damage function for the Mullin's effect |
| $\psi_0$ | The strain energy density of an intact erythrocyte membrane |
| $\psi_{0f}$ | The strain energy density of intact fibres |
| $\psi_{0m}$ | The strain energy density of the intact matrix |
| $\psi_{dev}$ | Deviatoric strain energy |
| $\psi_h$ | Helmholtz free energy function |
| $\psi_m$ | The strain energy density of the tight junction |
| $\psi_{max}$ | Maximum strain energy |
| $\psi_{vol}$ | Volumetric strain energy density |

# List of Abbreviations

| | |
|---|---|
| 2D | Two dimensions |
| 3D | Three dimensions |
| ADP | Adenosine diphosphate |
| AFM | Atomic force microscopy |
| ATP | Adenosine triphosphate |
| CDM | Continuum damage mechanics |
| DNA | Deoxyribonucleic acid |
| EBA | Erythrocyte binding antigen |
| EBL | Erythrocyte binding like |
| EMD | Erythrocyte membrane damage |
| FE | Finite element |
| FEA | Finite element analysis |
| GPA | Glycophorin A |
| GPC | Glycophorin C |
| HS | Horgan and Saccomandi |
| LLSM | Lattice light-sheet microscopy |
| MR | Mooney Rivlin |
| NH | Neo-Hookean |
| PVM | Parasitophorous vacuole membrane |
| RBL | Reticulocyte binding like |
| RNA | Ribonucleic acid |
| S/V | Surface area to volume ratio |
| SLC4A1 | Solute carrier family 4 member 1 |
| SPH | Smoothed particle hydrodynamics |
| UMAT | User material for abaqus standard analysis |
| VUMAT | User material for abaqus explicit analysis |
| WHO | World Health Organisation |

# 1 Introduction and background

## 1.1 Malaria

### 1.1.1 Pathogenesis of malaria

In 2015 World Health Organisation reported over 212 million malaria cases with an estimated 429,000 deaths, the majority of which occurred in the sub-Saharan African children (World Health Organisation 2017). Despite global efforts to eliminate malaria, the challenge of resistance to existing antimalarial drugs remains. Even with the best available treatment, severe plasmodium falciparum malaria mortality remains high.

The plasmodium falciparum parasite interacts with human host cells at several stages in its life cycle. The human to human transmission of malaria parasites occurs by a female anopheles' mosquito, which deposits Plasmodium falciparum sporozoites into the dermis of the human host skin. Sporozoites are motile cells equipped with sophisticated actomyosin machinery that allows gliding migration through dermis cells to nearby lymphatic channels or blood vessels. Once in the blood circulatory or lymph system, parasites are transported to the liver, where they infect hepatocytes, see Figure 1.

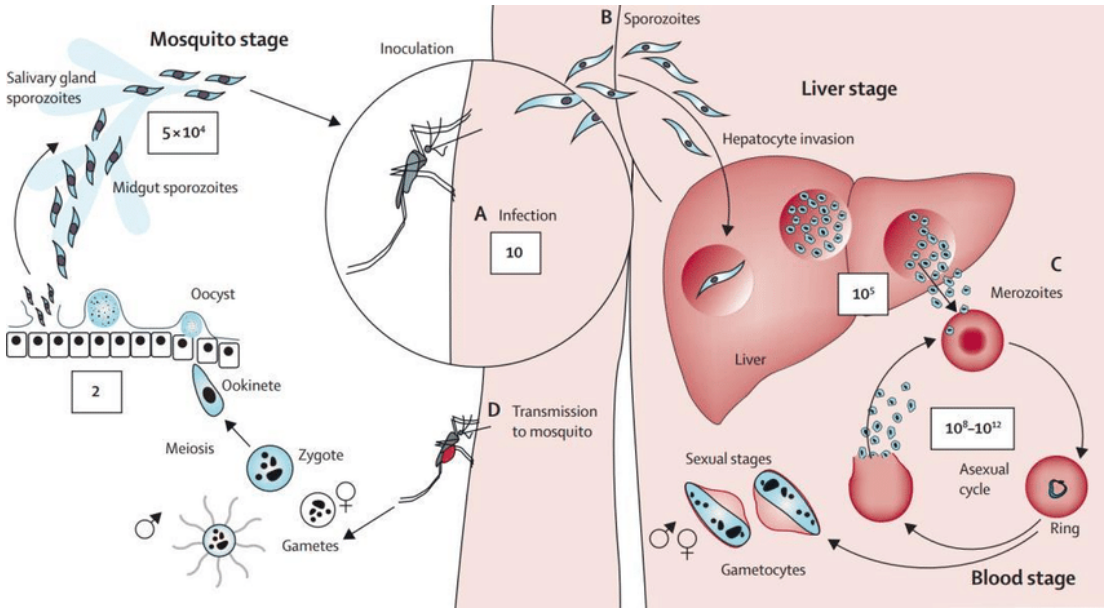


Figure 1: Life cycle of plasmodium falciparum merozoites, with permission from White *et al.* (2014).

Once inside the hepatocytes, sporozoites replicate into merozoites. This liver stage development of sporozoites is followed by the rupturing of infected hepatocytes, releasing hundreds of malaria merozoites into the bloodstream. Once in the bloodstream, infection of erythrocytes commences,

marking the pathogenesis of malaria. The intraerythrocytic developmental stage commences once the malaria parasite is inside the erythrocyte. The intraerythrocytic developmental stage is divided into two categories: asexual and sexual. Asexual development phase commences soon after the invasion process and involves the formation of trophozoite, which replicates into schizonts, which develops into merozoites. The merozoites replicate further until the erythrocyte ruptures, releasing more merozoites into the bloodstream and thus starting a new cycle of erythrocyte invasion. During this intraerythrocytic developmental stage, the malaria parasite induces signalling to manipulate and regulate various erythrocyte biochemical processes facilitating its survival. For example, the malaria parasite establishes transport channels for its nutrition, exports thousands of proteins to the host membrane surface to form adhesive knobs allowing the infected erythrocyte to sequester along the walls of blood vessels and thus escape its destruction in the spleen. The sexual intraerythrocytic development stage starts with sexually committed trophozoites that replicate into schizonts and then develop into merozoites. When sexually committed merozoites infect erythrocytes, they develop into male and female gametes, which are taken up by a female anopheles mosquito during a blood meal. Once inside the mid-gut of the female anopheles mosquito, the male and female gametes form a zygote which then develops into the Ookinete. The Ookinete develops into an Oocyst and then forms sporozoites which occupy the salivary gland of a female anopheles. Sporozoites are injected into the human host's skin during a blood meal, marking a new infection cycle.

### 1.1.2 Malaria merozoite invasion mechanics

Invasion of a human erythrocyte by a malaria merozoite starts with a low-affinity contact mediated by the merozoite surface proteins (MSP) (Harvey *et al.* 2012). As soon as the merozoite is weakly attached to the erythrocyte surface, it begins to reorient to maximize the adhesion energy (Dasgupta *et al.* 2014), which locally deforms the erythrocyte membrane and thus forming an invasion pit. Additionally, the reorientation of the merozoite also facilitates the secretion of proteins located in specialized exocytic organelles of the malaria merozoite (micronemes, rhoptries) onto the apical surface of the erythrocyte (Singh *et al.* 2010). Furthermore, the molecular interaction between the secreted erythrocyte binding antigen (EBA-175) and glycophorin antigen (GPA) (Jaskiewicz *et al.* 2019) plays a vital role in signalling the reorganisation of the erythrocyte membrane skeleton (Zuccala *et al.* 2016), achieved by phosphorylation of the key membrane skeleton proteins such as ankyrin and spectrin. The tight junction formation then follows the formation of the invasion pit. The merozoite then forms the digestive vacuole and exerts a traction force through the tight junction, causing the erythrocyte membrane to wrap around the merozoite surface. The tight junction forms a circular structure that functions as a mechanical link between the merozoite and erythrocyte membrane. This mechanical

link moves rearward during the invasion, propelling the merozoite into the host cell (Cowman and Crabb 2006) see Figure 2. Predictions from imaging studies of fixed merozoite mid-entry indicate that actomyosin force is applied consistently at or proximal to the tight junction (Riglar *et al.* 2011). In other words, the tight junction acts as a circular mechanical link transmitting the merozoite's actomyosin force to the erythrocyte membrane hence facilitating the invagination of the malaria merozoite (Koch and Baum 2016). Erythrocyte binding like ligands (EBL), erythrocyte binding antigens (EBA-175, EBA-140) and erythrocyte receptors such as glycophorin A (GPA) and glycophorin C (GPC) has been identified to mediate signalling and tight junction formation (Paul *et al.* 2015). Hence, playing a vital in regulating the invasion efficiency. The internalisation of the malaria merozoite ends with the sealing of the erythrocyte membrane.

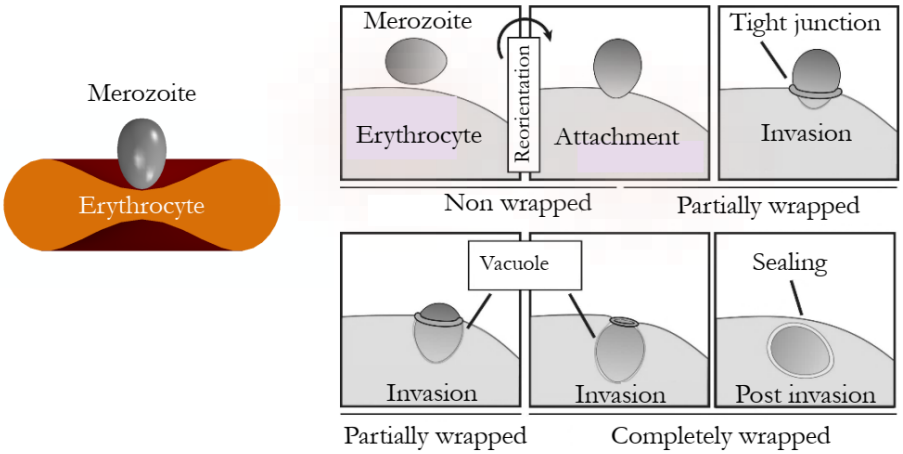


Figure 2: Illustration of invasion process by malaria falciparum merozoites Dasgupta *et al.* (2014).

The malaria merozoite takes less than 30 seconds to be internalised entirely into a human erythrocyte. Dasgupta *et al.* (2014) demonstrated that erythrocyte membrane wrapping is the primary mechanism for internalising the malaria merozoite. The authors also suggested that the malaria merozoite induced reorganisation of the erythrocyte cytoskeleton and release of malaria merozoites derived membrane can also account for a considerable energetic portion of the invasion energy. Additionally, Dasgupta *et al.* (2014) described the energy $\psi$ required by the malaria merozoite to invade the erythrocyte, and is given as follows:

$$\psi = \psi_{ben} + \psi_{mem} + \psi_{ad} + \psi_{ten} \quad (1)$$

where $\psi_{ben}$, $\psi_{mem}$, $\psi_{ad}$, $\psi_{ten}$ are energies due to bending rigidity, membrane tension, adhesion strength, and line tension, respectively. The malaria merozoite must minimise the total energy $\psi$ in Eqn. (1 to maximise the invasion efficiency of the erythrocyte. Analysing the energetics associated with the internalisation of the malaria merozoite in an in vitro experiment could be challenging and costly.

However, mathematical modelling of biomechanical interaction of the merozoite and erythrocyte can predict the force and the energy required for a successful invasion. It has been demonstrated using contact mechanics that the adhesion energy between the malaria merozoite and erythrocyte generates an indentation force that accurately corresponds to the indentation energy of the erythrocyte membrane for an indentation depth up to 10% (Abdalrahman and Franz 2017a). With all these findings, it would be an excellent idea to integrate currently separate concepts of (i) the actomyosin motor force generation, (ii) spectrin network disruption and (iii) tight junction in one mathematical model for the invasion process.

## 1.2 Structure of the human erythrocyte

The erythrocyte membrane skeleton is a repetitive 2D structure consisting of short, ~37 nm long actin filaments (composed of 12 to 14 monomers) that coordinate 5 or 6 spectrin tetramers. Accessory proteins, such as protein 4.1 and dimers of adducin, stabilise the actin-spectrin interaction. The whole structure is attached to the plasma membrane through two protein complexes that interact with the anion transport protein Band 3. At the actin-spectrin junction, the protein 4.1 complex mediates the interaction with Band 3, whereas a second link to the membrane is formed through an ankyrin complex close to the middle point of the spectrin tetramer. This arrangement of proteins forms an elastic network of proteins that underlies the lipid bilayer see Figure 3. The malaria merozoite reorganises this network by inducing phosphorylation of the erythrocyte membrane proteins (Zuccala and Baum 2011) see Figure 3 b.

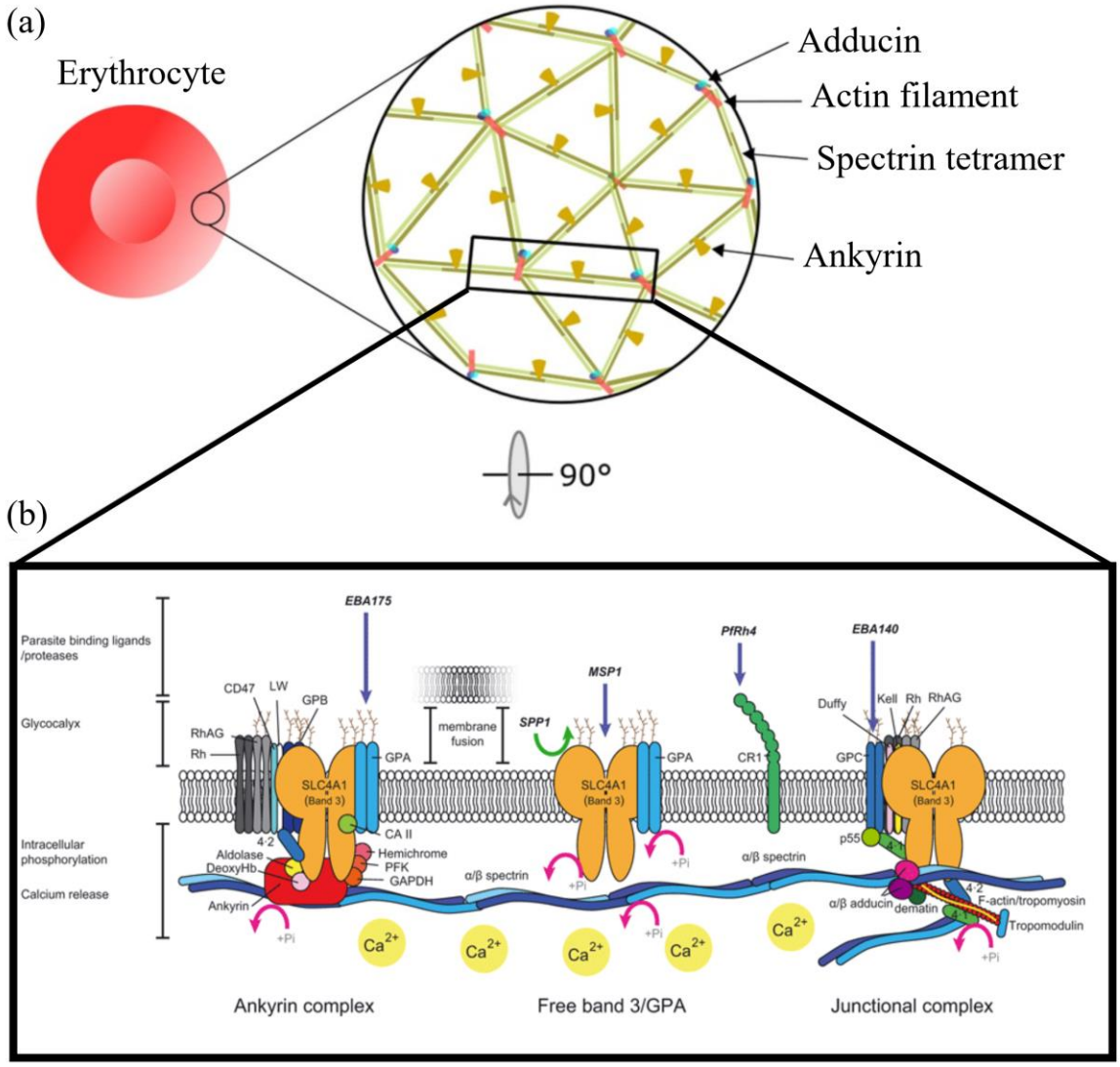


Figure 3: (a) Basic arrangement of the actin/spectrin skeleton underlying the erythrocyte lipid bilayer (Unsain *et al.* 2018) (b) erythrocyte membrane architecture showing interactions and modifications that occur during malaria merozoite invasion. Blue arrows indicate P. falciparum merozoite binding ligands and their receptors. The green arrow shows extra-cellular cleavage of SLC4A1 (Band 3) by a parasite-derived protease. Magenta arrows indicate putative erythrocyte cytoskeletal phosphorylation events that arise during the invasion. Calcium ions (known to be released during the invasion) are shown with permission from Zuccala and Baum (2011).

## 1.3 Computational mechanics of erythrocytes

### 1.3.1 Structural models

Cortical shell Newtonian liquid drop models have been previously proposed to model biological cells, including erythrocytes (Lim *et al.* 2006). Recently, this model has been adopted to develop the finite element model of erythrocyte deformation when exposed to shear load (Ida Laila Ahmad 2015). The

author modelled the erythrocyte cytoplasm as an incompressible Newtonian fluid surrounded by a thin hyperelastic membrane. Micro-structural models have also been used to represent erythrocyte structures such as the erythrocyte spectrin network (Fai *et al.* 2017). However, none of these models has been used for predicting changes in mechanical properties of the erythrocyte skeleton that occur during invagination of malaria merozoites. Lattice models have been used to capture local mechanical behaviour of continuum systems such as metals, composites, ceramics and polymers (Ostoja-Starzewski 2002, Ostoja-Starzewski *et al.* 1996). These models have been applied for predicting crack propagation in continuum systems hence suitable for modelling spectrin network damage in the erythrocyte membrane (Chen and Boyle 2014, Li *et al.* 2007, Saito *et al.* 2015). Several structural models of spectrin have been developed to predict how spectrin stretches from undeformed to deformed states (Law *et al.* 2003). Multi-scale models based on dissipative particle dynamics have been used to simulate the deformations of infected erythrocytes during the intra-erythrocytic development stages (Fedosov *et al.* 2011). Despite numerous previous models, none has been developed to model the malaria merozoite induced erythrocyte membrane damage.

### 1.3.2 Isotropic hyperelastic constitutive models for the erythrocyte membrane

Biological cells are primarily made up of naturally occurring biopolymers, e.g., proteins, DNA, RNA, peptides, and enzymes. An in-depth understanding of the mechanical behaviour of biopolymers is, thus, essential to understanding the mechanical behaviours of biological cells and their load-bearing structures. Experimental and in silico characterisation of biopolymers undergoing damage has received limited attention. In silico experiments are recently attracting more attention because they could be easily conducted. However, an adequate mathematical representation of the material behaviour and test condition is required to achieve accurate predictions. Various hyperelastic models have been applied to predict the deformation of biological cells. However, most of these models are not developed to predict biological damage. For example, The Neo-Hookean model developed based on cross-linked polymer chains is ideal for predicting finite deformations in intact biological membranes and tissue. Furthermore, the Neo-Hookean material model is only accurate for a strain of less than 20% (Austrell and Kari 2005). Additionally, the strain energy density function of the model only depends on a single invariant $I_1$ of the right Cauchy-Green deformation tensor, which limits the accuracy of the model, particularly in applications where material deformation also depends on the second invariant $I_2$. The Mooney Rivlin model is the extension of the Neo-Hookean (NH) model and was first proposed by Melvin Mooney in 1940 and was written in terms of invariants by Ronald Rivlin in 1948. The strain energy density function of the Mooney Rivlin model forms a linear combination of two invariants of the left Cauchy-Green deformation tensor. The advantage of this model over the Neo-Hookean model

is that the model is valid for a higher maximum biaxial strain of 138%. In many applications, introducing the second material parameter $C_{01}$ and the second invariant $I_2$ improves the accuracy of the stress predictions. However, the addition of the second invariant of the Cauchy-Green tensor can lead to unstable material behaviour. The Mooney Rivlin model was previously applied to computationally predict erythrocyte deformation in a microfluid device and optical tweezer (Chee *et al.* 2008). However, erythrocyte membrane damage was not considered. The polynomial model is a higher-order function of the first and second invariants comprised of the Neo-Hookean (NH), Mooney Rivlin, and Yeoh models. The higher older terms do not necessarily contribute to the accuracy of the prediction. The three models in the polynomial model equation make the determination of material parameters for multi-axial loading applications demanding(Bergström 2015). The eight-chain model developed by Arruda and Boyce (Arruda and Boyce 1993) was introduced to predict the deformation of molecular chains in the microstructure of intact elastomers in which molecular chains are aligned along the diagonals of a unit cell, and material damage was not considered. The Ogden model is often expressed in terms of the principal stretches in all three principal directions. Unlike the Mooney Rivlin model, the Ogden model can be difficult to calibrate due to the relatively many material parameters (Kim *et al.* 2012). The Gent model extends the Neo-Hookean (NH) model to predict elastomeric materials at large deformations. The model only contains three material parameters, μ, J and k, representing the material shear modulus, the Jacobian of the left Cauchy tensor, and the material's compressibility. The Horgan and Saccomandi (HS) model is an extension of the Gent model (Bergström 2015). Like the Gent model, the HS model contains only three parameters, but the main difference between the Gent and the HS model is that the HS model depends on both the first invariant $I_1$ and the second invariant $I_2$. Just like the Gent model, the Knowles model is an extension of the NH model. The main difference is that the Knowles model contains a hardening parameter. The model was developed to predict the crack tip response of incompressible elastic solids such as poly-L-lactic acid solid materials.(Bergstrom 2015). The aforementioned hyperelastic models have been previously assessed based on their predictive accuracies. However, it is essential to note that the predictive accuracies of the models also depend on the boundary conditions. As such, the hyperelastic model's stability, accuracy, and deformation mode need to be considered when selecting a hyperelastic model for modelling applications. Table 1 provides various material models with their predictive accuracy and the number of parameters required for calibration. In addition to the model's predictive accuracy, the number of parameters in the model needs to be considered when selecting the material model. Material models with fewer parameters are easier to calibrate.

Table 1: Hyperelastic models with their predictive accuracies and the number of material parameters (Bergstrom 2015).

| Hyperelastic model | $R^2$ prediction | Number of parameters |
|---|---|---|
| Neo-Hookean | 0.794 | 2 |
| Mooney-Rivlin | 0.843 | 3 |
| Yeoh | 0.98 | 4 |
| Eight chain | 0.973 | 3 |
| Ogden (2 term) | 0.977 | 5 |
| Ogden (3 term) | 0.998 | 7 |
| Gent | 0.972 | 3 |
| Horgan-Saccomandi | 0.901 | 3 |
| Knowles | 0.85 | 4 |
| Response function | 0.96 | 0 |
| Extended tube | 0.997 | 5 |

## 1.4 Computational damage mechanics of erythrocyte membranes

### 1.4.1 Continuum damage mechanics of biological membranes

Continuum damage mechanics (CDM) is a branch of continuum mechanics used to describe the damage and fracture processes involving the initiation of microcavities or microcracks, propagation of microcracks, development of macrocracks and fracture in a material (Murakami 2012). The concept was first proposed by (Kachanov 1999) for modelling creep damage due to micro-voids. In brief, continuum damage mechanics involves the following aspects:

- Representation of the damage state with a damage variable function
- Formulation of an equation governing the development of the damage variable (i.e., evolution equation)
- Formulation of an equation describing the mechanical behaviour of the damaged material (i.e., constitutive equation)
- Solving the initial and boundary value problem

Since its inception, CDM has been used to study damage mechanics in a wide range of materials, including soft biological tissues (Calvo *et al.* 2007a). CDM mainly involves averaging the mechanical properties of a material with micro defects, e.g., microvoids. Typically, this is often achieved by

introducing an internal state damage variable function into the Helmholtz free energy function representing the strain energy of an intact material. Careful selection of the Helmholtz free energy function must ensure high accuracy of model predictions and ease of calibration if required.

#### 1.4.1.1 Scales of chemical damage phenomena in the erythrocyte membrane

The constituents of the erythrocyte membrane are mainly made up of biopolymers. The interactions of the constituent atoms or molecules in biopolymers determine the mechanical properties of the erythrocyte membrane. At the molecular or atomic scale, the primary damage mechanism in the erythrocyte membrane during the invasion process is protein phosphorylation which may lead to the dissociation of the interatomic or intermolecular bonds. At the spectrin network scale, damage may be characterised by the number of defects in the network. At the erythrocyte membrane scale, the material damage can typically be described by microscopic discontinuities in the spectrin network. At this scale, the mechanical property of the material with various microscopic discontinuities is averaged over a small region and expressed as a continuous function. The averaging of the mechanical properties of a material with defects into a continuum forms the basis of continuum damage mechanics.

#### 1.4.1.2 Physical mechanisms of mechanical damage in erythrocyte membrane

Human cells, including erythrocytes, are often subjected to more than one loading mode, i.e., shear, compression. When excessive loading occurs, cells can undergo mechanical damage. Extreme stretching of the load-bearing cellular structures can lead to excessing unfolding of the protein chains, which often results in the rupture of the protein. Unfolding the protein chains can also lead to conformational changes in the protein chains, exposing several protein binding domains useful for activation of the biochemical reactions, which can either further compromise the mechanical integrity of the cellular structure or reinforce the mechanical integrity of the protein chains. To date, the knowledge of damage and repair mechanisms in biological cells remains limited. However, the continuum damage mechanics approach can set a new foundation for studying damage in biological cells. Damage mechanics of biological cell membranes have rarely been studied due to the microscopic size and the difficulty of measuring the mechanical damage effects that are dynamically regulated through signalling.

### 1.4.2 Continuum damage models for soft biological materials

Several models based on the continuum damage mechanics (CDM) approach have been developed in recent years; for instance, Rodriguez *et al.* (2008) developed and implemented a three-dimensional finite-strain constitutive model for soft fibrous tissue undergoing damage. The main limitation of the

model fails to capture viscoelastic effects such as creep and relaxation. Calvo *et al.* (2007b) developed the uncoupled directional damage model for fibred soft biological tissue where the strain energy density function is decomposed into two parts, representing the fibres and the matrix as follows:

$$\psi( C_t, M_{st}, N_{st}, D_{mv}, D_{fv} ) = \psi_{vol}( J ) + ( 1 - D_{mv} )\psi_{0m}( C_t ) + ( 1 - D_{fv} )\psi_{0f}(C_t, M_{st}, N_{st} ) \quad (2)$$

where $M_{st}$ and $N_{st}$ are structural tensors that describe the fibre orientation, $\psi_{vol}(J)$ is a volumetric strain energy density function $\psi_{0m}$ is the isochoric strain energy density function of the undamaged matrix material. $\psi_{0f}$ represents the strain energy density function of intact fibres. $(1 - D_{mv})$ and $(1 - D_{fv})$ are reduction factors for the matrix and the fibres, respectively. $C_t$ is the right Cauchy deformation tensor

In the healthy erythrocyte, elastic properties are mainly determined by the spectrin network, and hence the elasticity of the embedding matrix could be ignored. Without the embedding matrix and structural tensors, this approach could be relevant for modelling the malaria merozoite induced erythrocyte membrane damage. The structural tensors describing the fibre orientations could be ignored when modelling erythrocyte membrane damage because the erythrocyte membrane skeleton comprises a 2D spectrin lattice forming a uniform pattern of elastic spectrin tetramers, thus creating an isotropic structure.

Pseudo-elasticity is generally used to model Mullin's effect to describe stress softening of filled rubber elastomers under quasi-static cyclic loading (Ogden and Roxburgh 1999). This theory also falls under the broad field of CDM, where the damage variable only affects the deviatoric strain energy component. Hence, the standard Mullins effect model may be limited to material damage involving volumetric degradation. With few modifications of Mullin's effect, the model can be effectively applied for non-cyclic loading. Additionally, with minor adjustments to the damage variable function, Mullin's model can be used for modelling biodegradation. The energy stored in a material with the pseudo elastic response is given as follows:

$$\psi (J, B, \eta) = \psi_{vol} (J) + \eta\, \psi_{dev}(B) - \varphi_d (\eta) \quad (3)$$

where $\psi_{dev}$ is undamaged material's initial deviatoric strain energy density, $\psi_{vol}$ is the volumetric part of the strain energy density function. $\eta = 1$ represents the damage variable for the primary loading phase where $\varphi_d (\eta = 1) = 0$, $\varphi$ is the damage function. For subsequent unloading and reloading when $\eta < 1$, the damage evolves as follows:

$$\frac{\partial \psi}{\partial \eta} = \psi_{dev}( B ) + \varphi'_d( \eta ) = 0 \quad (4)$$

where $\varphi'( \eta ) = \frac{d\varphi(\eta)}{d\eta}$

In Abaqus Explicit, the damage variable for modelling the Mullins effect is defined as follows:

$$\eta = 1 - \frac{1}{r_p} \operatorname{erf}\left( \frac{\psi_{max} - \psi_{dev}}{m_p - \beta_p \psi_{max}} \right) \quad (5)$$

where $\psi_{max}$ is the maximum of $\psi_{dev}$, $r_p$, $m_p$, and $\beta_p$ are material parameters; erf ( x ) is an error function defined as follows:

$$\operatorname{erf}(x) = \frac{2}{\sqrt{\pi}} \int_0^x \exp\left(-w^2\right) dw \quad (6)$$

#### 1.4.2.1 Introduction to damage variable functions

The damage variable functions proposed for modelling damage in soft fibrous tissue such as ligaments share similar aspects as follows:

- The damage variable function is a monotonically increasing function
- The damage evolution functions are dependent on the thermodynamic force, i.e., the strain energy
- The equation representing damage is relatively simple and involves few parameters

These aspects can also be considered when modelling chemical damage. Most biochemical processes that lead to mechanical degradation of biological membranes reduce the elastic modulus of the membrane. EBA-175 secreted by the malaria merozoites induces protein phosphorylation of the erythrocyte membrane skeleton leading to the reduction of the elastic modulus of the erythrocyte membrane. Nano-indentation studies of a healthy erythrocyte indicated that 50 nM of EBA-175 induces approximately 96% reduction in the elastic modulus of the erythrocyte membrane, see Figure 4 and Figure 5 (Sisquella *et al.* 2017). Hence to accurately model the malaria merozoite induced damage, the damage variable function must reduce the elastic modulus of the erythrocyte membrane.

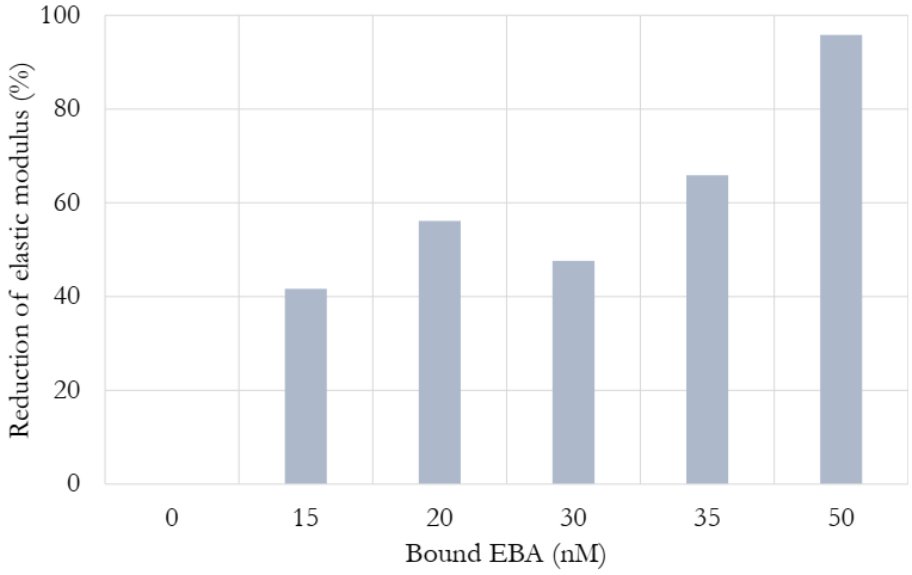


Figure 4: EBA-175 concentration vs AFM Young's modulus (Sisquella *et al.* 2017).

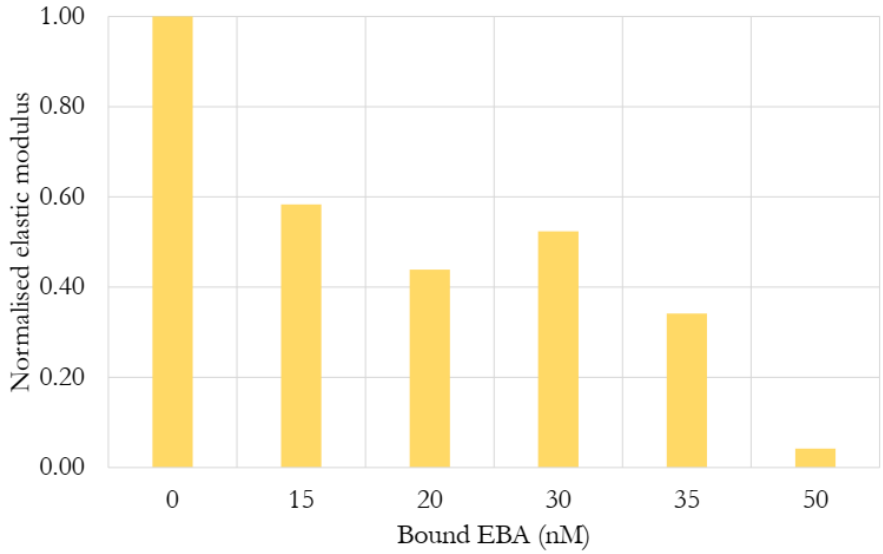


Figure 5: Normalised elastic modulus representing the mechanical state of the erythrocyte membrane relative to the EBA-175 RII dose (Sisquella *et al.* 2017).

To date, the concentration of EBA-175 secreted by the malaria merozoite is unknown. Additionally, it is not known whether malaria merozoite induced damage only occurs at the beginning of the invasion or occurs progressively throughout the entire invasion process. With the developed computational damage model, various damage scenarios can be assessed to determine their impact on the invasiveness of the malaria merozoite.

#### *1.4.2.2* Exponential damage variable functions

The exponential damage variable function denoted by $D_k$, in Eqn. (7) was proposed to describe the mechanical damage in fibrous biological material (Balzani *et al.* 2006). With few adjustments, this damage variable function can be applied to model phosphorylation damage in the erythrocyte membrane.

$$D_k\left(\psi_0\right) = \gamma_1 \left[1 - \exp\left(\frac{-\beta_3\, \psi_0}{\gamma_2}\right)\right] \tag{7}$$

where $\beta_3\psi_0$ is a modified internal variable representing the scaled strain energy density of the intact material per reference volume. When $\gamma_2 = \max(\beta_3\, \psi_0)$, $\gamma_1 = 1$, $\beta_3 \geq 1$, the damage variable increases monotonically.

#### *1.4.2.3* Polynomial damage variable functions

Peña *et al.* (2008) developed the polynomial damage variable function defined as follows:

$$D_k(\Xi_k) = \begin{cases} 0 & \text{if } \Xi_k < \Xi_{min} \\ \Lambda^2\,[1 - \eta_e\,[\Lambda^2 - 1]] & \text{if } \Xi_{min} \leq \Xi_k \leq \Xi_{max} \\ 1 & \Xi_k > \Xi_{max} \end{cases} \tag{8}$$

where $\Lambda = (\Xi_k - \Xi_{min})/(\Xi_{max} - \Xi_{min})$ is a dimensionless parameter, $\eta_e = [-1, 1]$ and $\Xi_k$ is the strain energy of the intact model. $\Xi_{min}$, $\Xi_{max}$ are the intact material model's minimum and maximum strain energy, respectively.

#### *1.4.2.4* Sigmoid damage variable functions

Another damage variable function for soft biological tissue was proposed by Rodriguez *et al.* (2008) and is written as follows:

$$D_k\left(\Xi_k\right) = \frac{1}{2}\left(1 + \frac{\xi_k\, \Xi_k\, \exp\left(2\xi_k\left[\left(\frac{2\Xi_k}{\rho_k}\right) - 1\right]\right) - 1}{\xi_k \Xi_k\, \exp\left(2\xi_k\left[\left(\frac{2\Xi_k}{\rho_k}\right) - 1\right]\right) + 1}\right) \tag{9}$$

where $\rho_k \geq 0$ and $\xi_k$ are experimentally determined constants. The drawback of this damage variable function is that the damage initiation cannot be controlled since the parameters $\Xi_{min}$ and $\Xi_{max}$ representing the material's minimum and maximum strain energy are not considered. However, Peña *et al.* (2009) improved the function in Eqn. (9)(9 by incorporating the dimensionless variable $\Lambda_k = (\Xi_k - \Xi_{min})/(\Xi_{max} - \Xi_{min})$ defined as follows:

$$D_k(\Xi_k)=\begin{cases}0 & \text{if } \Xi_k<\Xi_{min}\\ \frac{1}{2}\left(1+\frac{2\xi_k\Lambda_k\exp\left(2\xi_k[2\Lambda_k-1]\right)-1}{2\xi_k\Lambda_k\exp\left(2\xi_k[2\Lambda_k-1]\right)+1}\right) & \text{if } \Xi_{min}\leq\Xi_k\leq\Xi_{max}\\ 1 & \Xi_k>\Xi_{max}\end{cases} \quad (10)$$

Note that when $\Lambda_k = 1$ and $\xi_k = 1$, the total damage is less than 1, indicates that for relatively smaller values of $\xi_k$, not only does $\xi_k$ affect the shape of the damage variable function but also affects the total amount of damage.

## 1.5 Problem identification

Invasion of erythrocytes by malaria merozoites marks the pathogenesis of malaria. When untreated, a single invasion can lead to a rapid expansion of malaria parasites in the human host, leading to excessive sequestration of infected erythrocytes in the blood, which often results in severe malaria and death (Leitgeb *et al.* 2017). Erythrocyte invasion has been extensively studied as a target for antimalarial vaccines. However, despite the enormous research efforts in this area of research, clinically approved invasion blocking compounds remain unavailable for treatment. This lack is mainly due to the limited mechanistic understanding of the invasion mechanism.

Advances in proteomics and improvements in data acquisition technologies over the past decade have led to new experimental tools for studying the invasion process. Data obtained from such studies have addressed some of the long-standing research questions related to the molecular interaction between the plasmodium falciparum merozoite antigens and the erythrocyte surface receptors. Global and subcellular proteomics have revealed essential features of the parasite's regulatory mechanisms (Zuccala *et al.* 2016). Proteomic studies have revealed the activation of phosphorylation cascades by the malaria merozoite's erythrocyte binding antigen 175 (EBA-175) (Sisquella *et al.* 2017). Whole-genome sequencing and protein biochemistry has provided evidence that erythrocyte interactions with reticulocyte binding like (RBL) and erythrocyte binding like (EBL) invasion ligands on the merozoite surface regulate the erythrocyte's preference for Plasmodium parasites (Paul *et al.* 2015).

Although much progress has been achieved in understanding certain aspects related to the role of molecular factors in the invasion mechanism, most of these studies do not address the role of biomechanical factors associated with the invasion process. Experimental data on the mechanical properties of the human erythrocytes are widely available, including the parameters that determine the erythrocytes deformability, such as cell shape, cytoplasmic viscosity, and membrane deformability and stability (Mohandas and Chasis 1993b, Mohandas and Evans 1994). However, it remains to be clarified how these factors impact the invasiveness of the malaria merozoite.

## 1.6 Aims and objectives

The aims of this research were:

Aim 1: To analytically and computationally investigate the mechanical factors that determine the invasiveness of a malaria merozoite during its entry into the erythrocyte.

Aim 2: To evaluate the impact of local membrane damage on an erythrocyte's regional and global mechanical properties towards cell mechanics profiling of invasion blocking anti-malarial compounds that target erythrocyte membrane damage mechanism.

The following objectives were formulated to achieve the aims:

Objective 1: To develop an analytical model for establishing the major factors facilitating erythrocyte membrane wrapping of a malaria merozoite.

Objective 2: To develop an erythrocyte membrane damage model for simulating the malaria merozoite induced damage during the invasion process.

Objective 3: To develop a finite element model for evaluating the malaria merozoite's invasiveness during its entry into the erythrocyte.

Objective 4: To computationally investigate the sensitivity of cell mechanics tests, namely whole-cell compression and nanoindentation, to local erythrocyte membrane damage induced by malaria merozoites.

### 1.6.1 Impact of erythrocyte morphology on the invasiveness of the malaria merozoite

The erythrocyte shape is often defined in terms of surface area to volume ratio (S/V), a measure of sphericity that determines the deformability of the erythrocyte. A healthy human erythrocyte has a biconcave discoid shape with ~8 μm in diameter and ~2 μm in thickness (Tomaiuolo 2014). When subjected to adverse loading conditions, a healthy erythrocyte can undergo finite deformations of up to 230% of its original dimension. This large deformation is possible because of the large surface area of the discoid shape. Generally, a healthy erythrocyte has a volume of 94.5 $\mu m^3$ and a surface area of 135.2 $\mu m^2$ (Li *et al.* 2014a) and a surface area to volume ratio S/V of 1.43/m. If the same erythrocyte is transformed into a sphere of identical volume, it would have a surface area of only 98 $\mu m^2$ with an S/V of 1/m. Hence, the discoid shape provides approximately 40 $\mu m^2$, or 43%, of excess surface area, approximately five times the merozoite surface area of 8.01 $\mu m^2$ (Dasgupta *et al.* 2014).

The impact of the S/V ratio on the erythrocyte's deformability motivated the interest to investigate the role of the S/V ratio on the malaria merozoite invasiveness. Currently, the impact of S/V, or simply the shape of an erythrocyte on the invasiveness of the malaria merozoite, is unknown. Furthermore, erythrocytes with hereditary disorders such as spherocytosis are less vulnerable to the invasion by the malaria merozoite. Genetic alteration of membrane proteins has been documented as the leading factor mediating the invasion resistance (Eber and Lux 2004). However, little is known on the impact of shape or S/V ratio of the invasiveness of malaria merozoite. Reasons may include the difficulty of conducting such studies in an in vitro experiment. For example, in an in vitro study, it may be difficult to replicate the microenvironments of the human host. Additionally, it may be challenging to control multiple impact factors independently, for instance, allowing S/V alterations while keeping other determinants of erythrocyte deformability unchanged. One common practice for altering the shape of a healthy erythrocyte in a physical experiment is by incubating the erythrocyte in a hypotonic solution (Linderkamp and Meiselman 1982) to allow water ($h_2o$) to diffuse into the cell and hence changing the erythrocyte shape. The drawback of this approach is that diffusion of $h_2o$ into the cell can interfere with other impact factors such as the cytoplasmic viscosity. In individuals with spherocytosis, erythrocytes take a spherical form due to alterations of erythrocyte membrane proteins. These alterations may have some effect on the mechanical properties. To efficiently investigate the impact of the S/V ratio independently of other factors, we have developed an in silico platform for conducting in silico experiments.

In total, the process of spherocytosis involves alteration of the erythrocyte membrane leading to shape changes. Understanding the effect of shape stiffness on the invasiveness of the malaria merozoite in spherocytes could help understand the malaria resistance mechanism in spherocytes. The computational model would allow the assessment of the impact of erythrocyte morphology on the invasiveness of the malaria merozoite in a less cumbersome manner, see Figure 6 a. Additionally, an in silico approach provides an easy way of studying the invasion energetics in the convex and the concave region of the erythrocyte (see Figure 6 b and c), which would be challenging or impossible to determine in an in vitro experiment.

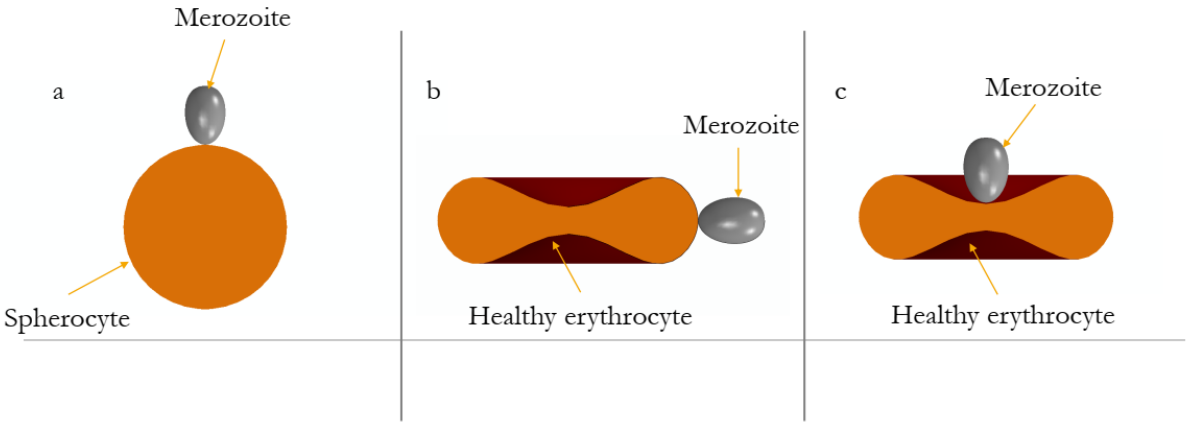


Figure 6: Spherocyte invasion by a malaria merozoite (a), convex region invasion of a discoid erythrocyte by a malaria merozoite (b), concave region invasion of a discoid erythrocyte by a malaria merozoite.

### 1.6.2 Impact of erythrocyte membrane damage on the invasiveness of the malaria merozoite

The impact of the malaria merozoite induced erythrocyte membrane damage on the invasiveness of the merozoites has a limited scope. This is due to the lack of constitutive models describing the remodelling of the erythrocyte membrane during entry of the malaria merozoite**.** Using a continuum damage mechanics framework, the remodelling effect due to the phosphorylation of the erythrocyte membrane proteins can be incorporated into the Helmholtz free energy function.

Under normal physiological conditions, the erythrocyte membrane skeleton proteins form a stable network consisting primarily of spectrin tetramers. Structural defects in the membrane skeleton arising from genetic mutations involving αβ spectrin, ankyrin, band 3, or protein 4.1R lead to the loss of cohesion between the lipid bilayer and the spectrin network resulting in a mechanically unstable membrane (Discher *et al.* 1995). Alterations of the membrane skeleton during the intraerythrocytic developmental stage of the malaria parasite life cycle result in a less deformable erythrocyte. Apart from genetically induced structural alteration, the erythrocyte membrane mechanical properties can also be actively altered or regulated by activating phosphorylation and dephosphorylation reactions of membrane skeleton proteins. Protein phosphorylation is a reversible reaction that involves adding a phosphate group to an amino acid residue. This process alters the structural conformation of proteins, causing them to become activated, deactivated, or modified in terms of their function and mechanical properties. Dephosphorylation refers to removing a phosphate group from an organic compound by hydrolysis. A notable occurrence of dephosphorylation is the conversion of adenosine triphosphate (ATP) to adenosine diphosphate (ADP) and inorganic phosphate. In simple terms, phosphorylation can be described as a forward reaction in which ADP is converted into ATP while dephosphorylation is the backward reaction in which ATP is converted into ADP as follows:

$$[ADP]_t \rightleftharpoons [ATP]_t \tag{11}$$

The Michaelis–Menten kinetics can be written in the form of a differential equation:

$$\frac{d[ADP]}{dt} = -k_f[ADP]_t + k_b([ADP]_0 - [ADP]_t) \tag{12}$$

where $k_f$ is a parameter for the forward reaction, i.e. phosphorylation, and $k_b$ is for the backward reaction. [ADP]t and [ATP]t denote ADP and ATP concentration at time t. $[ADP]_0$ denotes the concentration of ADP at t=0. The solution of the differential equation in Eqn. (12, given in Eqn. (13) defines an exponential decay function similar to strain-based exponential reduction functions generally used in the field of continuum damage mechanics for describing material deterioration.

$$[ADP]_t = [ADP]_0 \left( \frac{k_b + k_f \exp(-t(k_f + k_b)}{k_f + k_b} \right) \tag{13}$$

Under the normal physiological function of the cell, the bidirectional process in Eqn. (11) can be considered to be bi-stable. However, the malaria merozoite disrupts the bi-stable reaction during the invasion so that phosphorylation reaction dominates. Like in so many other biological cells, phosphorylation is a primary mechanism by which mechanical properties of the erythrocyte cell membrane are regulated (Zuccala and Baum 2011). Phosphorylation of band 4.1 weakens the connections between band 4.1, spectrin and actin, leading to membrane destabilisation (Betz *et al.* 2009). In addition, phosphorylation of β spectrin also results in decreased membrane stability (Manno *et al.* 1995), while tyrosine phosphorylation of SLC4A1 weakens its attachment to the underlying skeletal network and increases its membrane mobility by altering ankyrin binding (Ferru *et al.* 2011). During the erythrocyte invasion, malaria parasites manipulate these kinetic processes to maximise their invasion efficiency. EBA-175 activated phosphorylation has been related to erythrocyte membrane elasticity. EBA-175 concentrations of 0-50 nM correlated to a reduction in the elastic modulus of 1-96 % (Sisquella *et al.* 2017). However, this data alone is not sufficient to fully understand merozoite induced damage because the exact concentration of EBA-175 secreted by the malaria merozoite is unknown. Additionally, it is not known whether EBA-175 binding to the GPA receptors on the erythrocyte membrane causes an instantaneous reduction in the erythrocyte membrane elastic modulus only at the beginning of the active invasion or whether it occurs progressively throughout the invasion process. An in silico model can enable investigations of such scenarios by using parametric studies to deepen the understanding of the invasion event.

### 1.6.3 Assessing erythrocyte damage using whole-cell compression and nano-indentation

Although numerous investigations have been conducted on the variation of the mechanical properties of an infected erythrocyte during the intraerythrocytic developmental stage of the parasite, to date, the effect of malaria merozoite induced erythrocyte membrane damage has received limited attention.

The current study seeks to determine the relative sensitivity of indentation force with respect to the local erythrocyte membrane damage by evaluating numerical data obtained from compression and nanoindentation simulations, illustrated in Figure 7 (a and b**)**. The compression and nanoindentation forces will be evaluated based on the amount of erythrocyte membrane damage to determine whether erythrocyte membrane damage affects the compression and nanoindentation forces, locally and globally, respectively. Furthermore, the high sensitivity of the indentation or compression forces for a given amount of damage would indicate that compression or nanoindentation in vitro experiments have a high potential for investigating erythrocyte membrane damage. Hence the data from compression and nanoindentation simulations would guide in vitro experiments for investigating erythrocyte membrane damage. These simulations can also guide experimental investigations involving the efficacy assessment of invasion blocking compounds that target the erythrocyte membrane damage mechanisms. Signalling induced by the malaria merozoite is related to reducing the stiffness of the erythrocyte membrane (Sisquella *et al.* 2017). Any anti-malarial compound that blocks signalling would also block the local changes in the mechanical properties of the erythrocyte membrane. Hence the efficacy of such a compound may be determined by a mechanical test that is highly sensitive to local alterations of the elastic modulus of the erythrocyte membrane.

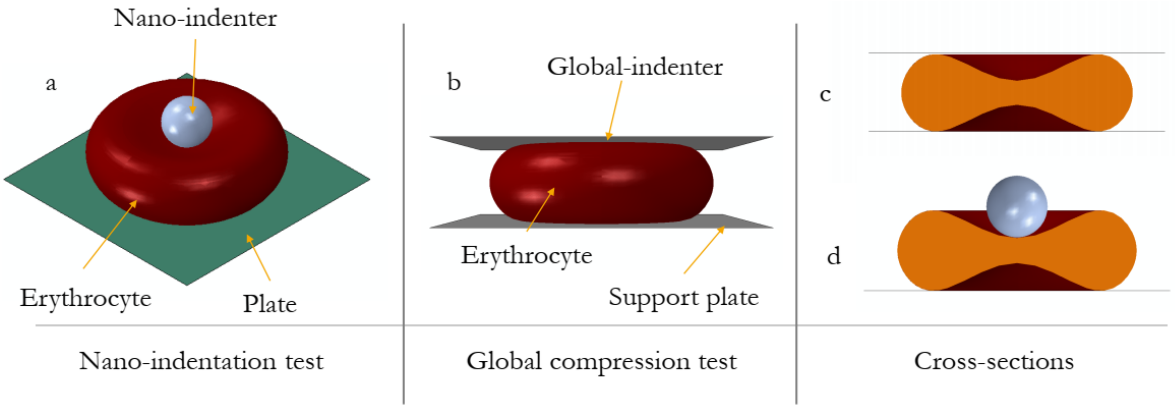


Figure 7: Nano-indentation simulation of a locally damaged erythrocyte in Abaqus Explicit (a), compression simulation of the locally damaged erythrocyte (b), c and d are cross-sections of b and a respectively.

## 1.7 Chapter overview

The following chapters of this thesis comprise the following:

Chapter 2 introduces a new analytical model for describing the entry of the malaria merozoite into a human erythrocyte. Insights into the mechanics of erythrocyte membrane wrapping have been presented using the membrane theory of shells. With the analytical model, we can predict the force applied by the malaria merozoite vs displacement required to achieve a successful invasion.

Chapter 3 presents the constitutive model for the malaria merozoite induced remodelling of the erythrocyte membrane. The development of the erythrocyte membrane damage model has been discussed in detail. The damage model is based on continuum damage mechanics in which the damage variable describing the chemically induced erythrocyte membrane deterioration is incorporated. The implementation of the damage model in Abaqus Explicit is achieved by using VUMAT subroutine. With this model, the impact of erythrocyte membrane damage on invasion mechanics has been analysed and assessed in Chapter 4.

Chapter 4 presents a finite element model developed and applied for investigating the impact of erythrocyte biophysical and biomechanical factors such as shape or morphology on the invasiveness of the malaria merozoite. The theoretical framework for developing the computational model has been presented in detail. A two-component approach is used for the erythrocyte 3D model. The erythrocyte membrane and cytoplasm domain are described by a Lagrangian formulation. Smoothed particle hydrodynamics (SPH) has been applied to the viscous cytoplasmic domain to allow extreme deformations associated with the entry of the malaria merozoite. Appropriate mechanical contact definitions between interacting structures and surfaces involved in the invasion process have been

described. 3D computational mechanics models for nano-indentation and global compression were developed. Information from these simulations has been used to assess the feasibility of physical experiments to identify local malaria merozoite induced damage in erythrocytes for applications in drug screening.

Chapter 5 provides overall conclusions and recommendations for future work.

# 2 An analytical model of the mechanics of erythrocyte membrane wrapping during the active invasion of a plasmodium falciparum merozoite

## 2.1 Introduction

Invasion of erythrocytes by malaria merozoites marks the pathogenesis of malaria. The invasion process involves mechanical and biochemical interactions whereby the malaria merozoite exerts an actomyosin based force to push itself into the erythrocyte while inducing biochemical damage of the erythrocyte membrane, thus optimising its invasion efficiency.

For a long time, the role of molecular factors in the invasion of a human erythrocyte by a malaria merozoite has been extensively investigated (Cowman and Crabb 2006). However, the major challenge has been identifying antimalarial compounds that target the binding of the malaria merozoite during the entry process. This is because erythrocyte membrane proteins are redundant, and unless all surface proteins are disrupted, it is impossible to block erythrocyte invasion. New approaches in proteomics (Guiguemde *et al.* 2010), chemoinformatics (Plouffe *et al.* 2008), and genetics (Rottmann *et al.* 2010) have shown promise in addressing this challenge. Despite this progress, to date, no clinically approved vaccine that blocks the invasion process is available for clinical use; this is due to the limited knowledge of the invasion process. Hence the need for new approaches for advancing the knowledge domain of the erythrocyte invasion.

The simulation studies of the mechanics of the invasion erythrocytes have not yet been extensively explored, and this has limited insights for guiding experimental investigations related to the invasion of erythrocytes. Few mathematical models have been developed to analyse and predict erythrocyte invasion mechanics. A recent analytical model developed by Abdalrahman and Franz (2017b) employs contact mechanics to describe the deformation of the erythrocyte membrane due to adhesion energy for indentation up to 10% of the merozoite length. The model by Dasgupta *et al.* (2014) described erythrocyte membrane wrapping, a mechanism associated with the internalisation of the malaria merozoite where the contribution of erythrocyte membrane wrapping to the invasion energetics was predicted.

The wrapping process begins with a low-affinity attachment of the malaria merozoite on the surface of the erythrocyte membrane followed by a cascade of key invents such as the active entry in which the malaria merozoite exerts an actomyosin force, induce erythrocyte membrane skeleton remodelling,

establish the tight junction and the sealing of the erythrocyte membrane. However, to date, a detailed model for describing the deformation of the erythrocyte membrane due to the malaria merozoite's applied forces remains unavailable.

Findings from the previous in vitro study where the erythrocyte membrane was quasi-statically loaded indicate that the yield strain of the membrane ranges between 2% and 4% areal strain, beyond which cell lysis occurs (Li *et al.* 2014b). Interestingly, cell lysis does not occur during the invasion process. The absence of lysis may suggest that (i) erythrocyte membrane wrapping is associated with small areal strain (< 4%) or (ii) locally induced erythrocyte membrane strain larger than 4% does not induce cell lysis. Hence, the mechanics related to small and finite erythrocyte membrane areal strain are investigated in this study.

The lack of mechanistic understanding of the invasion mechanism has limited the scope of anti-malaria drug targets. Mechanical markers, generally referred to as mechanical phenotypes or mechanotypes, are emerging label-free markers with the potential of being used as drug targets (Qi *et al.* 2015). In silico determination of the relevant mechanism that determines the invasiveness of the malaria merozoite can provide new insights to guide the development of invasion blocking anti-malarial compounds. The development of such tools requires a detailed mathematical description of the biomechanical interactions occurring during the invasion process. Hence this study aimed to analytically investigate the mechanics of the erythrocyte membrane during entry of the malaria merozoite. With the developed analytical model, the malaria merozoite actomyosin forces have been predicted in terms of both small (< 4%) and finite (> 4%) areal strains.

## 2.2 Model development

The erythrocyte membrane wrapping mechanism was modelled using membrane theory of shells where the differential equation describing the equilibrium configuration of a circular erythrocyte membrane of radius $r_m$ and a rigid egg-shaped merozoite is solved numerically throughout the entire invasion process (Villaggio 1997). The equations describing the morphology of the malaria parasite are first presented. Thereafter, the deformation of the erythrocyte membrane is described in terms of the shape parameters of the malaria merozoite. The equations describing the deformation and the constitutive law of the erythrocyte are used to formulate equilibrium and governing equations. The governing equations are then numerically solved using the Runge-Kutta fourth-order method to obtain stretches and stresses in the erythrocyte membrane. The solution of the governing equation simulates erythrocyte membrane wrapping in terms of a classical areal strain of the erythrocyte membrane of less than 4%, a generally accepted value for quasi-static deformation of the erythrocyte membrane.

However, the model has also been applied to explore the mechanics of erythrocyte membrane wrapping for larger areal strain values of less than 51%.

To describe the mechanics of membrane wrapping associated with the entry of a malaria merozoite into a healthy erythrocyte, the following are the basic simplifying assumptions used for developing this model:

a) The erythrocyte membrane is homogeneous and mechanically isotropic
b) The erythrocyte membrane has a small thickness of 0.01 μm
c) The region of the erythrocyte membrane involved in the wrapping is initially flat
d) The bending modulus of the erythrocyte membrane is small, and only the mid-plane strain due to other loading modes are considered
e) The malaria merozoite is assumed rigid, i.e., non-deformable

### 2.2.1 Physical and mechanical properties of a healthy erythrocyte

A mature human erythrocyte is a biconcave discoid shaped cell with a diameter of 7.8 μm and a thickness that varies from 0.8 to 2.6 μm. It is mainly composed of the cytoplasm and surrounded by a continuous membrane. In a healthy erythrocyte, the liquid cytoplasm comprises a concentrated haemoglobin solution with a viscosity of approximately 6 to 10 mPa s (Dimitrakopoulos 2012). At normal physiological conditions, the erythrocyte haemoglobin viscosity has a negligible contribution to erythrocyte deformability, and the deformability of the cell is mainly determined by the erythrocyte membrane. However, at high viscosity of 650 cP (Mohandas and Chasis 1993a), the erythrocyte cytoplasm becomes a primary determinant of cellular deformability (Mohandas *et al.* 1979).

The erythrocyte membrane is a layered structure comprising the lipid bilayer and the membrane skeleton. The lipid bilayer is often considered as a two-dimensional incompressible structure without shear resistance, whereas the underlying membrane skeleton is composed of a spectrin network that enables the erythrocyte membrane to resist shear loads (Dimitrakopoulos 2012). The biconcave discoid shape of a healthy erythrocyte allows it to undergo large deformation of up to 230% of its original dimension while maintaining minimal areal strain. An erythrocyte has a volume of 94.5 $\mu m^3$ and a surface area of 135.2 $\mu m^2$ (Li *et al.* 2014a). Compared to the surface area of 98 $\mu m^2$ of a sphere with an identical volume, the discoid shape of an erythrocyte increases its surface area by approximately 37 $\mu m^2$, which is approximately 4.6 times the surface area of a merozoite of 8.0 $\mu m^2$ (Dasgupta *et al.* 2014). This excess surface area suggests that the erythrocyte may wrap the malaria merozoite entirely while maintaining a small areal strain in the membrane.

### 2.2.2 The geometry of a malaria merozoite

The idealised geometry of the merozoite is defined by:

$$(x^2 + y^2 + z^2)^2 = R_a\, x^3 + (R_a - R_b)\, x\, (y^2 + z^2) \qquad (14)$$

where $R_a$ = 1 µm and $R_b$ = 0.7 µm are shape parameters that determine the size of the merozoite, as illustrated in Figure 8 (a). The main erythrocyte membrane stresses are in the meridian and circumferential directions, see Figure 8 (b). The deformation of the erythrocyte membrane is parameterised using the idealised shape parameters of the malaria merozoite Figure 8 (c), where $L_m$ is the total length of the malaria merozoite, and $d_i$ is the malaria merozoite indentation depth.

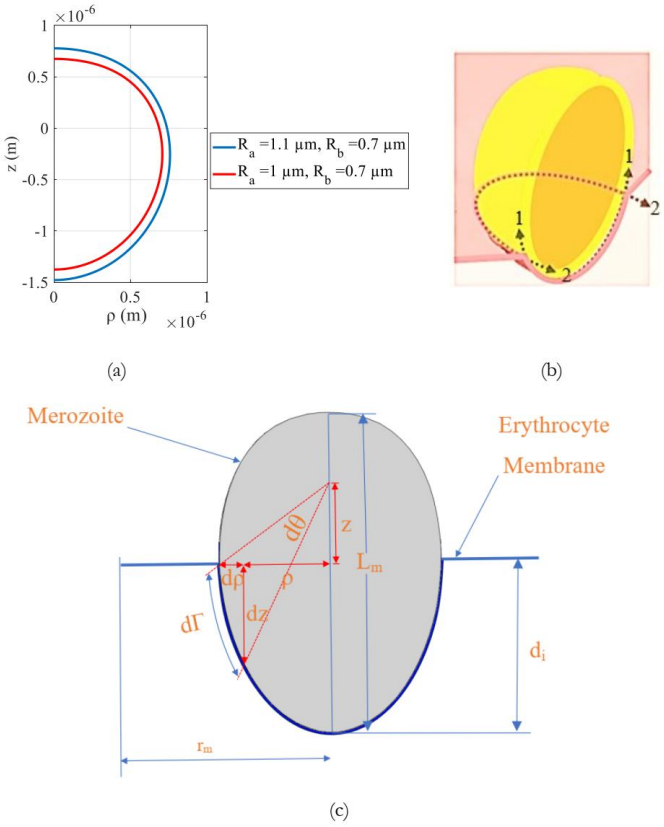


Figure 8: (a) Malaria merozoite idealized shape showing morphological alteration resulting from altering $R_a$ from 1 µm to 1.1 µm, (b) shows the principal stretch directions in the erythrocyte membrane, where 1 and 2 represent the meridian and circumferential directions, respectively, and (c) illustration of the erythrocyte membrane wrapping mechanism.

The erythrocyte membrane is assumed to be flat during the initial contact with the malaria merozoite. The shape parameters $R_a$ and $R_b$ can be used to investigate the impact of shape changes of the malaria

merozoite on its invasion efficiency. Using spherical coordinate parameterization, the x, y, and z coordinates of the surface of the malaria merozoite are expressed as follows (Dasgupta *et al.* 2014):

$$z(\theta) = (1 + \cos\theta)\,[\,2R_a - R_b(1 - \cos\theta)\,]/4 \tag{15}$$

$$x(\theta, \varphi) = \sin\theta\cos\varphi\,[\,2R_a - R_b(1 - \cos\theta)\,]/4 \tag{16}$$

$$y(\theta, \varphi) = \sin\theta\sin\varphi\,[2R_a - R_b(1 - \cos\theta)\,]/4 \tag{17}$$

where θ and φ are polar angles.

The arc length on the egg-shaped merozoite surface is defined using the first fundamental form as follows:

$$d\Gamma_c^2 = \tilde{E}\,d\varphi^2 + 2\,\check{A}\,d\varphi\,d\theta + d\theta^2 \tag{18}$$

where $\tilde{E} = r_\varphi \times r_\varphi$, $\check{A} = r_\theta \times r_\varphi$, $G = r_\theta \times r_\theta$

$$r_\theta = \frac{\partial x}{\partial\theta}\,i + \frac{\partial y}{\partial\theta}\,j + \frac{\partial z}{\partial\theta}\,k \tag{19}$$

$$r_\varphi = \frac{\partial x}{\partial\varphi}\,i + \frac{\partial y}{\partial\varphi}\,j + \frac{\partial z}{\partial\varphi}\,k \tag{20}$$

Letting $\rho^2 = (x^2 + y^2)$, the following matrix of coefficients of the first form is defined:

$$\begin{bmatrix} \tilde{E} & \check{A} \\ \check{A} & G \end{bmatrix} = \begin{bmatrix} \rho^2 & \rho\,\rho'(\sin(\varphi - \theta) \\ \rho\,\rho'(\sin(\varphi - \theta) & \rho'^2 + z'^2 \end{bmatrix} \tag{21}$$

where a single prime represents the first partial derivative with respect to θ.

### 2.2.3 Deformation of erythrocyte membrane during merozoite wrapping

The erythrocyte membrane deformations due to stretching are described in terms of meridian and circumferential stretch as follows:

$$\lambda_1 = 1 + (\Gamma - \rho) / r_m \tag{22}$$

$$\lambda_2 = m \left( \rho / \rho_0 \right)^n + c \tag{23}$$

with

$$\Gamma = \int_0^{\pi} \sqrt{\rho'^2 + z'^2}\ d\theta \tag{24}$$

Here, ρ and z are the Cartesian coordinates of locations on the surface of the rigid merozoite; m, n, and c are parameters that determine the magnitude of the principal stretches of the erythrocyte membrane; and Γ is the coverage length of the erythrocyte membrane on the merozoite surface in the meridian direction. Throughout this chapter, the subscripts 1 and 2 refer to the meridian and circumferential principal directions of the deformed erythrocyte membrane, respectively, shown in Figure 8b

The deformation gradients in meridian and circumferential deformation are then calculated by taking the derivative of Eqns. (22 and (23) as follows:

$$\lambda_1' = \left( \sqrt{\rho'^2 + z'^2} - \rho' \right) / r_m \tag{25}$$

$$\lambda_2' = n\, \rho' \left( \lambda_2 - c \right) / \rho \tag{26}$$

The local erythrocyte membrane bending is characterised by its two principal curvatures, $k_1$ and $k_2$, described as:

$$k_1 = z'\, \rho'' - z''\, \rho' / \left( \sqrt{z'^2 + \rho'^2} \right)^3 \tag{27}$$

$$k_2 = 1/\rho \tag{28}$$

where the single and double prime represent the first and second partial derivatives with respect to θ, respectively.

### 2.2.4 Constitutive law of erythrocyte membrane

A typical erythrocyte model often comprises a Newtonian liquid cytoplasm surrounded by a thin membrane of 0.01 µm in thickness (Hochmuth *et al.* 1973). Erythrocyte membrane constitutive law (Villaggio 1997) described by Eqns.(33) and (34) is determined by considering the erythrocyte membrane as isotropic and incompressible Mooney Rivlin continuum solid. The deformation of the erythrocyte membrane in a microfluidic device has been previously modelled with the Mooney Rivlin law (Zhang and Zhang 2011). The merozoite-induced erythrocyte membrane dissociation was represented by reducing the erythrocyte elastic modulus from 1 kPa to 0.5 kPa. The Mooney Rivlin strain energy density function per reference volume (Skalak *et al.* 1973) is as follows:

$$\psi = C_{10} (I_1 - 3) + C_{01} (I_2 - 3) \tag{29}$$

where $C_{10}$ and $C_{01}$ are empirical material parameters, $I_1$ and $I_2$ are the first and second strain invariants related to the principal stretch $\lambda_1$ and $\lambda_2$ by:

$$I_1 = \lambda_1^2 + \lambda_2^2 + \lambda_1^{-2} \lambda_2^{-2} \tag{30}$$

$$I_2 = \lambda_1^{-2} + \lambda_2^{-2} + \lambda_1^2 \lambda_2^2 \tag{31}$$

The material parameter $C_{10}$ is related to the elastic modulus E of the erythrocyte membrane as follows (Zhang and Zhang 2011):

$$C_{10} = E/6 ( 1 + \beta ) \tag{32}$$

where $\beta$ ranges from 0 to 0.5. The elastic modulus E is of order 1 kPa (Hochmuth *et al.* 1973). The ratio of two Mooney Rivlin material parameters, $\beta = C_{10}/C_{01}$, equals 0.1. The erythrocyte membrane constitutive law is defined using by:

$$\sigma_i = \lambda_i \, d\psi/d\lambda_i \tag{33}$$

$$T_i = h_t \, \sigma_i / \lambda_1 \, \lambda_2 \tag{34}$$

$$T_1 = 2\, h_t \left( \lambda_1\, \lambda_2^{-1} - \lambda_1^{-3}\, \lambda_2^{-3} \right) \left( \partial\psi / \partial I_1 + \lambda_2^{2}\, \partial\psi / \partial I_2 \right) \tag{35}$$

$$T_2 = 2\, h_t \left( \lambda_2\, \lambda_1^{-1} - \lambda_1^{-3}\, \lambda_2^{-3} \right) \left( \partial\psi / \partial I_1 + \lambda_1^{2}\, \partial\psi / \partial I_2 \right) \tag{36}$$

where $h_t$ = 0.01 μm is the thickness of the erythrocyte membrane (Hochmuth *et al.* 1973).

The shear modulus $G_s$ of the erythrocyte membrane is determined by:

$$G_s = \frac{\mu_s}{e_s} \tag{37}$$

with

$$\mu_s = \frac{T_1 - T_2}{2} \tag{38}$$

$$e_s = \frac{\lambda_1^2 - \lambda_2^2}{4} \tag{39}$$

The areal strain $A_s$ of the erythrocyte membrane is expressed by:

$$A_s = \left( \lambda_1\, \lambda_2 - 1 \right) \tag{40}$$

### 2.2.5 Equilibrium equations of erythrocyte membrane

For the contact region between the erythrocyte membrane and the rigid merozoite, the equilibrium equations are given by:

$$\lambda_1^{'}\, dT_1/d\lambda_1 + \lambda_2^{'} dT_1/d\lambda_2 = \rho^{'} (T_2 - T_1)/\rho, \tag{41}$$

$$k_1\, T_1 + k_2\, T_2 = P\,, \tag{42}$$

where P is the pressure exerted on the erythrocyte membrane surface by the malaria merozoite and acting in the direction normal to the erythrocyte membrane surface. The malaria merozoite wrapping

force $F_w$ acts on the surface of the erythrocyte membrane, causing the erythrocyte membrane to wrap the malaria merozoite and is given as follows:

$$F_w = P\, A_w\,, \tag{43}$$

where $A_w$ is the wrapped surface area of the malaria merozoite:

$$A_w = \int_0^{\pi} \int_0^{2\pi} \sqrt{\tilde{E}\, G - \check{A}^2}\, d\theta\, d\varphi. \tag{44}$$

The total indentation force of the malaria merozoite is:

$$F_i = P\, A_p, \tag{45}$$

where $A_p$ is the projected surface area of the erythrocyte membrane

$$A_p = \pi\, \rho^2.$$

The indentation work, which is the energy required by the parasite to invade a human erythrocyte, is:

$$E_i = F_i\, d_i. \tag{46}$$

Where $d_i = (\max(z) + z)$ is the indentation depth.

### 2.2.6 Governing equations of erythrocyte membrane

The governing differential equations for the contact region are:

$$\lambda_1' = z' \left( \frac{g_3 - n\, g_2\, (\lambda_2 - c)}{2\, r_m\, g_1\, \varrho + g_3\, r_m^2 - n\, g_2\, r_m^2\, (\lambda_2 - c)} \right)^{0.5} \tag{47}$$

$$\lambda_2' = n\, \rho' (\lambda_2 - c) / \rho \tag{48}$$

with

$$g_1(\lambda_1, \lambda_2, \theta) = \frac{dT_1}{d\lambda_1},\ g_2(\lambda_1, \lambda_2, \theta) = \frac{dT_2}{d\lambda_2},\ g_3(\lambda_1, \lambda_2, \theta) = T_1 - T_2.$$

The coverage area of the erythrocyte membrane at each step of invasion is expressed as:

$$M_c = \frac{100\left(\int_0^{\pi}\int_0^{2\pi}\sqrt{\tilde{E}G\text{-}\check{A}^2}\,d\theta d\varphi\right)}{A_0}, \quad (49)$$

where $A_0$ is the total surface area of the malaria merozoite.

With the parameter values in Table 2, the solutions of the governing equations can be obtained.

Table 2: Erythrocyte membrane parameters for simulating merozoite wrapping with small and large maximum areal membrane strain of $A_{s,max}$ = 4% and 51%.

| $A_{s,max}$ (%) | E (kPa) | $C_{10}$ (Pa) | $C_{01}$ (Pa) | $r_m$ (μm) | c | n | $\lambda_o$ |
|---|---|---|---|---|---|---|---|
| **4** | 1 | 183 | 18.3 | 50 | 1 | 1 | 1 |
| **50** | 1 | 183 | 18.3 | 4 | 1 | 1 | 1 |

### 2.2.7 Contribution of tight junction and erythrocyte membrane wrapping to invasion energetics

The tight junction forms a mechanical link between the merozoite and erythrocyte membrane to facilitate membrane wrapping. It acts as an anchor location from which the merozoite's actomyosin motors pull the erythrocyte membrane. The parameter values in Table 2 were used for solving the governing equations to simulate the contributions of both the tight junction and the erythrocyte membrane wrapping during small and large strain deformation of the erythrocyte membrane. The tight junction was assumed to exert tension in the circumferential direction at any equilibrium point. In the erythrocyte membrane, a tension acting in the meridian direction was assumed to resist the forces applied by the malaria merozoite. The tensions in the circumferential direction $T_2$ and the meridian direction $T_1$ were used to describe the energetics of the tight junction and the erythrocyte membrane.

### 2.2.8 Impact of erythrocyte membrane damage on the invasion energetics

After attaching to the erythrocyte membrane, the malaria merozoite induces phosphorylation of the erythrocyte membrane skeleton that changes the erythrocyte membrane's mechanical properties (Zuccala and Baum 2011). For example, phosphorylation of band 4.1 weakens the connections between band 4.1, spectrin and actin, which leads to membrane destabilisation (Betz *et al.* 2009). The phosphorylation of β spectrin also leads to decreased membrane stability (Manno *et al.* 1995); tyrosine phosphorylation in SLC4A1 protein weakens the attachment of SLC4A1 to the underlying spectrin network and increases membrane mobility by altering ankyrin binding (Ferru *et al.* 2011). To study

the impact of membrane damage, the elastic modulus of the erythrocyte membrane was reduced from 1 kPa to 0.5 kPa.

## 2.3 Model application and results

The developed model was applied to wrap a merozoite with an erythrocyte membrane. Two cases of maximum areal strain in the erythrocyte membrane were considered, i.e. (i) $A_{s,max}$ = 4% as a generally accepted upper threshold for initiation of cell lysis during quasi-static deformation of the membrane (Li *et al.* 2013), and (ii) $A_{s,max}$ = 51% to investigate larger deformations with an upper threshold of 40% yield areal strain of the erythrocyte membrane (Li *et al.* 2013). The effect of local membrane damage due to phosphorylation by the merozoite was considered by reducing the membrane's elastic modulus. The maximum areal strain in the erythrocyte membrane during merozoite wrapping was implemented in the model using a large circular membrane section with radius $r_m$ = 50 µm (for $A_{s,max}$ = 4%) and a small membrane section with $r_m$ = 4 µm (for $A_{s,max}$ = 51%), and with parameters values specified in Table 2. The merozoite wrapping i.e., when $A_{s,max}$ = 4%, induced maximum principal stretches of $\lambda_{1,max}$ = 1.04 in meridian direction and $\lambda_{2,max}$ = 1.000046 in circumferential direction of the erythrocyte membrane. The maximum circumferential stretch $\lambda_{2,max}$ occurred at a meridian stretch of $\lambda_1$ = 1. (see Figure 9 a). Permitting a higher areal membrane strain of $A_{s,max}$ = 51% during merozoite wrapping resulted in a substantial increase of maximum circumferential and meridian membrane stretch, namely $\lambda_{1,max}$ = 1.5 and $\lambda_{2,max}$ = 1.0375. In this case, the maximum circumferential stretch $\lambda_{2,max}$ occurred at $\lambda_1$ = 1.26 (see Figure 9 b).

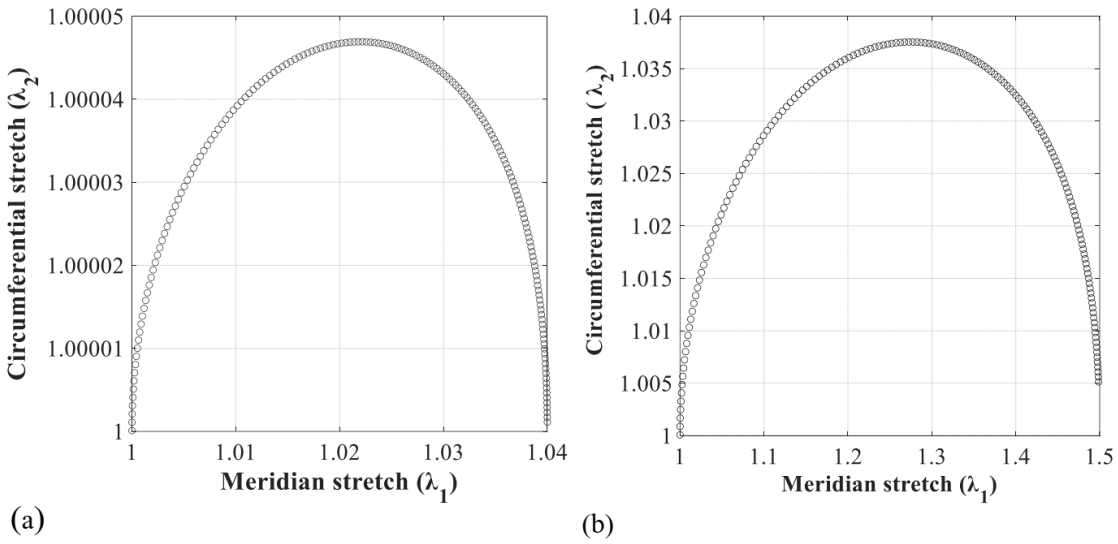


Figure 9: Numerical solution of circumferential stretch $\lambda_2$ versus meridian stretch $\lambda_1$ for the complete wrapping of the merozoite for (a) small maximum areal strain of $A_{s,max}$ = 4% and (b) for large maximum areal strain of $A_{s,max}$ = 51% in the erythrocyte membrane.

The analytical model predicts larger erythrocyte membrane stretch in the meridian direction than circumferential direction for both small and finite erythrocyte membrane areal strain when the indentation depth is 100% (see Figure 10 and Figure 11).

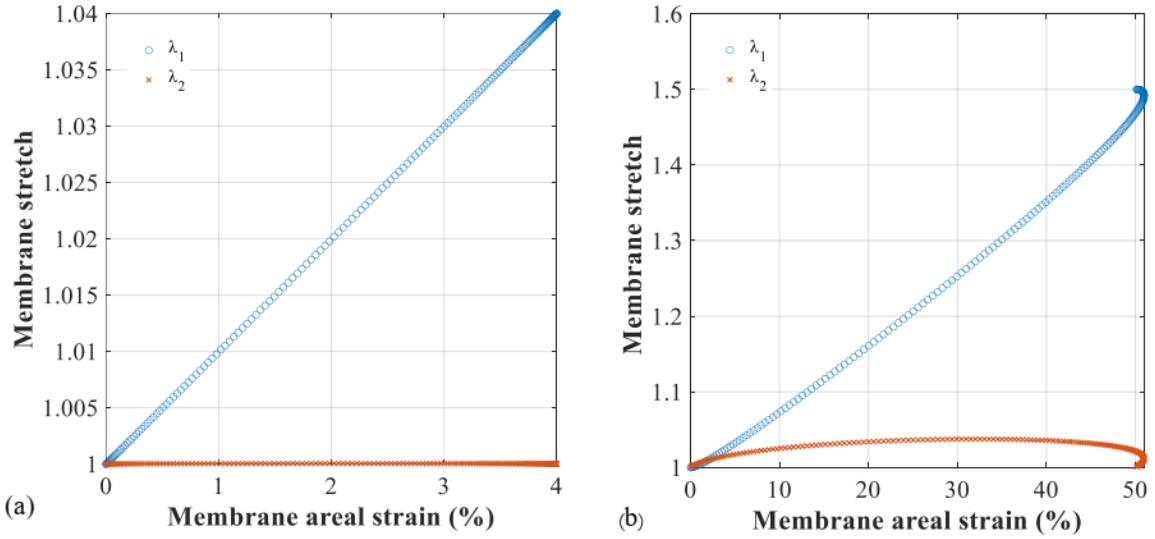


Figure 10: Numerical solution of meridian stretch $\lambda_1$ and circumferential stretch $\lambda_2$ versus the erythrocyte membrane areal strain for the complete wrapping of the merozoite for (a) small maximum areal strain of $A_{s,max}$ = 4% and (b) for large maximum areal strain of $A_{s,max}$ =51% in the erythrocyte membrane.

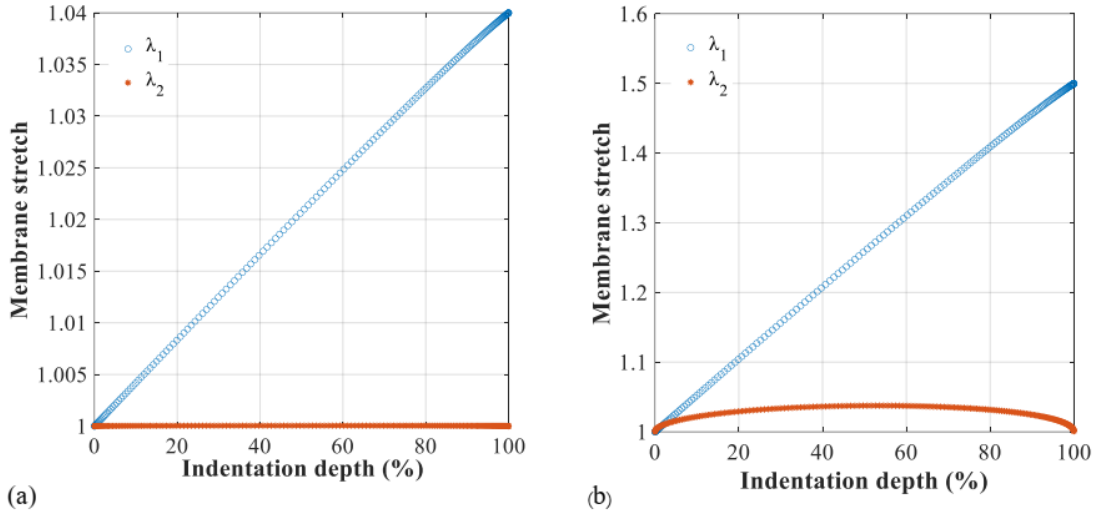


Figure 11: Analytical solution describing erythrocyte membrane stretch versus percentage indentation depth for (a) small maximum areal strain of $A_{s,max}$ = 4% and (b) for large maximum areal strain of $A_{s,max}$ =51% in the erythrocyte membrane.

The membrane tension induced by the circumferential and meridian stretches reflects a near-linear constitutive response of the erythrocyte membrane for small deformations up to $A_{s,max}$ = 4%. The erythrocyte membrane's non-linear elastic response with strain softening is apparent for large deformation, e.g. $A_{s,max}$ = 51% (see Figure 12 b, d). For the model with the large membrane section of $r_m$ = 50 µm, the predicted non-dimensional membrane tension in $T_1$ direction agrees better with the Neo-Hookean based non-dimensional tension than Mooney-Rivlin based non-dimensional tension (Omori *et al.* 2011a) (Figure 12 a, c). However, for the large erythrocyte membrane deformation, the

model predictions in $T_1$ direction fit the experimentally based Hooke's law solution better for the small membrane section of $r_m$ = 4 µm (see Figure 12 b).

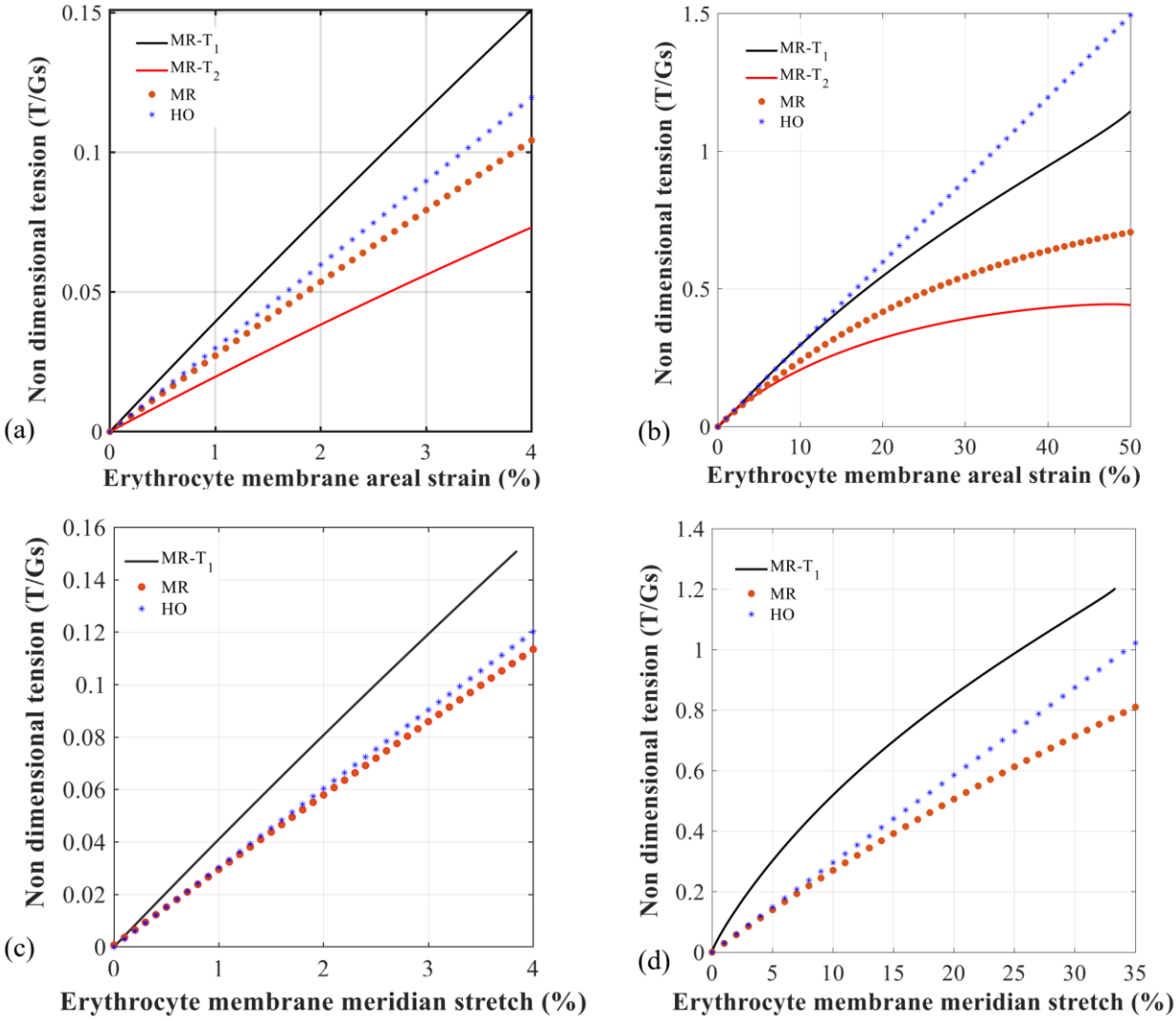


Figure 12: Non-dimensional isotropic tension versus areal strain in the erythrocyte membrane during merozoite wrapping for the maximum areal strain of $A_{s,max}$ = 4% (a) and 51% (b). Mathematical solutions of the tension in meridian (MR-$T_1$) and circumferential direction (MR-$T_2$) obtained with the Mooney-Rivlin law, see Eqns. (35) and (36), are compared to solutions of linear-elastic Hooke's law (HO) and the nonlinear elastic Mooney-Rivlin law (MR) from Omori *et al.* (2011b).

The erythrocyte membrane's strain-softening was also observed by a decreasing shear modulus with increasing areal strain (see Figure 13 a**)**. The meridian and circumferential membrane stresses associated with an areal strain of $A_{s,max}$ = 4% are $\sigma_1$ = 63.1 Pa and $\sigma_2$ = 30.5 Pa (see Figure 13 b).

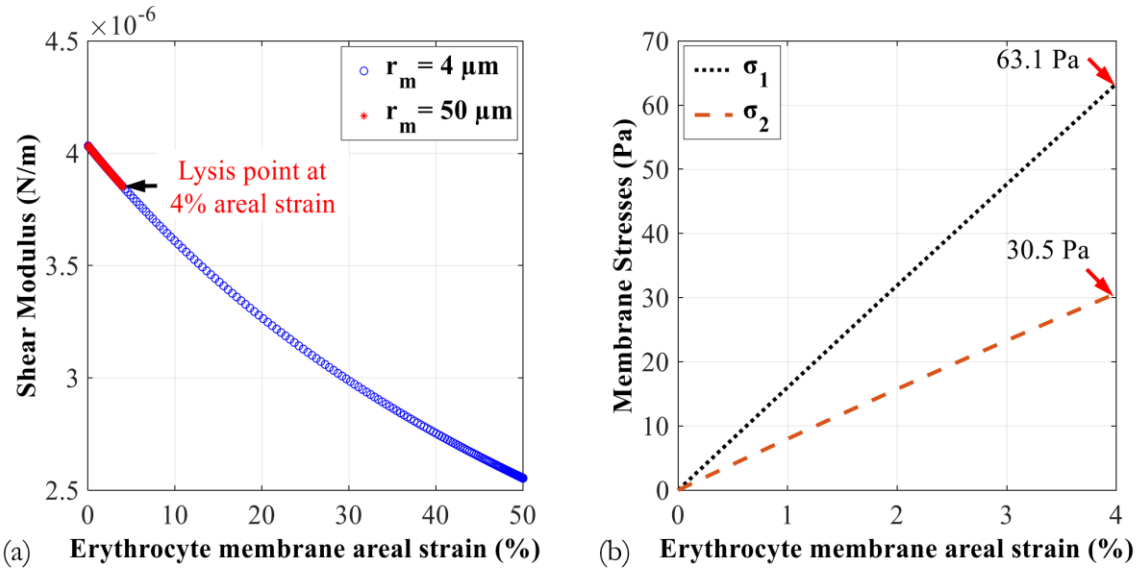


Figure 13: (a) Membrane shear modulus versus areal strain in the erythrocyte membrane during complete merozoite wrapping of the erythrocyte membrane. The decrease of the shear modulus with increasing areal strain represents strain softening. (b) Meridian and circumferential stress versus areal strain in the erythrocyte membrane during complete merozoite wrapping. The stress associated with the assumed lysis threshold areal strain of $A_{s,max}$ = 4% is $\sigma_1$ = 63.1 Pa in meridian and $\sigma_2$ = 30.5 Pa in the circumferential direction.

The total indentation force $F_i$ during membrane wrapping was predicted to increase nearly linearly up to a normalised indentation depth of 85.2% and decrease after that. The magnitude of $F_i$ was higher for larger maximum areal membrane strain; however, the maximum indentation force $F_i$ occurred at the same normalised indentation depth (see Figure 14 b). The result in Figure 14 illustrates that a large surface area of the erythrocyte membrane results in smaller magnitudes of total wrapping and total indentation, implying that the malaria merozoite becomes more invasive for a larger erythrocyte surface area.

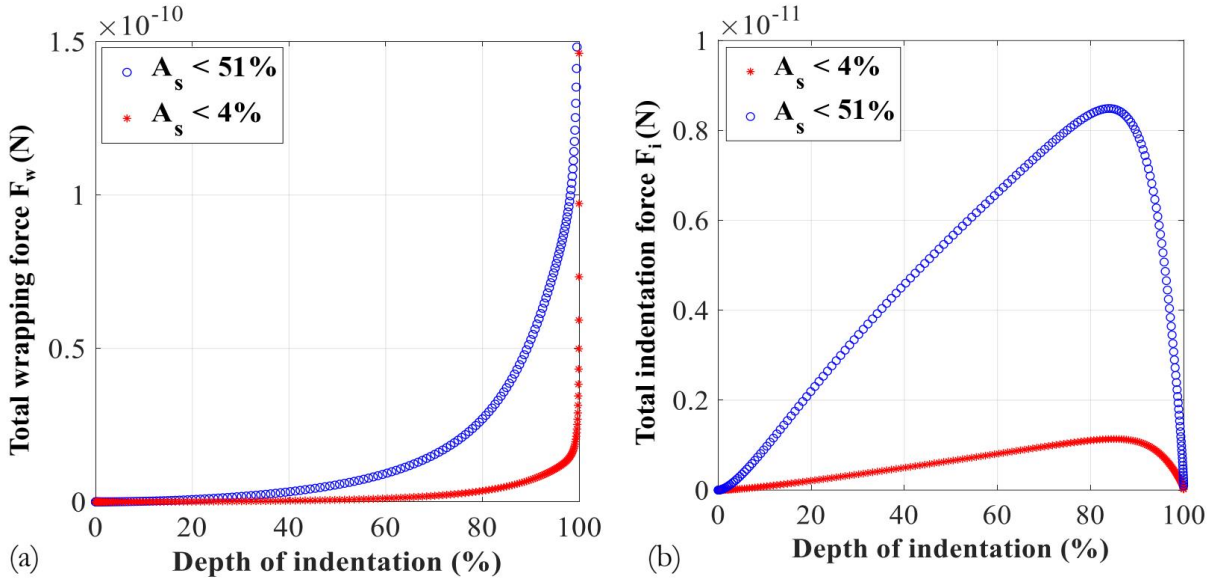


Figure 14. Forces involved in the complete wrapping of a merozoite for small ($A_{s,max}$ = 4%) and large maximum areal strain ($A_{s,max}$ = 51 %) in the erythrocyte membrane. (a) Total wrapping force $F_W$ versus normalised indentation depth $d_i/L_m$. (b) Total indentation force $F_I$ versus normalised indentation depth $d_i/L_m$. The total indentation force acts in the direction of the long axis of the merozoite.

The total indentation work $E_i$, required by the merozoite to overcome the barrier energy imposed by the erythrocyte membrane, increases with increasing indentation. $E_i$ reaches a maximum at the same normalised indentation depth at which the total indentation force is largest (see Figure 15 a). A reduction of the erythrocyte membrane's elastic modulus from 1 to 0.5 kPa (to simulate weakening of the membrane due to phosphorylation of the spectrin network) led to the reduction of the total indentation energy by 50%, implying that the phosphorylation increases the merozoite's invasiveness (Figure 15 b).

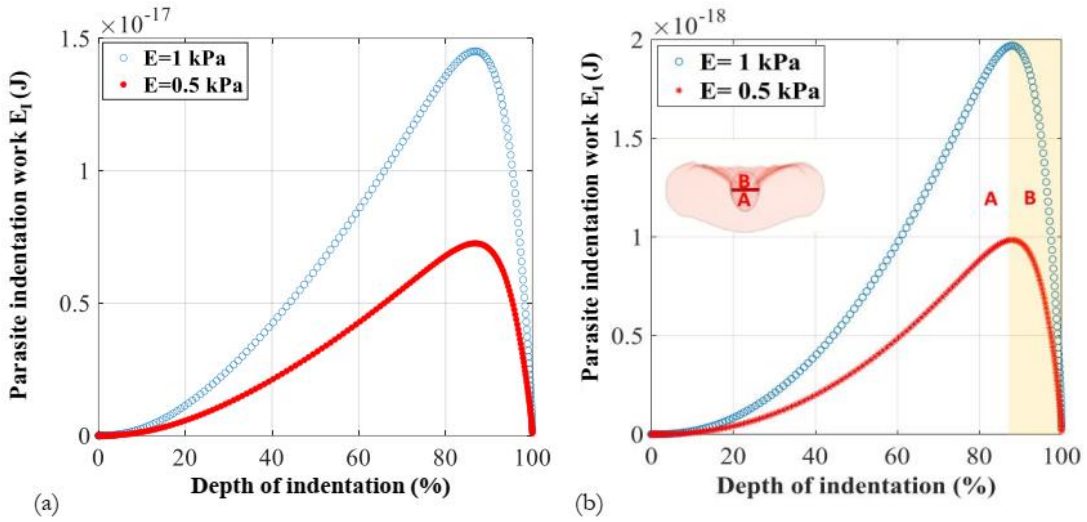


Figure 15: Indentation work required for the complete wrapping of the merozoite versus normalised indentation depth. (a) Indentation work for $A_{s,max}$ = 51 %, without and with phosphorylation of the spectrin network, represented by reducing the membrane's elastic modulus. (b) Indentation work for $A_{s,max}$ = 4 %, without and with phosphorylation of the spectrin network, represented by reducing the membrane's elastic modulus. A represents the indentation depth region where the indentation work is done by the malaria merozoite, whereas B indicates the part of the indentation for which the tight junction provides the work.

## 2.4 Discussion

An analytical model for wrapping a malaria merozoite by the erythrocyte membrane was developed, and the effects of the membrane area and damage through phosphorylation were studied. In the developed analytical model, the effect of the tight junction has been incorporated by defining the line tension acting in the circumferential direction of the erythrocyte membrane with an initial radius $\rho_o$. The total energy required for a successful invasion is determined by computing the total work done by the malaria merozoite. The results from the developed analytical model suggest that during the early stage of active invasion, the work done by the malaria merozoite increases progressively and is stored in the form of internal energy in the tight junction and erythrocyte membrane. This energy is utilised during the late phase of the invasion, facilitating the sealing of the erythrocyte membrane. The simulations with the developed mathematical model describe two types of erythrocyte membrane wrapping. One type involves a small areal strain in the erythrocyte membrane when the malaria merozoite interacts with a large region of the erythrocyte membrane. The second type involves a large areal strain in the erythrocyte membrane induced when the malaria merozoite interacts with a small erythrocyte membrane region.

By analysing the two types of membrane wrapping, the model reveals new insights into the mechanics of erythrocyte invasion by the malaria merozoites. For instance, the reduction in the magnitudes of the

malaria merozoite wrapping force and indentation force in Figure 14 illustrates that the malaria merozoite is more invasive for a lower areal strain, i.e. 4%, compared to a higher maximum erythrocyte membrane areal strain, i.e. 51%. This finding demonstrates that the malaria merozoite optimises its invasion efficiency by minimising its induced strain in the erythrocyte membrane. Additionally, recent data from (Introini *et al.* 2022) indicates that the wrapping energy for the control population is in range of $1.40 \times 10^{-17}$ J, which is equal to the parasite indentation work predicted by the developed analytical model for a 51% areal membrane strain hence supporting the validity of the developed model.

Similarly, the decrease of the malaria merozoite wrapping and indentation forces with increasing erythrocyte membrane surface area demonstrates that the malaria merozoite's invasiveness depends on the surface area of the erythrocyte membrane (see Figure 14). It is known that discoid shaped erythrocytes are more deformable than ellipsoidal or spherical erythrocytes (Li *et al.* 2018).The increased deformability is based on the larger surface to volume ratio (S/V) of the discoid shape compared to spherical and elliptic shapes, the latter often resulting from hereditary disorders such as spherocytosis, elliptocytosis. However, it has been unknown whether the discoid shape of the erythrocyte provides an advantage to the entry of malaria merozoites. With the developed analytical model, the impact of the erythrocyte membrane surface area on the invasiveness of the malaria merozoite has been established. The malaria merozoite becomes more invasive when a larger erythrocyte membrane area is involved in the wrapping interaction (see Figure 14 a and b). This finding can also partly explain why individuals with abnormal erythrocyte morphologies, e.g., caused by spherocytosis, elliptocytosis, and sickle cell anaemia, are less susceptible to being infected with malaria. However, further analysis is needed to quantify the impact of surface to volume ratio on the invasiveness of the malaria merozoite. To study the effect of merozoite-induced damage, the material parameter of the Mooney Rivlin law was altered such that the initial elastic modulus of the erythrocyte membrane was reduced from 1 kPa for the intact membrane to 0.5 kPa for the membrane with damage. The results from the developed analytical model indicate that reduction of erythrocyte membrane elastic modulus led to the decrease in the work done or energy required by the malaria merozoite to invade the erythrocyte. This decrease in work and energy demonstrates that the malaria merozoite becomes more invasive in the presence of damage in the erythrocyte membrane. Hence the analytical model reveals that the change of elastic modulus of the erythrocyte membrane affects the invagination energies and is a potential target for invasion blocking antimalarial drugs, thus leading to the development of efficacious drugs that target the invasions process.

The erythrocyte membrane response in the meridian direction obtained by the developed analytical model agrees better with the Mooney Rivlin model of a thin rubber membrane subjected to an equibiaxial strain. The noticeable differences between the predictions of the analytical model and the previous numerical data is due to the difference in the loading modes (see Figure 12 b).

# 3 A constitutive model for the remodelling erythrocyte membrane skeleton during the active invasion by the malaria merozoite

## 3.1 Introduction

A biological cell membrane is an organelle of the biological cell that provides selective permeability to many solutes required for its nutrition. Biochemical or mechanical damage of the cell membrane often disrupts the normal cell membrane functions, leading to severe cellular injury. Breakdown or disruption of the cell membrane can result in the influx of potentially toxic chemicals, the release of vital cellular nutrients, and the elimination of solute gradients across the cell membrane, crucial for maintaining cell life. Like in many biological cells, the erythrocyte membrane acts as a mechanical structure and a chemical barrier that allows the erythrocyte to undergo large nonlinear elastic deformations and regulate transport processes across it. Hence, any persistent disruption of the erythrocyte membrane can impair various physiological functions of the erythrocyte.

When the malaria merozoite invades the human erythrocyte, it evades its destruction by the host immune system. Hence the malaria merozoite must invade the human erythrocyte without breaching the membrane barrier to avoid erythrocyte cell death. Erythrocyte membrane damage can be categorised into two groups: biochemical damage involving chemically induced kinetic reaction, leading to the reorganisation of the erythrocyte membrane skeleton, and biomechanical damage due to membrane strain. During the malaria merozoite invasion, the erythrocyte membrane's chemical damage is induced by the binding of erythrocyte binding antigen (EBA-175) to the glycophorin A (GPA), the erythrocyte receptor that initiates biochemical signalling cascades. The complex signalling cascades involves the phosphorylation of the critical membrane skeleton proteins such as ankyrin and spectrin, resulting in considerable changes in the mechanical properties of the erythrocyte membrane. The erythrocyte binding antigen 175 (EBA-175) is a plasmodium falciparum merozoite antigen produced by micronemes. The micronemes secrete EBA-175 that binds to the GPA through the apical region of the malaria merozoite. It has been demonstrated by nano-indentation that EBA-175 reduces the elastic modulus and thus increases the deformability of the erythrocyte membrane (Sisquella *et al.* 2017). The primary mechanism associated with the reduction in the erythrocyte membrane elastic modulus is EBA-175 activated phosphorylation. In general, phosphorylation and dephosphorylation of membrane proteins is an essential mechanism by which properties of the erythrocyte membrane are regulated (Mohandas and Gallagher 2008).

Additionally, protein phosphorylation controls many cellular functions, including protein synthesis, transcription, and signal transduction to regulate cellular responses (Cohen 2000, 2002). The malaria merozoite manipulates these pathways to modify the properties of the erythrocyte membrane during the invasion process (Zuccala *et al.* 2016). To date, there is no damage model to predict the malaria merozoite induced damage. Hence this study aims to develop a constitutive model for the remodelling of the erythrocyte membrane.

The erythrocyte membrane skeleton is a dense network of proteins. This network provides the erythrocyte membrane's mechanical strength, allowing the cell to withstand mechanical loads as it flows through the narrow blood vessels. It comprises a unique arrangement of spectrin, F-actin, protein 4.1, and ankyrin with direct and indirect connections to the lipid bilayer. The importance of the protein network of the erythrocyte membrane skeleton in maintaining the discoid shape and elasticity of a healthy erythrocyte has been highlighted in various studies involving erythrocytes with hereditary disorders. Spectrin proteins form a large part of the erythrocyte membrane skeleton and are responsible for the elastic deformation of the cell. Apart from providing mechanical strength to the erythrocyte membrane, the spectrin network acts as the structural platform for stabilising and activating membrane channels, receptors, and transporters (Machnicka *et al.* 2014).

Several studies have described molecular factors responsible for altering the elastic behaviour of the erythrocyte membrane. However, the impact of the erythrocyte membrane remodelling on the malaria merozoite's invasiveness is not well understood. This limitation in knowledge is due to the difficulty of studying structural changes of protein networks and quantifying the mechanical properties during the short invasion process of less than 30 s. Continuum damage mechanics modelling (CDM) provides an alternative approach for predicting and studying erythrocyte membrane damage during the invasion.

Theoretical models can generally allow the investigation of complex biological systems and avoid costly experimental studies. However, the numerical studies of these biological materials require knowledge of their constitutive models. Several strain-based constitutive damage models for soft biological tissue have been previously developed and implemented in a finite element framework. There is growing interest in computational damage mechanics related to soft biological tissue because studying disease mechanisms is less cumbersome when conducted in silico. In silico studies can also lead to testing devices for studying disease mechanisms and drug interaction with diseased cells or tissue. Erythrocyte membrane damage mechanism can be studied by using in silico simulations derived from computational finite element analysis. With this approach, the mechanics associated with the phosphorylation events during the invasion of erythrocytes can be predicted and analysed.

In this chapter, a new constitutive model of the erythrocyte membrane with a remodelling function is presented. The model has been applied for simulating merozoite induced phosphorylation events and applied to investigate the impact of the malaria merozoite induced erythrocyte membrane remodelling on the invasiveness of malaria merozoite (chapter 4). To model erythrocyte membrane damage due to phosphorylation, the internal state variable or damage variable from the field of continuum damage mechanics is used to represent the phosphorylation state of spectrin which is thought to (1) alter the protein conformation, (2) influence dissociation of proteins, (3) cause dissociation of protein skeleton from lipid bilayer, and (4) induce a membrane bending moment. With suitable parameterisation of the damage variables, the developed erythrocyte membrane damage model can elucidate the energetics of erythrocyte membrane damage which is challenging to investigate experimentally. Additionally, the model can also be applied to study repair mechanisms of various biological cells. The model can be further used for studying damage processes involving both chemical and strain-based damage.

## 3.2 Methods and materials

### 3.2.1 Mathematical model of the constitutive behaviour of the damaged erythrocyte membrane

In this section, the mathematical details used in the development of the constitutive model of the erythrocyte membrane subjected to chemical damage has been presented. The hyperelastic constitutive response (Bower 2010) of a healthy erythrocyte membrane was defined by the Helmholtz free-energy function $\psi_h$ in Eqn. (50) (Bergstrom 2015). The deformation of the erythrocyte membrane in a microfluidic device has been previously modelled with the Mooney Rivlin law (Zhang and Zhang 2011). To model the material response of the erythrocyte membrane due to chemical damage, the Helmholtz free energy function, a thermodynamic potential that measures the useful work obtainable from an isochoric and isothermal thermodynamic system, was modified by incorporating a damage reduction function $R_d$ in Eqn. (56).

$$\psi_h = U_h - T_h S_h \tag{50}$$

Where $\psi_h$ is the Helmholtz free energy, $U_h$ is the system's internal energy, $T_h$ is the absolute temperature of the surroundings, modelled as a heat bath, $S_h$ is the entropy of the systems. The deformation of the erythrocyte membrane is mainly due to the mechanical load exerted by the malaria merozoite through its actomyosin machinery plus other external loads such as blood pressure. Hence the energetics associated with entropy was not considered. Thus, the Helmholtz free energy function for the erythrocyte membrane deformation was only represented as internal energy. Therefore, damage

induced by the malaria merozoite was modelled by modifying the strain energy density function of the erythrocyte membrane. The strain energy density function of the erythrocyte membrane is usually

presented in a decoupled form comprising deviatoric and isochoric terms because the erythrocyte membrane is primarily made up of an elastic network of spectrin and can be considered as an elastic isotropic and nearly incompressible continuum. For nearly incompressible hyperelastic materials, the combination of incompressibility and large deformations presents extreme difficulties for a displacement-based finite element method. The reason is that the constraint J = det F = 1 on the deformation field is highly nonlinear (Weiss 1994). Hence, a displacement-based finite element scheme must invoke a small change measure of volumetric deformation to overcome this challenge. Consequentially, the deformation gradient was decomposed into the dilatational and deviatoric parts to apply separate numerical treatments to each part (Weiss 1994). Therefore, the deformation gradient F and the left Cauchy-Green strain tensor B was divided into the volume changing (dilatational) and the volume-preserving (distortional) parts, an approach often used in elastoplasticity (Ogden 1978). The strain energy density function of the isotropic erythrocyte membrane was expressed in terms of the left Cauchy deformation tensor as follows:

$$B = F \cdot F^T \tag{51}$$

where $F = R\,U$ and $F^T = R^T U^T$, R is a rotation matrix, and U is a stretch tensor, and this gives the following equation:

$$B = RU \cdot U^T R^T = U \cdot U^T \tag{52}$$

This shows that B, the left Cauchy deformation tensor, is a stretch tensor and isotropic. Hence the strain energy density function ψ of a damaged erythrocyte were written in terms of invariants of the left Cauchy-Green deformation tensor as follows:

$$\psi\,(I_1, I_2, J, \tau) = R_d\,[\,\psi_0(I_1, I_2) + \psi_0\,(J)\,] \tag{53}$$

where,

$$I_1 = \text{trace}\,(B),$$

$$I_2 = \frac{1}{2}\,(I_1^2 - B{\cdot\cdot}B),$$

$$J = \sqrt{\text{Det}\,(B)},$$

B is the left Cauchy-Green tensor, and $R_d$ is the reduction factor, $\psi_0$ is the strain energy density of an intact erythrocyte membrane, τ is the indentation time in seconds.

The continuum damage mechanics framework for material stiffness deterioration suitable for implementation in Abaqus Explicit was used to simulate chemical damage induced by a malaria merozoite during the entry process. The model borrows some concepts from various strain-based damage models for soft biological materials and biodegradable polymers where constitutive hydrolytic degradation and time-dependent behaviour are described (Vieira *et al.* 2011). The phosphorylation of the critical membrane skeleton proteins was assumed to induce alterations to both the deviatoric and the volumetric components of the strain energy density function. Hence, the induced phosphorylation of the membrane skeleton proteins was considered to alter elastic stiffness and the compressibility of the erythrocyte membrane. Hence the shear elastic modulus and the compressibility K of the erythrocyte membrane are related as follows:

$$K = \frac{4}{3} R_d \left( \frac{C_{10} + C_{01}}{1 - 2\nu} \right) ( 1 + \nu ) \tag{54}$$

$$\mu = 2 ( C_{10} + C_{01} ) \tag{55}$$

where the damage reduction factor, Poisson's ratio, and the shear modulus are denoted as $R_d$, $\nu$, $\mu$, respectively. The damage reduction factor $R_d$ is a function of chemical, mechanical damage parameters and is defined as follows:

$$R_d( B,\ J, \tau ) = \left[ 1 - \beta_2 \right] e^{-( \beta_1 \tau + \beta_2 \psi_0 )} \tag{56}$$

where B and J denote the left Cauchy green tensor and the volumetric strain of intact erythrocyte membrane, respectively, $\tau$ is the simulation time, and $\psi_0$ is the strain energy density per reference volume of the intact erythrocyte membrane. The chemical damage parameter is denoted as $\beta_1$, and the strain or mechanical damage parameter is denoted as $\beta_2$, and. When $\beta_2 = 0$, the damage mode is 100% chemical damage, i.e., damage of the erythrocyte membrane is not due to strain. Thus, $\beta_1$ represents chemical damage due to various modes of phosphorylation, and $\beta_2$ represents mechanical damage associated with the tearing or rupturing of the protein chains in the erythrocyte membrane skeleton. The erythrocyte's compressibility was defined using Poisson's ratio of 0.499, which is a nearly incompressible state. For incompressible materials, the contribution of the volumetric strain energy density function is neglected since J = 1. However, the erythrocyte membrane is nearly incompressible; as such, the following deviatoric strain invariants were used:

$$\bar{I}_1 = J^{-2/3} I_1 \tag{57}$$

$$\bar{I}_2 = J^{-4/3} I_2 \tag{58}$$

The variation of the strain energy potential is by definition equal to the internal virtual work per reference volume $V_0$, and this can be written as follows:

$$\delta W_i = \int J \left( S : \delta e - p \delta \epsilon^{vol} \right) dV^0 = \int \delta \psi \, dV^0 \tag{59}$$

where

$$\delta \psi = 2 \left[ \left( \frac{\partial \psi}{\partial \bar{I}_1} + \bar{I}_1 \frac{\partial \psi}{\partial \bar{I}_2} \right) B^* - \frac{\partial \psi}{\partial \bar{I}_2} B^* \cdot B^* \right] : \delta e + J \frac{\partial \psi}{\partial J} \delta \epsilon^{vol} ,$$

$$\delta e = \delta D - \frac{1}{3} \delta \epsilon^{vol} I ,$$

$$\delta D = sym \left( \delta L \right) = \frac{1}{2} \left( \delta L + \delta L^T \right) ,$$

$$\delta \epsilon^{vol} = I : \delta D ,$$

$$\delta L = \frac{\partial \delta u}{\partial X} ,$$

$$S = \sigma + pI ,$$

$$p = - \frac{1}{3} I : \sigma = - \frac{\partial \psi}{\partial J} ,$$

Hence deviatoric stress can be rewritten as:

$$S = \frac{2}{J} DEV \left[ \left( \frac{\partial \psi}{\partial \bar{I}_1} + \bar{I}_1 \frac{\partial \psi}{\partial \bar{I}_2} \right) B^* - \frac{\partial \psi}{\partial \bar{I}_2} B^* \cdot B^* \right] \tag{60}$$

$$S = \frac{2}{J} \left[ \left( \frac{\partial \psi}{\partial \bar{I}_1} + \bar{I}_1 \frac{\partial \psi}{\partial \bar{I}_2} \right) \left( B^* - \frac{trace \left( B^* \right)}{3} \right) - \frac{\partial \psi}{\partial \bar{I}_2} \left( B^* \cdot B^* - \frac{trace \left( B^* \cdot B^* \right)}{3} \right) \right] \tag{61}$$

And therefore stress (deviatoric stress + volumetric stress) is written as follows:

$$\sigma_{ij}=\frac{R_d}{J}\left[\frac{1}{J^{2/3}}\left(\frac{\partial \psi_0}{\partial \bar{I}_1}+\bar{I}_1\frac{\partial \psi_0}{\partial \bar{I}_2}\right)B_{ij}-\left(\bar{I}_1\frac{\partial \psi_0}{\partial \bar{I}_1}+2\bar{I}_2\frac{\partial \psi_0}{\partial \bar{I}_2}\right)\frac{\delta_{ij}}{3}-\frac{1}{J^{\frac{4}{3}}}\frac{\partial \psi_0}{\partial \bar{I}_2}B_{ik}B_{kj}\right]+\frac{R_d\partial \psi_0}{\partial J}\delta_{ij} \quad (62)$$

$$\sigma_{ij}=\frac{e^{-(\beta_1\tau)}}{J}\left[\frac{1}{J^{2/3}}(C_{10}+\bar{I}_1C_{01})B_{ij}-(\bar{I}_1C_{10}+2\bar{I}_2C_{01})\frac{\delta_{ij}}{3}-\frac{1}{J^{\frac{4}{3}}}C_{01}B_{ik}B_{kj}+\frac{KinJ}{J}\delta_{ij}\right] \quad (63)$$

where $\delta$ is the Kronecker delta function and $\psi_0$ is the Mooney Rivlin strain energy density function per unit reference volume of the intact erythrocyte membrane, rewritten as follows:

$$\psi_0 = C_{10}(\bar{I}_1-3)+C_{01}(\bar{I}_2-3)+\frac{1}{2}K(\text{in }(J))^2 \quad (64)$$

### 3.2.2 Implementation and verification of the modified Mooney Rivlin model as user material in Abaqus Explicit

Abaqus Explicit analysis involves numerically solving equilibrium equations. The equilibrium solution is represented in terms of the stretch tensors, deformation gradients, or strain tensors. In order to calculate stresses, the Abaqus Explicit algorithm can either use the materials module with the Mooney Rivlin law definition or the VUMAT subroutine with a suitable material definition. In the developed FEA model, the VUMAT subroutine was used to simulate merozoite-induced damage using the approach illustrated in Figure 16. The detailed VUMAT subroutine is attached as supplementary information in appendix A.

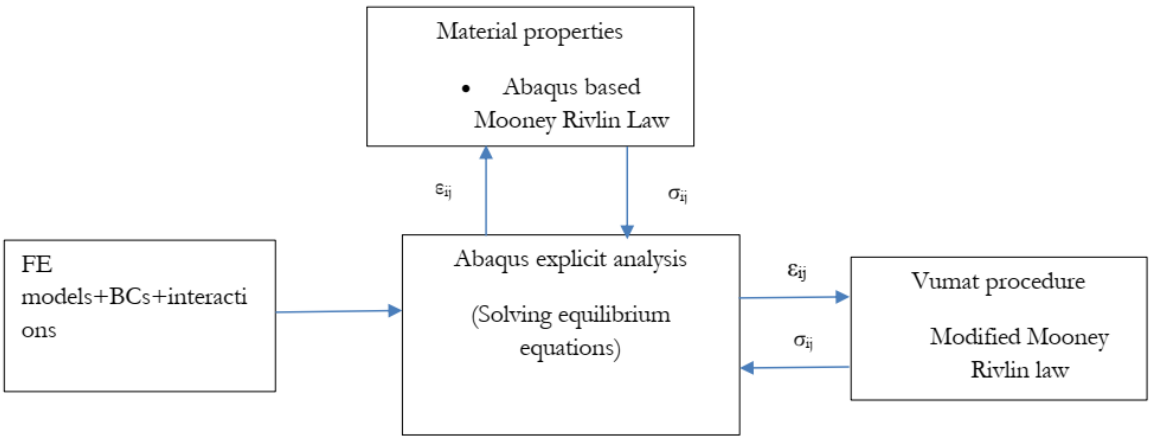


Figure 16: Abaqus Explicit procedure for simulating erythrocyte membrane by using the VUMAT subroutine. The Abaqus materials module is used to define the Abaqus based Mooney Rivlin law.

The implementation step begins with verifying the accuracy of the developed VUMAT subroutine by comparing the true stresses defined by the Mooney Rivlin law in the Abaqus Explicit materials module with the true stresses defined by the developed VUMAT subroutine when $\beta_1$ is set to 0. When the damage parameter $\beta_1$ is set to 0 in the developed VUMAT subroutine, the constitutive response is that of an intact erythrocyte membrane and theoretically equal to the response of the Mooney Rivlin law built in the Abaqus Explicit materials module.

This verification step was achieved by subjecting a single shell element to an equi-biaxial strain of 110%, see Figure 17. The Mooney Rivlin law refers to the standard model built-in Abaqus, whereas the erythrocyte membrane damage model refers to the model developed in the current study that is based on the Mooney Rivlin model to represent an erythrocyte membrane with merozoite-induced damage.

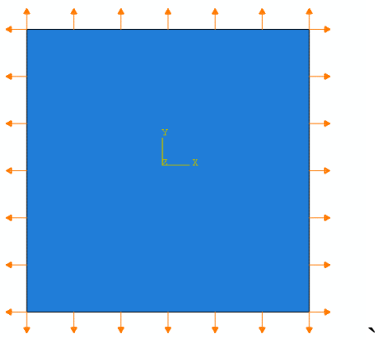

Figure 17: Biaxially loaded shell element used to verify the VUMAT subroutine.

After verifying the developed erythrocyte membrane damage model, it is then implemented on the single shell element to simulate various degrees of chemical damage. This approach allows the

evaluation of the stability of the developed erythrocyte membrane damage model, assessed by using Drucker's stability criterion.

### 3.2.3 Representing erythrocyte membrane damage in alternative constitutive models

In some instances, implementing the erythrocyte membrane damage model may not be desired or possible. For such cases, the suitability of other constitutive models (built-in in Abaqus) to represent erythrocyte membrane damage was determined. A standard equibiaxial test was simulated in Abaqus with the Evaluate option using nominal stress and strain data obtained from the developed erythrocyte membrane damage model for $\beta_1$ = 0, 0.49, 1 and 2.7. The test resulted in the following constitutive models' parameter values and stability thresholds.

- Ogden model:

$$\psi_{ogd} = \sum_{i}^{N} \frac{2\mu_i}{\alpha_i^2} \left( \left( J^{-\frac{1}{3}}\lambda_1 \right)^{\alpha_i} + \left( J^{-\frac{1}{3}}\lambda_2 \right)^{\alpha_i} + \left( J^{-\frac{1}{3}}\lambda_3 \right)^{\alpha_i} - 3 \right) + \sum_{i=1}^{N} \frac{1}{D_i} \left( J^{el} - 1 \right)^{2i} \tag{65}$$

  where $\lambda_i$, ( i = 1, 2, 3 ) are the principal stretches, N is the number of material parameters, $\mu_i$, $\alpha_i$, $D_i$ are temperature-dependent material parameters, and $J^{el}$ is the elastic volume ratio.

- Yeoh model:

$$\psi_{yeoh} = C_{10} \left( J^{-\frac{2}{3}} I_1 - 3 \right) + C_{20} \left( J^{-\frac{2}{3}} I_1 - 3 \right)^2 + C_{30} \left( J^{-\frac{2}{3}} I_1 - 3 \right)^2 + \frac{1}{D_1} \left( J^{el} - 1 \right)^2 + \frac{1}{D_2} \left( J^{el} - 1 \right)^4 + \frac{1}{D_3} \left( J^{el} - 1 \right)^6 \tag{66}$$

  where $I_1 = \lambda_1^2 + \lambda_2^2 + \lambda_3^2$, $\psi_{yeoh}$ is the strain energy per reference volume unit, and $C_{i0}$ and $D_i$ are temperature-dependent material parameters.

- Reduced Polynomial model:

$$\psi_{RP} = \sum_{i}^{N} C_{i0} \left( J^{-\frac{2}{3}} I_1 - 3 \right)^i + \sum_{i=1}^{N} \frac{1}{D_i} \left( J^{el} - 1 \right)^{2i} \tag{67}$$

  where $\psi_{RP}$ is the strain energy per reference volume unit, N is the number of material parameters, $C_{i0}$ and $D_i$ are temperature-dependent material parameters, and $I_1$ is the first strain invariant.

## 3.3 Results

### 3.3.1 Erythrocyte membrane damage model

The true stresses defined by the Abaqus built-in Mooney Rivlin material model and the erythrocyte membrane damage VUMAT based model agreed well for the intact membrane, i.e., when $\beta_1 = 0$, and for true strain between 0 and 110% (see Figure 18 a). This agreement indicates that the developed VUMAT subroutine was accurately implemented. When the damage parameter is changed from the intact state, i.e. when $\beta_1 = 0$, to the damaged state, i.e. when $\beta_1 = 2.7$, the in-plane true stress and the largest in-plane maximum principal stress at 110% true strain, decreases, see Figure 18 (b) and Figure A.1. The in-plane true stress decreases from 0.0048 MPa (for $\beta_1 = 0$) to 0.0028 MPa (for $\beta_1 = 0.49$), 0.0016 MPa (for $\beta_1 = 1$) and to 0.00025 MPa ( for $\beta_1 = 2.7$), when the true strain is 110% see Figure 18 (b).

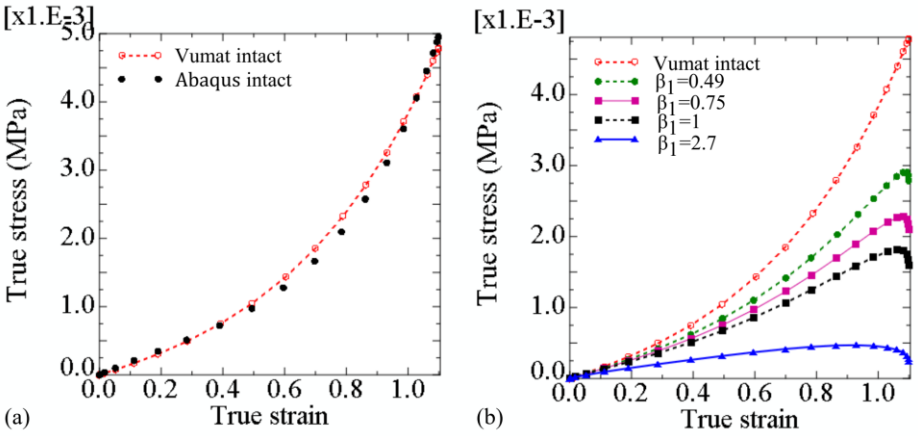


Figure 18: (a) True stress versus true strain in a shell element determined with the Abaqus built-in Mooney Rivlin model and the Vumat damage model for $\beta_1$=0, (b) True stress versus true strain determined with the Vumat erythrocyte membrane damage model showing the stress decrease with initiation and increase of membrane damage.

### 3.3.2 Representing erythrocyte membrane damage in Ogden, Yeoh, Reduced Polynomial models

The erythrocyte membrane stress predicted with the Ogden, Yeoh and Reduced Polynomial model, respectively, agrees well with the developed erythrocyte membrane damage model for the intact and damage states, i.e., $\beta_1 = 0, 0.49, 1, 2.7$ (Figure 19 a to d). The parameter values for the three models, i.e., Ogden, Yeoh, and the Reduced polynomial and the different membrane states, are provided in appendix A, Table A.1 to Table A.12.

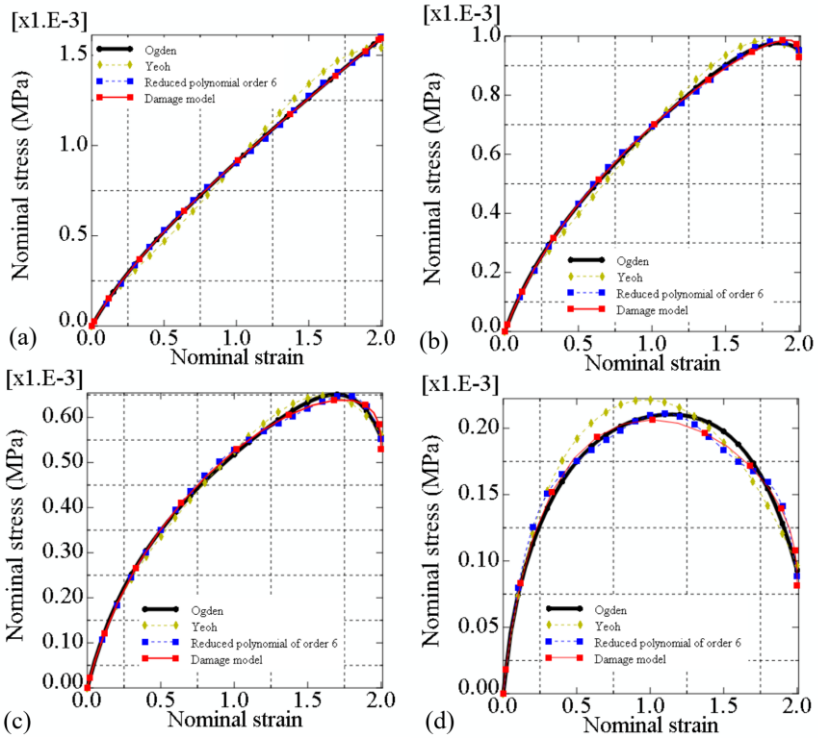


Figure 19: Erythrocyte membrane damage represented by the Ogden, Yeoh, and Reduced polynomial materials models at various damage states in a single shell element, for $\beta_1 = 0$ (a), $\beta_1 = 0.49$ (b), $\beta_1 = 1$ (c), and $\beta_1 = 2.7$ (d).

The Abaqus material evaluation indicated that for the intact erythrocyte membrane ($\beta_1 = 0$), the Ogden model Eqn. (65) is the least stable of the three evaluated models. The Ogden strain energy function is unstable in biaxial tension when the biaxial nominal strain is greater than 1.05. In contrast, the Yeoh strain energy function Eqn. (66), the Reduced Polynomial strain energy function Eqn. (67), and the erythrocyte membrane damage function are stable in biaxial tension for the entire range of the biaxial nominal strain up to 2.0.

For erythrocyte membrane damage (EMD) model with $\beta_1 = 0.49$, the Ogden model is the least stable model, becoming unstable in biaxial tension when the biaxial nominal strain is greater than 1.75. The Yeoh and the Reduced Polynomial strain energy functions become unstable when the biaxial nominal strains exceed 1.96 and 1.98, respectively.

For erythrocyte membrane damage (EMD) model with $\beta_1 = 1$, the Ogden model has the lowest stability threshold with a nominal biaxial strain of 1.74, see Figure 19 (c). the stability threshold of the Yeoh and Reduced Polynomial strain energy functions are strains of 1.8 and 1.85, respectively.

For the most severe erythrocyte membrane damage with $\beta_1 = 2.7$, the erythrocyte membrane damage model has the lowest stability threshold of a nominal strain of 1.19, see Figure 19 (d) and Table 3. The

Reduced Polynomial, Ogden and Yeoh strain energy functions become unstable when the biaxial nominal strain exceeds 1.34, 1.5 and 1.36, respectively. The strain stability thresholds for all the four models when $\beta_1 = 2.7$ are relatively lower than that obtained when $\beta_1$ is equal to 0.49 and 1, showing that all the four material models are poorly stable at a high degree of damage, see Table 3.

Table 3: Strain stability threshold of various material models at various erythrocyte membrane damage state.

| Material model | Stability threshold ($\beta_1 = 0$) | Stability threshold ($\beta_1 = 0.49$) | Stability threshold ($\beta_1 = 1$) | Stability threshold ($\beta_1 = 2.7$) |
|---|---|---|---|---|
| EMD | stable | 1.98 | 1.89 | 1.19 |
| Ogden | 1.05 | 1.75 | 1.74 | 1.5 |
| Yeoh | stable | 1.96 | 1.8 | 1.36 |
| Reduced Polynomial | Stable | 1.98 | 1.85 | 1.34 |

## 3.4 Discussion

The study of the impact of the malaria merozoite-induced erythrocyte membrane damage on the invasiveness of the merozoites to date has been limited due to the lack of constitutive models for the remodelling of the erythrocyte membrane during the entry of the malaria merozoite. Additionally, it is very challenging to experimentally investigate the invasiveness of the malaria merozoite due to damage because the process is rapid and damage occurs at a molecular scale, hence challenging to quantify. With parameterisation of the developed damage model, various degrees of damage relevant to the merozoite induced remodelling of the erythrocyte membrane can be studied.

One of the challenges encountered when using hyperelastic models is that they are not always stable, i.e. when strain is inversely related to stress. One way of assessing the stability of a model is by using Drucker's stability. This condition comes with many challenges since some hyperelastic models can be Drucker unstable for small and large strains when subjected to different loading conditions. Common practice is to use the model with a known stability threshold or validity range. For example, the Mooney Rivlin model has a known validity range of up to 138% equi-biaxial logarithmic strain (Marckmann and Verron 2006).

The stability thresholds of the developed constitutive damage model have been analytically determined by using Drucker's stability criteria and are in range with the stability thresholds of the Yeoh and Reduced Polynomial models. The stability thresholds are used to determine the validity ranges of the hyperelastic models and the impact of the damage. The initiation and increase in damage, i.e. by

altering $\beta_1$ from 0 to 2.7, alter the nominal strain stability threshold of the developed erythrocyte damage model from a stable state to 1.19. The decrease in the maximum stresses when damage is induced (see Figure 18 b and Figure A.1) represents stiffness reduction, indicating that the developed damage model accurately mimics the phosphorylation of the key erythrocyte membrane skeleton. Phosphorylation is a process known to destabilise the erythrocyte membrane and reduce its stiffness.

The Ogden, Yeoh and Reduced Polynomial constitutive models with material parameters indicated from Table A.1 to Table A.12 correspond to the developed damage model's constitutive responses associated with $\beta_1$ ranging from 0 to 2.7. Thus, these models can simulate various degrees of material damage of the erythrocyte membrane if implementing the new erythrocyte membrane model is not feasible.

# 4 A finite element model for the invasion of human erythrocytes by a plasmodium falciparum merozoite

## 4.1 Introduction

The invasion of malaria merozoites into human erythrocytes has been extensively studied as a potential target for antimalarial drugs (Flannery *et al.* 2013). During the invasion of erythrocytes, the merozoite is highly exposed to the host immune system and is highly vulnerable to therapeutic interventions hence an essential target for antimalarial drugs. Despite the enormous interest in studying the invasion process, fundamental gaps in the knowledge of the invasion process remain. To date, the impact of erythrocyte morphology and local erythrocyte membrane damage on the invasiveness of a malaria merozoite has not been explored comprehensively due to the lack of detailed models of the invasion mechanics to complement findings from experimental studies.

Limitations of in vivo approaches for analysing the invasion process have led to an inadequate mechanistic understanding of the invasion process. Unlike in vivo approaches, in silico approaches provide easier alternative methods of ascertaining how biomechanical factors may contribute to the invasiveness of the malaria merozoite. The malaria merozoite entry into an erythrocyte is an active process that involves the application of actomyosin-based forces on the erythrocyte membrane. The forces are transmitted to the erythrocyte membrane through contact with the merozoite surface (Dasgupta *et al.* 2014). To date, a detailed analysis of the mechanistic role of the erythrocyte membrane and associated structure, i.e., the spectrin network involved in the invasion process, is limited to 2D analytical models (Abdalrahman and Franz 2017a). Additionally, current analytical models do not incorporate the remodelling of the erythrocyte membrane. Hence the need to develop realistic 3D invasion models to account for all factors determining the malaria merozoite's invasiveness, i.e., merozoite-induced membrane damage.

Hereditary spherocytosis is caused by genetic alteration of erythrocyte membrane proteins leading to the formation of spherocytes. Previously, it has been documented that cells with hereditary spherocytosis have abnormal protein structure and thus have a low susceptibility to infection by the malaria merozoite (Eber and Lux 2004). Despite this finding, little is known about the higher invasion resistance of these cells. However, from the current study, it has been determined that shape alteration alone of the erythrocyte to spherical shape is also one of the contributing factors to the low susceptibility of infection of spherocytes by malaria merozoites.

This study aims to computationally investigate the erythrocyte mechanics during malaria parasite invasion with emphasis on (i) the factors contributing to the malaria merozoite's invasiveness and (ii) the impact of local disruption of the spectrin network on the global mechanical properties of the erythrocyte for assessing the feasibility of mechanical markers for testing the efficacy of invasion blocking anti-malarial drugs.

## 4.2 Materials and methods

### 4.2.1 Geometric modelling

#### 4.2.1.1 The healthy erythrocyte

A 3D biconcave geometry of the erythrocyte with dimensions shown in Figure 20 was generated in Abaqus by using:

$$z = \pm D_0 \left( 1 - \frac{4\,(x^2 + y^2)}{D_0^2} \right)^{1/2} \left( a_0 + a_1 \frac{x^2 + y^2}{D_0^2} + a_2 \frac{(x^2 + y^2)^2}{D_0^4} \right) \qquad (68)$$

where x, y, z are principal coordinate directions, $D_0$ = 7.82 µm is the undeformed diameter of the erythrocyte cell. $a_0$, $a_1$, $a_2$ are constants with values of 0.0518, 2.026 and -4.491 respectively. The generated erythrocyte model has a volume of 94.47 µm$^3$ and a surface area of 135 µm$^2$ consistent with the literature (Li *et al.* 2014a).

Table 4: Erythrocyte shape parameters.

| Parameters | $D_0$ | $a_0$ | $a_1$ | $a_2$ |
|---|---|---|---|---|
| Value | 7.82 µm | 0.0518 | 2.026 | -4.491 |

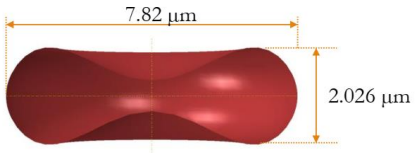


Figure 20: Erythrocyte geometry

#### 4.2.1.2 The spherocyte

In individuals with spherocytosis, erythrocytes take a spherical form due to alterations of erythrocyte membrane proteins and hence the geometry of the spherocyte shown in Figure 21 was generated using the parts module in Abaqus by using:

$$r^2 = (x - k_c)^2 + (y - l_c)^2 + (z - n_c)^2 \quad (69)$$

where r is the radius of the spherocyte, and $k_c$, $l_c$, $n_c$ are centre coordinates of the spherocyte, where $k_c = l_c = n_c = 0$. x, y, z denotes the coordinate points on the surface of the spherocyte. The surface area to volume ratio of the spherical geometry is reduced by 14% compared to the discoid erythrocyte geometry.

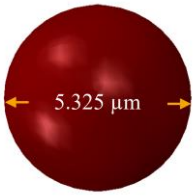


Figure 21: The geometry of the spherocyte generated in Abaqus.

#### 4.2.1.3 The malaria plasmodium falciparum merozoite

The merozoite shape has been previously described from cryo x-ray images of free malaria merozoites shown in Figure 22. From these data, the mean physical dimensions of the malaria merozoite were determined as follows: Physical length $L_m = 1.98 \pm 0.08$ µm, width $W = 1.40 \pm 0.06$ µm, volume $V_{actual} = 1.71 \pm 0.15$ µm$^3$ and surface area $A_{actual} = 8.06 \pm 0.72$ µm$^2$.

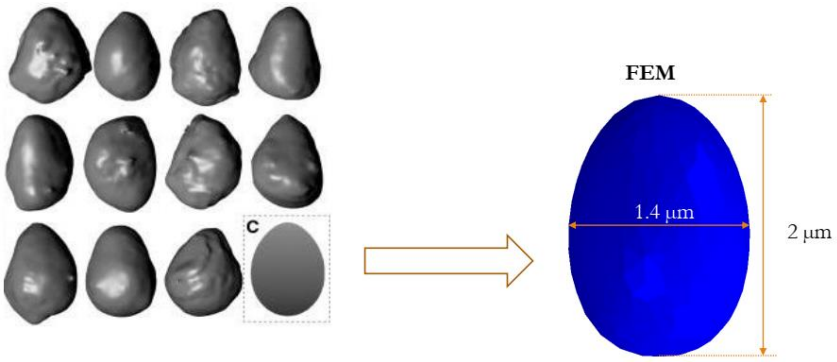


Figure 22: A section of the cryo x-ray image of free Plasmodium Falciparum merozoites. Schematic adapted from Dasgupta *et al.* (2014).

The 3D merozoite geometry shown in Figure 23 was generated based on the previously determined egg shape geometry using:

$$z(\theta) = [2R_a - R_b(1 - \cos\theta)](1 + \cos\theta)/4 \quad (70)$$

$$\rho(\theta) = \sin\theta\,[2R_a - R_b(1 - \cos\theta)]/4 \quad (71)$$

where ρ and z are cartesian coordinates, $R_a = 1$ µm, $R_b = 0.7$ µm are parameters that determine the egg shape profile of the malaria merozoite, and θ is a polar angle which varies from 0 to 180 degrees.

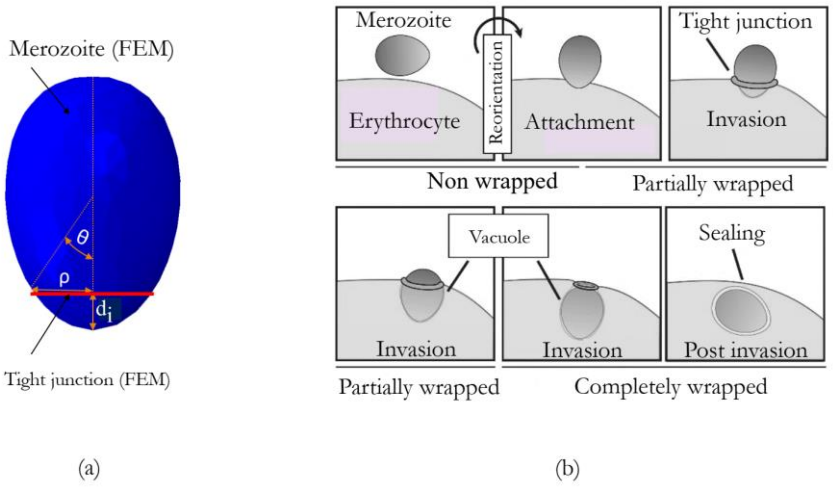


Figure 23: Rigid egg shape geometry of the malaria merozoite generated in Abaqus Explicit.

Images from electron microscopy, cryo-electron tomography, cryo x-ray tomography and widefield deconvolution fluorescence imaging of a merozoite during invasion show negligible changes in malaria merozoite shape throughout the invasion process (Zuccala *et al.* 2016). Hence, this study treated the merozoite geometry as a rigid body.

#### 4.2.1.4 The tight junction between malaria merozoite and erythrocyte membrane

The malaria merozoite pulls itself into the erythrocyte through the tight junction complexes, a structure established by the malaria merozoite after forming the invasion pit. The tight junction was modelled as a deforming mechanical link between the malaria merozoite surface and the erythrocyte membrane, forming an annulus-like structure to facilitate erythrocyte membrane wrapping. The annulus is defined as a circular ring with an internal diameter of 0.76 µm and a cross-section radius of 0.04 µm.

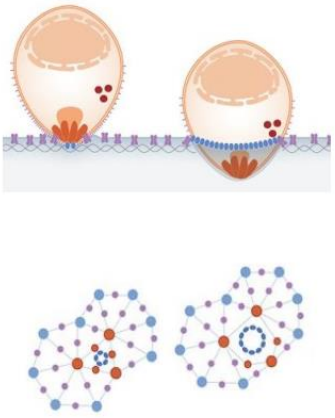

Figure 24:The orange dots represent merozoite ligand-bound complexes, blue dots represents tight junctional complexes. The figure has been adapted from (Koch and Baum 2016).

### 4.2.2 Constitutive modelling

#### 4.2.2.1 Constitutive modelling for erythrocyte membrane

The developed erythrocyte membrane damage model (EMD), see Eqn. (72) was specified using the VUMAT subroutine to induce localised damage in the erythrocyte membrane, while the Mooney Rivlin law model was specified using the material module to describe the constitutive response of the intact erythrocyte membrane.

$$\sigma_{ij}=\frac{e^{-(\beta_1\tau)}}{J}\left[\frac{1}{J^{\frac{2}{3}}}(C_{10}+\bar{I}_1C_{01})B_{ij}-(\bar{I}_1C_{10}+2\bar{I}_2C_{01})\frac{\delta_{ij}}{3}-\frac{1}{J^{\frac{4}{3}}}C_{01}B_{ik}B_{kj}+\frac{KinJ}{J}\delta_{ij}\right] \quad (72)$$

where $C_{10}$, $C_{01}$, $D_1$ are temperature-dependent material parameters, J is the total volume ratio, $\bar{I}_1$ and $\bar{I}_2$ are the first and second deviatoric strain invariant of the left Cauchy-Green deformation tensor B, given by:

$$B = F \cdot F^T \quad (73)$$

where F is the deformation gradient tensor (Gilson and Crabb 2009), and the invariants are defined by:

$$I_1 = \text{trace}\,(B) \quad (74)$$

$$I_2 = \frac{1}{2}\left(I^2 - B{\cdot\cdot}B\right) \quad (75)$$

The relative compressibility of the material also determines the mechanical response of the erythrocyte membrane. The relative compressibility is the ratio of the initial bulk modulus $K_0$ to the initial shear modulus $\mu_0$ of the material:

$$R_c = \frac{K_0}{\mu_0} \tag{76}$$

where $\mu_0$ and $K_0$ are defined by Eqns. (77) and (78), respectively, and large $R_c$ values show that the material is less compressible:

$$\mu_0 = 2\,(C_{10} + C_{01}) \tag{77}$$

$$K_0 = \frac{2}{D_1} \tag{78}$$

The Poisson's ratio **ν** for hyperelastic materials is related to R by:

$$\nu = \frac{3R_c\text{-}2}{6R_c+2} \tag{79}$$

Furthermore, $D_1$ is expressed as:

$$D_1 = \frac{3\,(1 - 2\,\nu)}{2\,(C_{10} + C_{01})\,(1 + \nu)} \tag{80}$$

For this study, the Poisson's ratio of the erythrocyte membrane was set to 0.499 to avoid numerical singularity, and hence $D_1$ was set to 12 $mm^2/N$. The material parameters for the Mooney Rivlin model are computed from the elastic modulus by:

$$C_{10} = \frac{E}{6\,(1 + \beta)} \tag{81}$$

where $C_{10} = \beta\, C_{10}$ (Zhang and Zhang 2011) with β ranging from 0 to 0.5. For an elastic modulus E of 1 kPa and setting $\beta = 0.1$, the corresponding values of $C_{10}$ and $C_{01}$ are 152 Pa and 15.2 Pa, respectively.

#### 4.2.2.2 The mechanical properties of the tight junction

In this study, the tight junction was represented with an annulus structure, mimicking the function of the tight junction during the invasion process. The energy associated with the work done by the tight junction is not yet known. However, an estimate of the minimum energy contribution of the tight junction required for a successful invasion was determined with the developed FE model, and the

Mooney Rivlin law was used to define the mechanical response of the annulus structure. The material parameters were determined by minimising the objective function defined by:

$$F_m(Cj) = \psi_m(C_j) \times D_m(C_j) \quad (82)$$

where $\psi_m$ is the strain, energy density function for the annulus structure, and $D_m$ is the diameter of the tight junction at maximum indentation depth at the end of the invasion when the simulation step time is 1.1 s. The binary search algorithm below was used to search for material parameters that minimise the objective function in Eqn. (82).

Given an array $C_j$ of n elements $C_{0j}$, $C_{1j}$, $C_{2j}$ …. $C_{nj-1}$ such that $C_{0j} \leq C_{1j} \leq C_{2j} \leq \ldots\ldots \leq C_{nj-1,}$ the following pseudo-code uses the binary to find the value of the material parameter in $C_j$ that minimises the objective function.

1. Set $L_j = 0$ and $R_j = n_j - 1$
2. If $L_j > R_j$, the search terminates as unsuccessful
3. Determine the middle element index $m_j$ = floor ( $[L_j + R_j]/2$ )
4. Compute the $D_m$ using the middle element parameter in $C_j$.
5. If $D_m > M_d + \bar{e}$ update $C_j$ such that $C_j \geq C_m$, compute $F_m$ and go to step 2.
6. If $D_m < M_d + \bar{e}$, update $C_j$ such that $C_j \leq C_m$, compute $F_m$ and go to step 2.
7. If $D_m \approx M_d$ the search is done, and compute $F_{min}$ = min ($F_m$)

Here, $M_d$ is the width of the merozoite at maximum indentation depth, and $\bar{e}$ is the clearance between the tight junction and the merozoite at the maximum indentation depth. When $F_m = F_{min}$ = min ($F_m$), see Figure 25, and $C_j$ gives a minimum strain energy $\psi_m(C_j)$ such that $D_m \approx M_d$, see Figure 26. The annulus structure's strain energy $\psi_m$ ($C_j$) increases from point a to b, and c, see Figure 25 while the diameter $D_m$ decreases from point a to b but remains constant from point b to c (see Figure 25 and Figure 26).

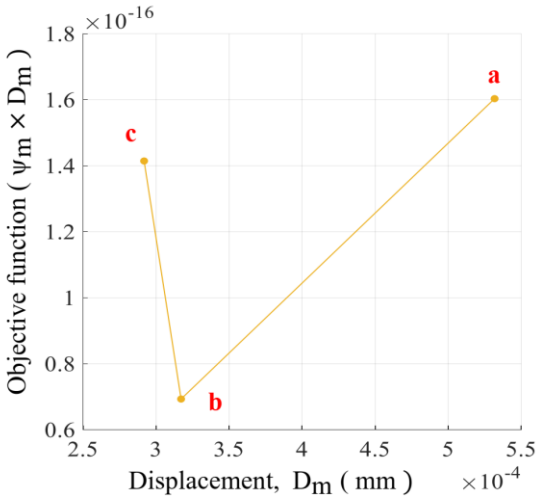


Figure 25: Illustration of the minimisation process of the objective function.

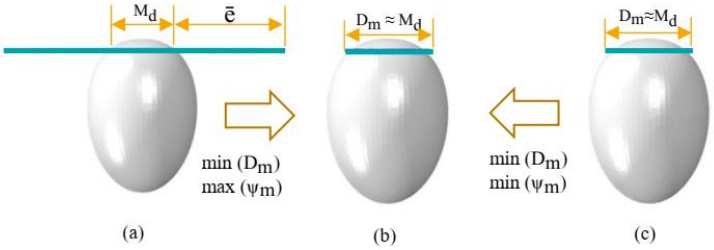


Figure 26: Schematic illustration of how the Mooney Rivlin parameters were determined.

The annulus structure's mechanical properties mimicking the tight junction's role were determined by minimising the objective function (see Table 5). The determined mechanical properties represent the minimum energy required by the annulus structure to ensure erythrocyte membrane wrapping.

Table 5: Mooney Rivlin parameter values of the tight junction complexes.

| **Properties** | **$C_{10}$** | **$C_{01}$** | **$D_1$** |
|---|---|---|---|
| Parameter values | 0.04 MPa | 0.004 MPa | 0.3 $mm^2/N$ |

#### 4.2.2.3 Representing the erythrocyte cytoplasm using smoothed particle hydrodynamics

The smoothed particle hydrodynamics (SPH) method was used to model the erythrocyte cytoplasm deformation. Smoothed particle hydrodynamics is a fully Lagrangian meshfree modelling scheme permitting the discretization of a prescribed set of continuum equations by interpolating the properties directly at a discrete set of points distributed over the solution domain. This approach was first developed to solve PDE problems in astrophysics (Gingold and Monaghan 1977). In Abaqus, the SPH scheme discretises the continuum partial differential equations (Violeau and Rogers 2016). SPH uses

an evolving interpolation scheme to approximate a field variable at any point in a domain. Using the particle approximation or field function Eqn. (83) and its derivative Eqn. (84), the Navier Stokes equation is discretized and solved using the explicit time integration method.

$$f_i = \sum_{j=1}^{N} \frac{m_j}{\rho_j} f_j \, w\left( \left| r_i - r_j \right|, h \right) = \sum_{j=1}^{N} \frac{m_j}{\rho_j} f_j \, w_{ij} \tag{83}$$

$$\nabla \cdot f_i = \sum_{j=1}^{N} \frac{m_j}{\rho_j} f_j \cdot \nabla w\left( \left| r_i - r_j \right|, h \right) = \sum_{j=1}^{N} \frac{m_j}{\rho_j} f_j \cdot \nabla w_{ij} \tag{84}$$

where N is the total number of particles and h is the smoothing length, $r_i$ and $r_j$ are the position vector of the particle of interest and the particle's position vector in the neighbouring region. The field function f and its derivative are constructed using a smoothing or kernel function w shown in Figure 27. Thus, the value of a variable at a particle of interest can be approximated by summing the contributions from a set of neighbouring particles, denoted by subscript j, for which the “kernel” function, w, is shown in Figure 27, is not zero.

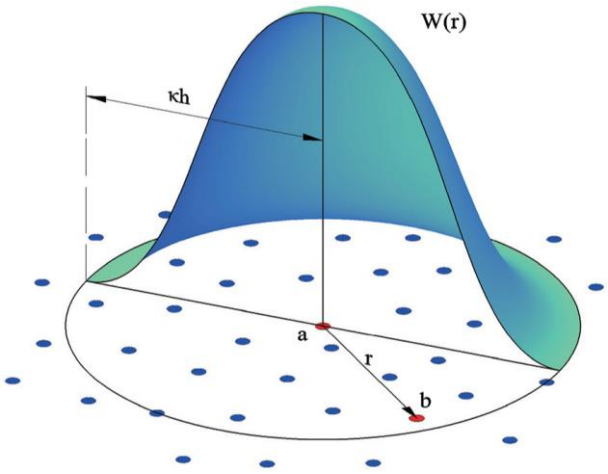


Figure 27: Graphical representation of Kernel function, with permission from Wang *et al.* (2016).

In Abaqus, the erythrocyte cytoplasmic domain is converted to SPH particles by activating a built-in conversion to SPH particles functionality in the mesh module. The erythrocyte cytoplasm primarily comprises viscous haemoglobin, mathematically described by the Navier-Stokes equation in the Lagrangian form (Ye *et al.* 2016). The erythrocyte cytoplasm is generally considered an incompressible Newtonian liquid, and thus, its dynamics are predicted by using the Navier Stokes equations given by:

$$\nabla \cdot v = 0 \tag{85}$$

$$\frac{dv}{dt} = \frac{1}{\rho} ( - \nabla p + \mu \nabla^2 v ) + f_{ext} \tag{86}$$

where p, v, ρ, μ and $f_{ext}$ represent the pressure, velocity, density, dynamic viscosity and external force vector, respectively. SPH solves the Navier Stokes equations by discretizing the whole computational domain into a set of particles. The Mie-Grüneisen equation of state defined in Eqn. (87) was used to model incompressible viscous laminar flow governed by the Navier-Stokes equation of motion. The volumetric response is governed by the equations of state, where the bulk modulus acts as a penalty parameter for the incompressible constraint. Since the viscosity of the erythrocyte cytoplasm is small, a small amount of shear resistance was specified in the materials module to suppress shear modes that can otherwise tangle the mesh. Here the shear stiffness or shear viscosity was used as a penalty parameter. The default hourglass control was used because when the shear model is defined, the hourglass control forces are calculated based on the shear resistance of the erythrocyte cytoplasm, which provides very low shear strength, insufficient to prevent spurious hourglass modes. For the erythrocyte cytoplasmic domain, an equation of state is necessary to link pressure P and density ρ. The Mie-Grüneisen equation of state used for this purpose (Monaghan 1988) is given as follows:

$$p = \frac{\rho_0 c^2 \eta_m}{(1-\eta_m s)^2} \left(1 - \frac{\eta_m \Gamma_0}{2}\right) + \rho_0 \Gamma_0 E_m \tag{87}$$

where $\rho_0$ is the reference density and c is the speed of sound, $\Gamma_0 = 0$ is a material parameter, $\eta_m = 1 - \rho_0/\rho$ is the nominal volumetric compressive strain, $E_m$ is internal energy per unit mass. The background pressure $P_0$ is added to avoid negative pressure values. The density is estimated from the particle distribution utilizing the SPH interpolation. c and s define the linear relationship between the shock velocity, $U_s$, and the particle velocity, $U_p$, as follows:

$$U_s = c + sU_p \tag{88}$$

where s was set to zero such that $U_s = c = 1000$ mm/s.

### 4.2.3 Finite element types and meshes

The FE model comprised multiple components with various element lengths, i.e., the erythrocyte membrane, the tight junction, the rigid merozoite, and the cytoplasm, see Figure 28.

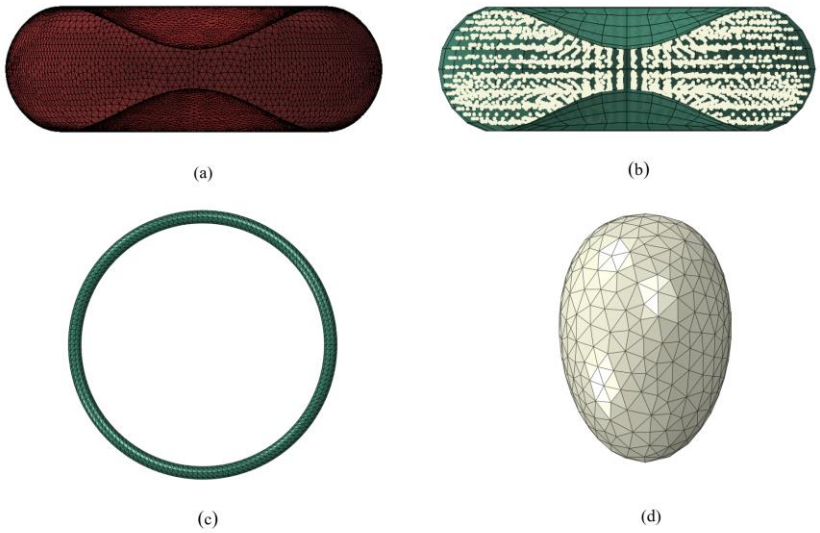


Figure 28: The erythrocyte membrane meshed with triangular shell elements (a), erythrocyte cytoplasm meshed using the 8-node linear brick elements with reduced integration and hourglass control (C3D8R) (b), annulus structure of the tight junction meshed using a ten-node modified quadratic tetrahedron elements (C3D10M) (c), the rigid merozoite meshed using a three-node 3D rigid triangular elements (R3D3) (d).

The tight junction contains the smallest element length relative to the erythrocyte membrane and is generally used to determine stable time increment for the whole model. However, it was necessary to evaluate the stability of the solution due to the mesh density of the erythrocyte membrane. A mesh density study for the erythrocyte membrane was performed to determine the mesh density, which gives a stable solution. In Abaqus, the erythrocyte membrane was modelled using shell elements with a thickness of 0.01 µm (Hochmuth *et al.* 1973). SPH was applied on the erythrocyte cytoplasmic domain; hence, no mesh density study was performed on the cytoplasm. However, to ensure accurate simulation of the cytoplasm by using the SPH functionality, Abaqus requires more than 10000 particles to be generated. Hence 18000 particles were generated by using the particle conversion functionality.

Three-node triangular shell elements with reduced time integration (S3R) were used to mesh the erythrocyte membrane. The reduced time integration algorithm provided more accurate results and reduced the running time. The use of conventional shell elements was preferred because, unlike continuum shell elements which only have displacement degrees of freedom, conventional shell elements have both displacement and rotational degrees of freedom. For the erythrocyte membrane to wrap around the malaria merozoite effectively, each erythrocyte membrane node must have both

displacement and rotation degrees of freedom. Erythrocytes undergo extreme deformations as they circulate through narrow capillaries in the human body. As such, to accurately predict erythrocyte deformation, both displacement and rotational degrees of freedom must be allowed in each element.

Additionally, shell elements were preferred over 3D solid elements for the erythrocyte membrane because shell elements allow the modelling of thin features with fewer elements, thus reducing computational time. Shell elements are also easier to mesh and less prone to negative Jacobian errors, representing negative element volume or distorted elements that might occur when using extremely thin solid features. The erythrocyte cytoplasm was meshed using the 8-node linear brick elements with reduced integration and hourglass control (C3D8R). The mesh provides the initial spatial particle discretisation required for the SPH scheme. Three-node 3D rigid triangular elements (R3D3) were used to mesh the rigid merozoite, while the ten-node modified quadratic tetrahedron elements (C3D10M) were used to mesh the annulus structure of the tight junction. The details of the mesh sizes are indicated in Table 6 below.

Table 6: Element type and mesh sizes for various structures involved in the invasion mechanism.

| **Structure** | **Element type** | **Elements** |
|---|---|---|
| Membrane | S3R | 19942 |
| Cytoplasm | C3D8R | 841 |
| Merozoite | R3D3 | 700 |
| Tight junction | C3D10M | 5535 |

### 4.2.4 Boundary conditions and interactions of merozoite and erythrocyte

#### 4.2.4.1 Boundary conditions

Several assumptions and boundary conditions were considered and are listed below:

- The erythrocyte was assumed suspended in a Euclidean space with an initial velocity of each node of approximately zero. The load module was used to predefine the initial velocity fields at each node in the erythrocyte membrane, see Figure 29 b.
- A constant external pressure load of 16 kPa equal to systolic blood pressure was applied on the external surface of the erythrocyte membrane, see Figure 29 a.
- The malaria merozoite is displaced by 2 μm along its longitudinal axis of the merozoite. The displacement is applied using a ramp function from 0.1 s to 1.1 s, see Figure 29 d.

- Each node of the tight junction freely deforms in the x and z directions, see Figure 29 c.

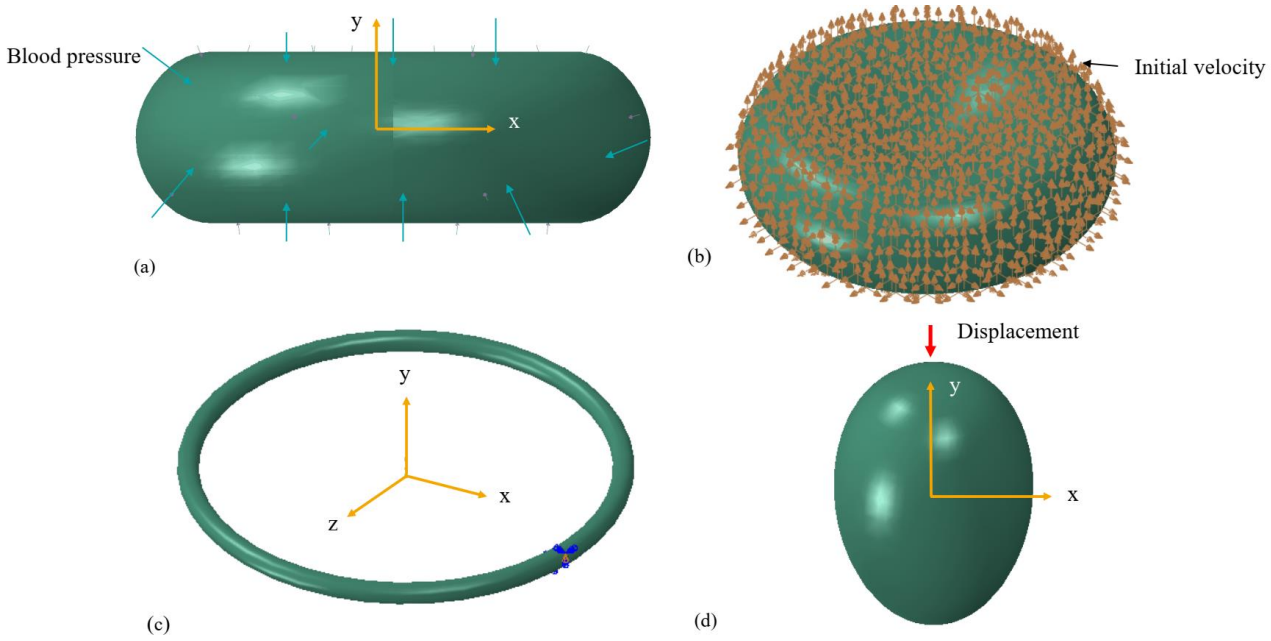


Figure 29: Blood pressure applied on the outer surface of the erythrocyte membrane (a), the initial velocity of $2\times10^{-30}$ mm/s applied at each node of the erythrocyte membrane (b), each node of the annulus structure is only allowed to displace in z and x directions (c), the rigid malaria merozoite is displaced in the negative y-direction (d).

### 4.2.4.2 Erythrocyte and malaria merozoite interactions

The interaction module in Abaqus Explicit was used to define the mechanical interaction of the interfaces of structures involved in the invasion process, as illustrated in Figure 30.

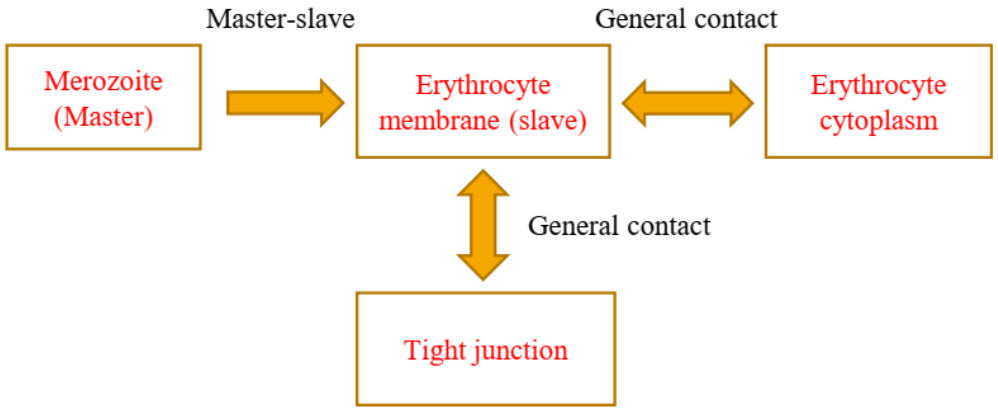


Figure 30: Structural interactions of the erythrocyte membrane, tight junction, malaria merozoite and the erythrocyte cytoplasm.

Two algorithms for modelling contact interactions were used. The general contact algorithm allows very simple definitions of contact with very few restrictions on the types of surfaces involved. The

contact pair algorithm has more restrictions on the surfaces involved and often requires a more careful contact definition. However, it allows interaction definitions unavailable with the general contact algorithm. The general contact algorithm was used to define contact interactions between the erythrocyte membrane, the erythrocyte cytoplasm and the tight junction. The contact pair algorithm was used to define contact between the malaria merozoite and the outer surface of the erythrocyte membrane. The contact pair algorithm in Abaqus Explicit includes the contact surface weighting (balanced or pure master-slave) and the sliding formulation (finite, small, or infinitesimal). The contact pair algorithm with pure master-slave weighting was used for the contact between the malaria merozoite surface and the region of entry **(**ROE**)** on the erythrocyte membrane. The interacting surfaces can penetrate each other for the pure master-slave scheme, leading to numerical instabilities. To avoid numerical errors due to penetration, the mesh density of the slave surface must be greater than that of the master surface. A mesh density study for the two surfaces was conducted to determine the mesh sizes for both the master and slave surfaces.

### 4.2.5 Model validation

#### 4.2.5.1 Erythrocyte model validation and simulation of a healthy erythrocyte in an optical tweezer/trap

This section presents a detailed validation method of the developed erythrocyte model based on laser trap experimental data (Mills *et al.* 2004). The mechanical response of the erythrocyte predicted by the developed model is compared against previous experimental data (Figure 31 c) from an optical trap experiment, see Figure 31 (a) and (b), where a 193 pN force is applied to stretch the erythrocyte.

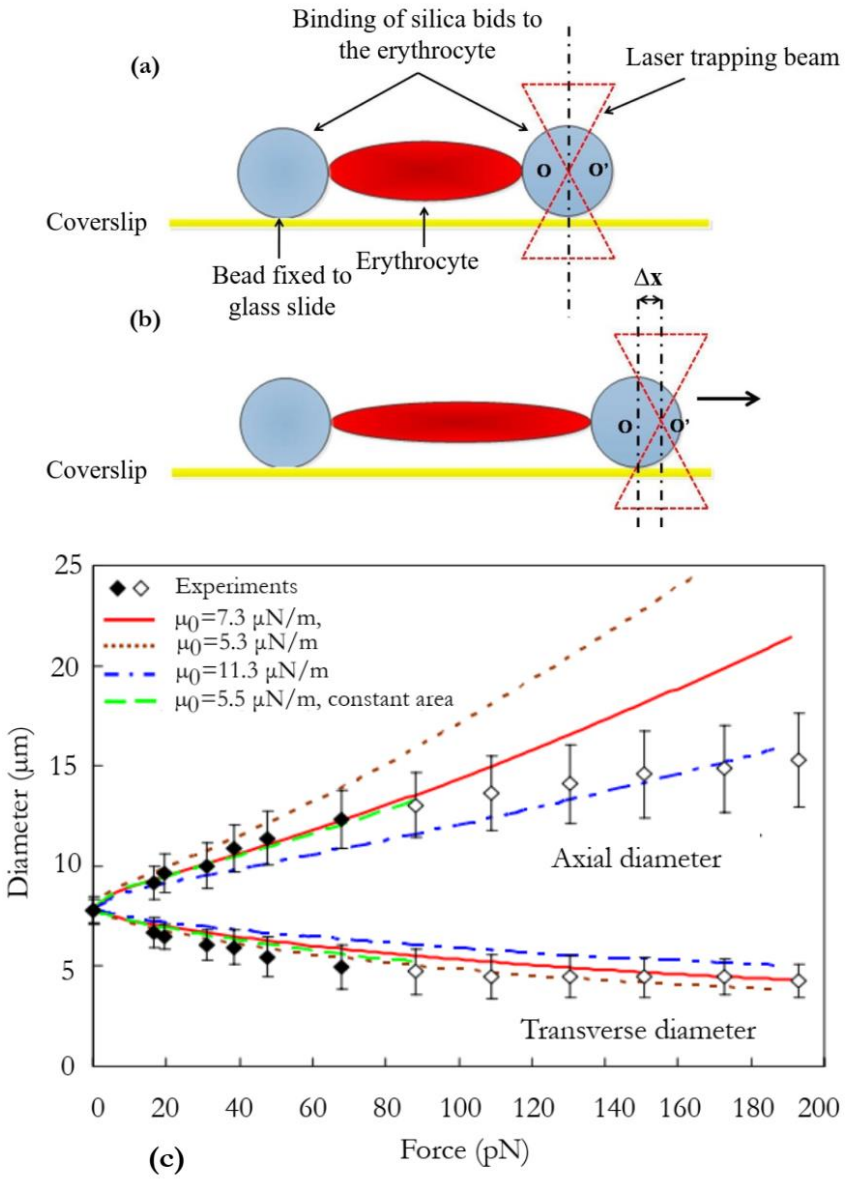


Figure 31: Optical tweezer experiment set up (a and b) (Song *et al.* 2017), Optical tweezer experimental data and numerically generated data (Mills *et al.* 2004) (c).

In the optical trap experiment, a stretching force is applied to one of the two silica beads attached to the erythrocyte. One microbead is fixed to the glass slide while the other microbead is trapped using a laser beam (Song *et al.* 2017). Cell stretching is performed by moving the trapped microbead. The deformation is determined by images of unstretched and stretched erythrocytes. Similarly, with optical trap simulation, the erythrocyte model was deformed in the axial and transverse directions when the resultant force F = 200 pN was applied on one microbead.

#### 4.2.5.2 Validation and simulation of merozoite invasion model

Recently, Geoghegan *et al.* (2021) used a high spatiotemporal resolution lattice light-sheet microscopy (LLSM) to analyse the malaria merozoite invasion into the erythrocyte by segmenting and tracking the formation of parasitophorous vacuole membrane (PVM). With this technique, the authors determined the portion of the erythrocyte membrane surface area that wraps malaria merozoite and the surface area of the erythrocyte membrane that does not wrap the malaria merozoite. The study documents the decrease in the erythrocyte membrane surface area since a portion of the area wraps the malaria merozoite (see Figure 32). The data obtained from this study was then used to validate the developed invasion model.

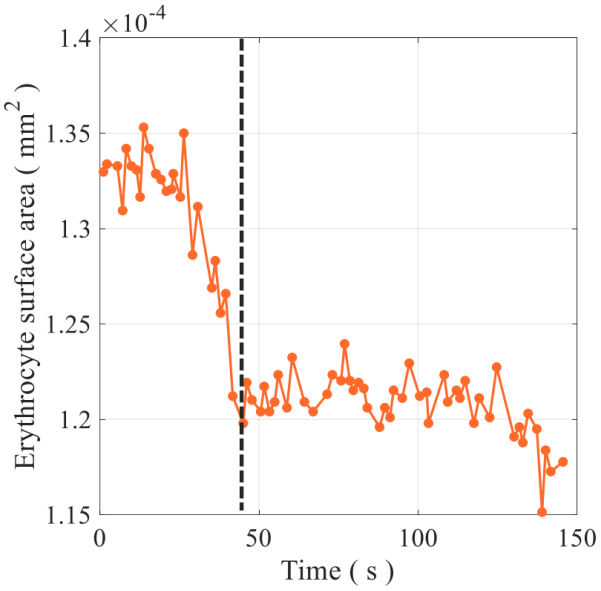


Figure 32: Reduction of the erythrocyte surface area during the erythrocyte invasion; the dashed line (black) represents the time when malaria merozoite is entirely wrapped by the erythrocyte membrane (Geoghegan *et al.* 2021).

In a human being, erythrocytes are subjected to physiological blood pressure. Hence to obtain realistic simulation results of the invasion model, a surface blood pressure must be applied to the surface erythrocyte model. However, no physiological pressure was applied in the Geoghegan *et al.* (2021) experiment. As such, surface area data of the erythrocyte obtained from the invasion model where no surface pressure was applied was compared with erythrocyte areal data from the Geoghegan *et al.* (2021) experiment to validate the invasion model.

### 4.2.6 Finite element analysis and case studies

#### 4.2.6.1 Generalised explicit finite element analysis in Abaqus

A generalised Abaqus Explicit dynamic analysis procedure was used to simulate the deformation of an erythrocyte during the invasion by a malaria merozoite. This procedure involves numerically solving the momentum equilibrium Eqn. (89) using an explicit central difference time integration rule described by Eqns. (90) and (91). The momentum equilibrium is:

$$M^{NJ}\,\ddot{u}_i^N = P_i^J - I_i^J \tag{89}$$

where $M^{NJ}$ is the mass matrix, $P^J$ is the applied load vector, $I^J$ is the internal force vector, $u^N$ denotes spatial degrees of freedom, and i is the increment number in the explicit dynamic step. $M^{NJ}$ is diagonalized to form a lumped mass matrix to reduce the computational complexity of the central difference time integration algorithm (Systemes 2015).

$$\dot{u}_{i+1/2}^N = \dot{u}_{i-1/2}^N + \frac{\Delta t_{i+1} + \Delta t_i}{2}\,\ddot{u}_i^N \tag{90}$$

$$u_{i+1}^N = u_i^N + \Delta t_{i+1}\,\dot{u}_{i+1/2}^N \tag{91}$$

The dynamic explicit analysis was specified using the step module where mass scaling and geometrically nonlinear analysis were specified. Mass scaling was only applied to the erythrocyte membrane and the tight junction with the primary purpose of obtaining a quasi-static response. The quasi-static analysis was achieved by simulating the invasion process in the shortest time, i.e. for a period of 1.1 s, while keeping the inertial forces relatively low. The semi-automatic mass scaling was used throughout the step to scale mass elements periodically and effectively reduce the wave speed. The effectiveness of the mass scaling algorithm in ensuring a quasi-static solution was determined by ensuring that the total kinetic energy of the erythrocyte model is much smaller than the internal or strain energy of the erythrocyte model. The kinetic energy represents the inertia effects on the global response of the erythrocyte model, while the internal energy represents the static effects. Time incrementation was achieved automatically by using built-in functionality. The adaptive, global estimation algorithm was applied to determine the maximum frequency of the entire model using the current dilatational wave speed.

#### 4.2.6.2 Case Study 1: Impact of the erythrocyte morphology on the merozoite invasiveness

With the developed FE model, the impact of erythrocyte morphology and malaria merozoite induced damage on the invasiveness of the malaria merozoite was assessed. The invasiveness of the malaria merozoite in the convex region (see Figure 33 a) and the concave region (see Figure 33 b) was assessed by comparing the total invasion energies associated with the malaria merozoite's invasion of the convex and concave regions.

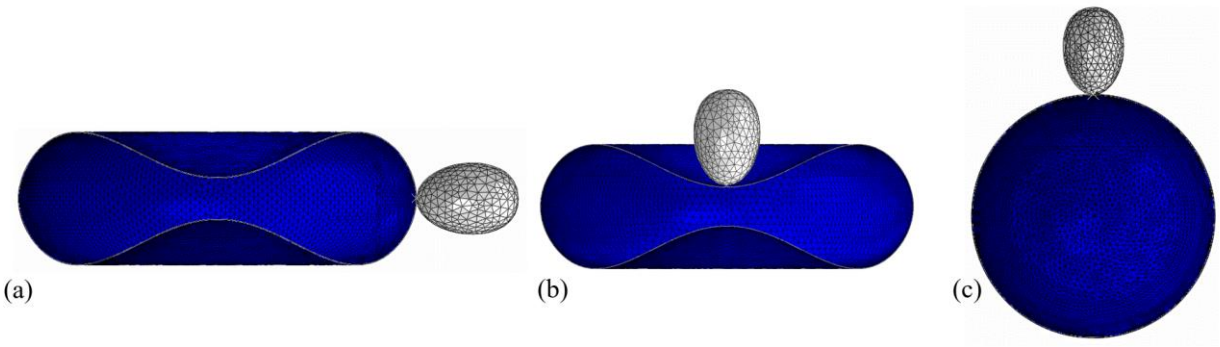


Figure 33: Entry point of the merozoite (grey) into a human erythrocyte (blue) through a convex region (a), the entry point of the merozoite (grey) into a human erythrocyte (blue) through a concave region (b), the entry point of a malaria merozoite (grey) into a human spherocyte (blue) (c).

To assess the impact of sphericity, i.e., surface area to volume ratio, the total invasion energies of two simulations are compared: One involving the entry of the malaria merozoite into a normal discoid shaped erythrocyte (see Figure 33 a and b), and the other involving entry simulation of a malaria merozoite into a spherical erythrocyte with the same volume as the normal erythrocyte (see Figure 33 c). To date, it is not known whether the spherical shape impacts the invasiveness of the malaria merozoite. The morphometric parameters used to define the two erythrocyte morphologies, i.e., discoid and spherical morphologies, are given in Table 7. The developed spherical model of the erythrocyte represents a 27% reduction of a healthy erythrocyte's S/V ratio and total surface area. With the two models of the erythrocyte, i.e., spherical and discoid models, the impact of morphological variations on the invasiveness of the malaria parasite was investigated.

Table 7: Simulation parameters used in Abaqus.

| Erythrocyte shape | Surface area (S) | Volume (V) | S/V |
|---|---|---|---|
| Discoid | 135 $\mu m^2$ | 94 $\mu m^3$ | 1.44/m |
| Spherical | 98.47 $\mu m^2$ | 94 $\mu m^3$ | 1.05/m |

#### 4.2.6.3 Case Study 2: Impact of phosphorylation induced damage in the erythrocyte membrane on the merozoite invasiveness

Two stages of erythrocyte membrane damage were investigated using the damage model described in chapter 3. This study was done to assess the impact of the damage stages on the invasiveness of the malaria merozoite. The first stage of damage was induced during the early invasion, i.e., from 0 to 0.1s, accounting for 9 % of the entire invasion period. The second stage of damage involved damage induced throughout the entire invasion process. Erythrocyte membrane damage was induced in the red region, with a diameter of 1.028 µm, see Figure 34. For each damage stage, the invasiveness of the malaria merozoite was determined by evaluating the indentation forces induced by the malaria merozoite. The damage parameters used to evaluate the indentation forces are given below (see Table 8).

Table 8: Damage parameters for first (0 – 0.1 s) and second stage damage (0–1.1 s).

| | | |
|---|---|---|
| Damage parameters for the entire invasion process (0 – 1.1 s) | 0.49 | 1 |
| Damage parameters for the early stage damage (0 – 0.1 s) | 5.4 | 11 |

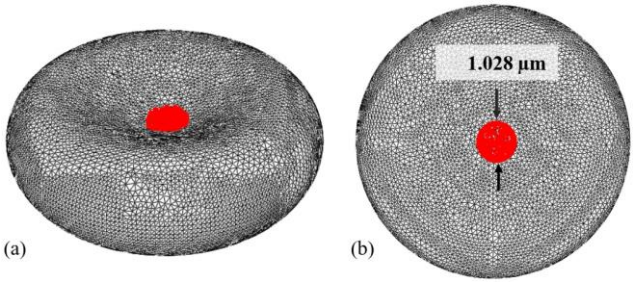


Figure 34: Region in red where two types of damage are induced, start configuration of the erythrocyte, isometric view (a), plan view (b).

#### 4.2.6.4 Case Study 3: Erythrocyte compression

The compression simulation involving an intact erythrocyte model and an erythrocyte with a locally damaged membrane aimed to investigate the impact of local erythrocyte membrane damage on the global mechanical and structural properties of the erythrocyte, see Figure 35 a.

First, an intact erythrocyte model was compressed to extract the compression data. Secondly, an erythrocyte with a locally damaged erythrocyte membrane was compressed to extract two compression data sets, one obtained by inducing damage in the concave region, i.e., damage location 1 and the other

in the convex region of the erythrocyte membrane, i.e., damage location 2, see Figure 35 b. The diameter of the region where damage was induced was set to 1.028 µm.

The compression plate (10 × 10 µm) was displaced by 1.3 µm for a period of 1.1 s, while the support plate (10 × 10 µm) was fixed to facilitate compression of the erythrocyte. The compression and the support plates were modelled using 5,000 linear triangular rigid shell elements (R3D3). The contact pair algorithm was used to define contact between the compression plate-erythrocyte interface and the erythrocyte-support plate interface, where surface-to-surface contact formulation with kinematic contact method was defined. Both the normal and the tangential behaviour of the interfaces mentioned above were defined for this type of interaction. Isotropic tangential interaction with negligible friction coefficient was used to define the tangential behaviour between the interfaces. Hard contact formulation, which allows separation of the interfaces mentioned above, was used to define the normal behaviour of the interfaces.

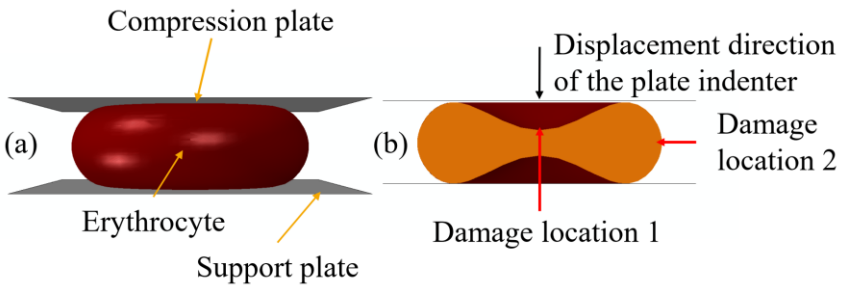


Figure 35: Initial configuration of the compression test simulation (a), concave and convex regions of the erythrocyte are indicated by damage locations 1 and 2, respectively.

The force-compression data obtained from indenting a locally damaged and intact erythrocyte were compared to assess the sensitivity of the global indentation for local erythrocyte membrane damage. A sufficient sensitivity may indicate the potential of compression tests for further development and implementation to study the malaria merozoite-induced damage in a physical experiment. The impact of surface pressure on the mechanical response of the locally damaged erythrocyte membrane was also investigated.

#### 4.2.6.5 Case Study 4: Erythrocyte nanoindentation

The nanoindentation test simulation was conducted by utilising a similar approach used in the compression test simulation from the previous section. The nanoindentation simulation involved an intact erythrocyte and an erythrocyte with a locally damaged membrane to investigate the impact of local erythrocyte membrane damage.

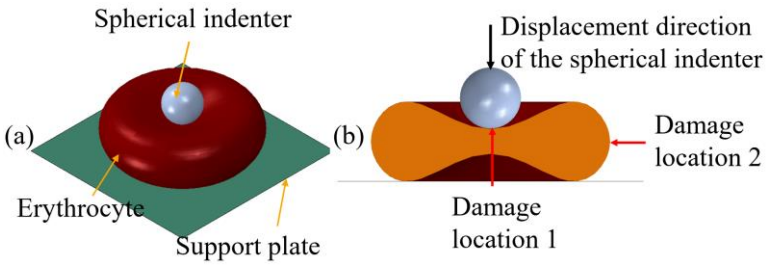


Figure 36: a) Initial configuration of the nanoindentation simulation, b) concave and convex regions of the erythrocyte are indicated by damage locations 1 and 2, respectively.

The spherical indenter with a diameter of 2 µm, representing 25.6% of erythrocyte diameter, was displaced by 1.31 µm, representing 64.7% of the maximum erythrocyte thickness. The support plate (10×10 µm) was fixed to facilitate indentation of the erythrocyte. The spherical indenter was modelled by using 854 linear rigid triangular shell elements (R3D3), while the support plate was modelled by using 5000 linear rigid triangular shell elements (R3D3). The contact pair algorithm was used to define contact between the spherical indenter-erythrocyte interface and the erythrocyte-support plate interface, where the surface-to-surface contact formulation with kinematic contact method was defined. Both normal and tangential behaviour of the interfaces mentioned above were defined for this type of interaction. Isotropic tangential interaction with negligible friction coefficient was used to define the tangential behaviour between the interfaces. Hard contact formulation that allows separation of the interfaces mentioned above was used to define the interfaces' normal behaviour. The force-indentation data obtained from the locally damaged and intact erythrocyte were compared to assess the sensitivity of the nanoindentation to local erythrocyte membrane damage. A sizeable difference between the force-indentation curves of the intact and damaged erythrocyte suggests that the nano-indentation test is sensitive to erythrocyte membrane damage.

## 4.3 Results

### 4.3.1 Validation of the erythrocyte finite element model

The developed erythrocyte model was validated by comparing optical tweezer experimental data (Mills *et al.* 2004) with the numerical data obtained by simulating an optical tweezer experiment. When a force of 200 pN is applied diametrically, the dimension of the erythrocyte FE model increases in the direction of the applied load (see Figure 37) and decreases in the direction normal to the applied force.

The dimension of the erythrocyte FE model that increases in the applied load direction is called the axial dimension. In contrast, the dimension of the erythrocyte FE model that decreases in the direction normal to the applied force is referred to as the transverse dimension.

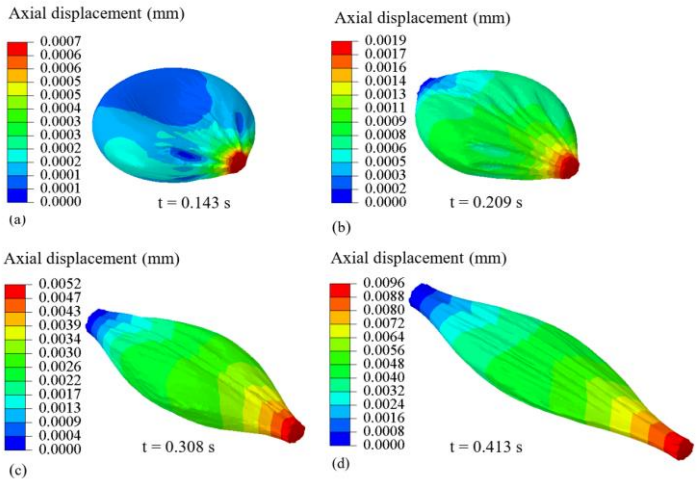


Figure 37: The contour plot of the erythrocyte axial displacements at various stages of optical tweezer simulation test, axial displacement of the erythrocyte FE at 0.0143 s (a), 0.209 s (b), 0.308 s (c), and at 0.413 s (d).

The increase in displacement of the erythrocyte FE model in the axial direction leads to the increase in the axial diameter of the erythrocyte (see Figure 37). In contrast, the increase in the transverse displacements of the erythrocyte FE model leads to the reduction of the transverse diameter of the erythrocyte (see Figure 38).

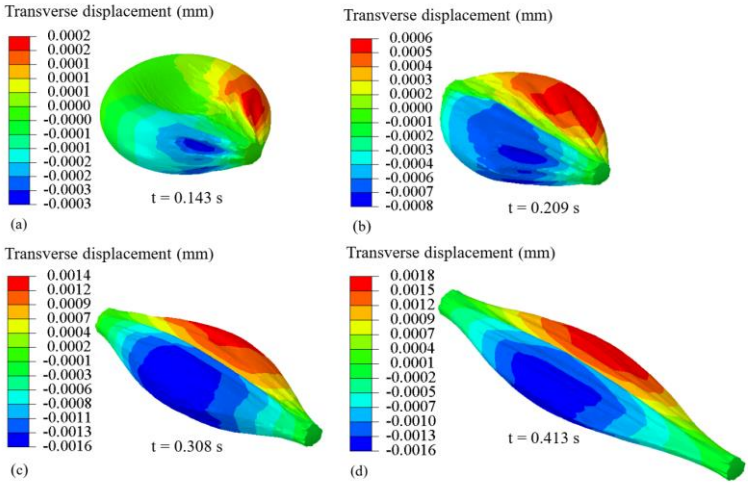


Figure 38: The contour plot of the erythrocyte transverse displacements at various stages of optical tweezer simulation test, transverse displacement of the erythrocyte FE at 0.0143 s (a), 0.209 s (b), 0.308 s (c), and at 0.413 s (d).

The numerical data shows that the transverse diameter of the erythrocyte model fit well with experimental data. However, the axial diameter of the erythrocyte model only fits well with experimental data when it is less than 0.0096 mm (see Figure 39 and Figure 40 a).

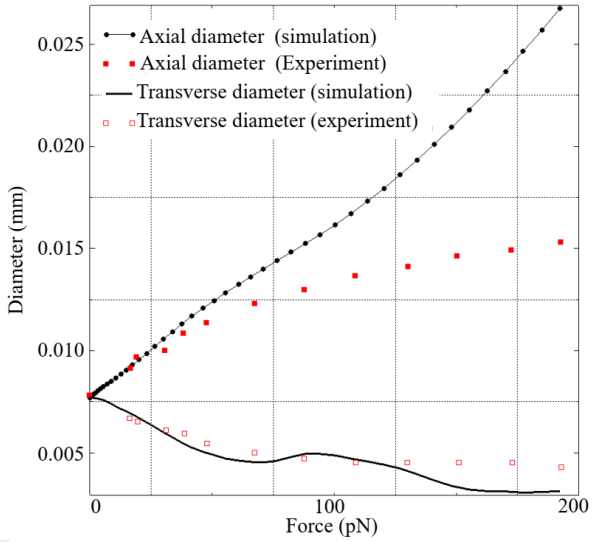


Figure 39: Optical tweezer simulation data (axial and transverse erythrocyte FE model diameters) fitted with optical tweezer experimental data (axial and transverse diameters of the human erythrocyte) (Mills *et al.* 2004).

For the erythrocyte model, the axial diameter of 0.0096 mm, corresponds to the maximum principal erythrocyte membrane logarithmic strain of 1.81 (see Figure 40 b). Beyond this point, the model fits experimental data in the axial direction with limited accuracy. The maximum principal erythrocyte membrane logarithmic strain due to entry of the malaria merozoite into the erythrocyte is 1.77 (see Figure 40 c), which is less than the accuracy threshold of 1.81 maximum principal logarithmic strain.

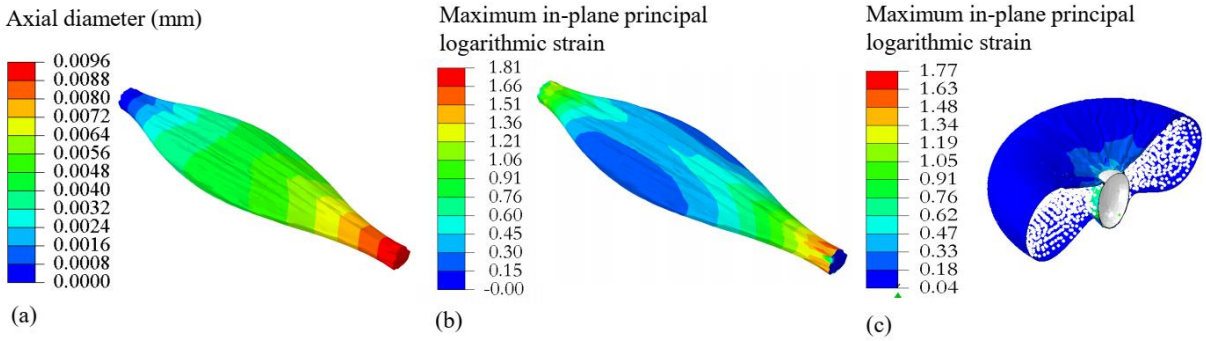


Figure 40: Contour plots of the erythrocyte FE model deformed in an optical tweezer simulation test showing the erythrocyte model axial diameter (a) and maximum principal logarithmic strain (b). The contour plot of the maximum principal logarithmic strain of the erythrocyte membrane (c)

The maximum principal logarithmic strain of the erythrocyte membrane increases throughout the deformation history during the optical tweezer simulation test (see Figure 41).

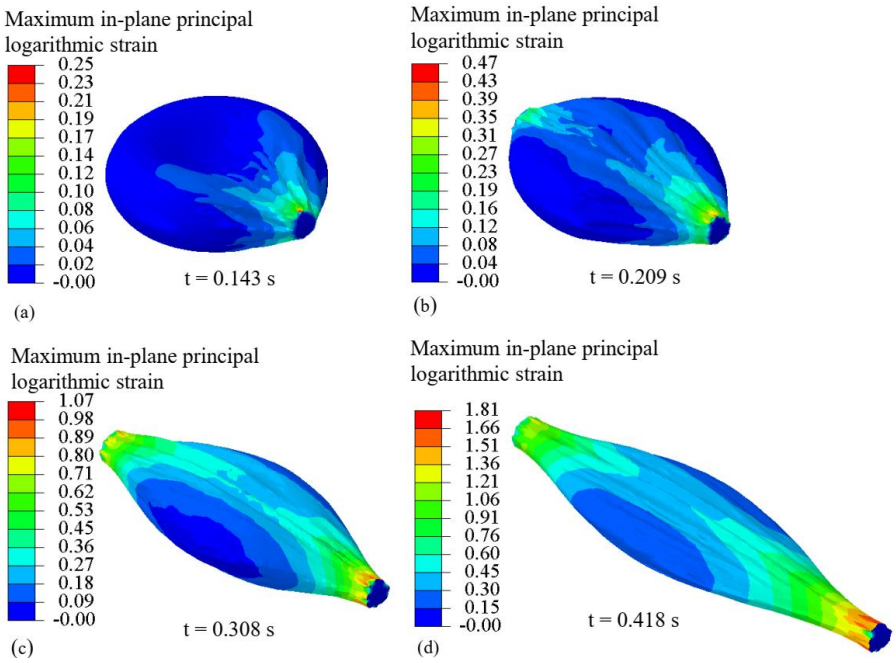


Figure 41: The contour plot of the erythrocyte membrane maximum principal logarithmic strain at various stages of optical tweezer simulation test, Maximum in-plane principal logarithmic strain of the erythrocyte membrane at 0.0143 s (a), 0.209 s (b), 0.308 s (c), and at 0.413 s (d).

### 4.3.2 Validation of the invasion model

The invasion model was validated by comparing the surface area of the erythrocyte with experimental erythrocyte areal deformation data obtained by tracking and segmenting the erythrocyte membrane during the invasion process (Geoghe*gan et a*l. 2021). The erythrocyte surface area obtained without applying blood pressure on the erythrocyte model's outer surface fits well with the experimental areal data of the erythrocyte membrane from the Geoghegan *et al.* (2021) also conducted without the application of blood pressure on the erythrocyte (see Figure 42). The maximum error between the areal data from Geoghe*gan et al*. (2021) and the developed invasion model is 5.2%. Additionally, when no surface pressure is applied on the erythrocyte model, the surface area of the erythrocyte model decreases, which is consistent with experimental data from Geoghegan *et al.* (2021) study (see Figure 42).

In contrast, when a blood pressure of 16 kPa is applied on the erythrocyte model's outer surface, the erythrocyte model's surface area increases during the late stages of the invasion process (see Figure 42).

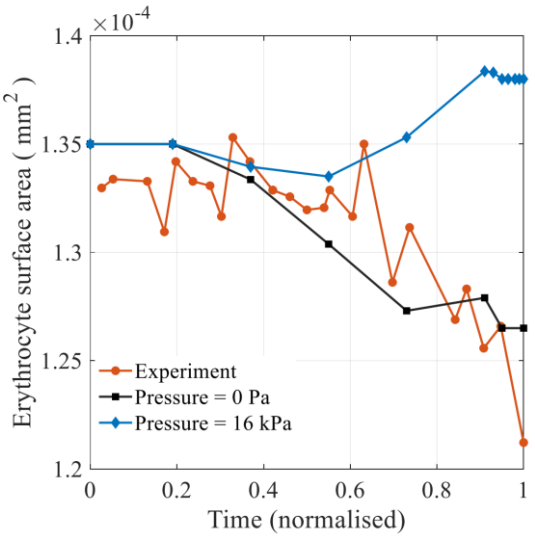


Figure 42: Experimental vs simulation data, showing the erythrocyte membrane surface areal variation when $\beta_1$=11 is induced from 0 to 0.1 s (Geoghegan *et al.* 2021).

The deformation of the erythrocyte model with the blood pressure of 16 kPa applied on its surface is entirely different from when no blood pressure is applied (see Figure 43).

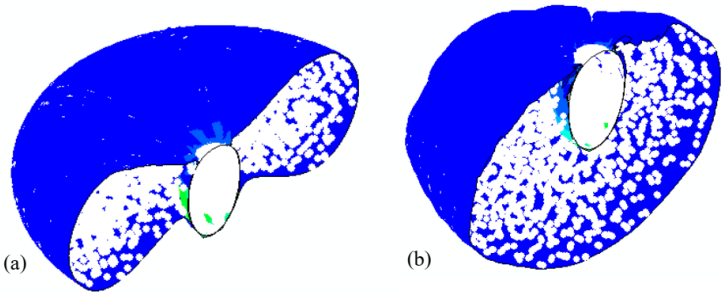


Figure 43: Deformation of an erythrocyte at 100% indentation depth normalised over the length of the malaria merozoite with (a) and without (b) blood pressure applied on the outer surface of the erythrocyte.

### 4.3.3 Impact of the erythrocyte morphology on the merozoite invasiveness

The impact of erythrocyte morphological variations on the invasiveness of the malaria merozoite is determined by the variation of the maximum strain energy of the invasion model, i.e. the maximum amount of energy required to facilitate successful invagination of the malaria merozoite. When the malaria merozoite invades through the convex region of the erythrocyte, the maximum strain energy value of the invasion model is $0.38 \times 10^{-15}$ J, and when it invades through the concave region of the erythrocyte, a lower value of $0.238 \times 10^{-15}$ J is obtained, representing a reduction of 37% of the maximum energy required to facilitate invagination of the malaria merozoite in the convex region of the erythrocyte (see Figure 44). This finding suggests that the malaria merozoite invagination requires 37% more energy when it occurs in the convex region than the concave regions of the erythrocyte.

Invasion of the spherocyte requires the largest maximum strain energy of 0.545 $\times 10^{-15}$ J, which is 43% and 129% larger than the energy required to invaginate the malaria merozoite in the convex and concave regions of the erythrocyte, respectively (see Figure 44).

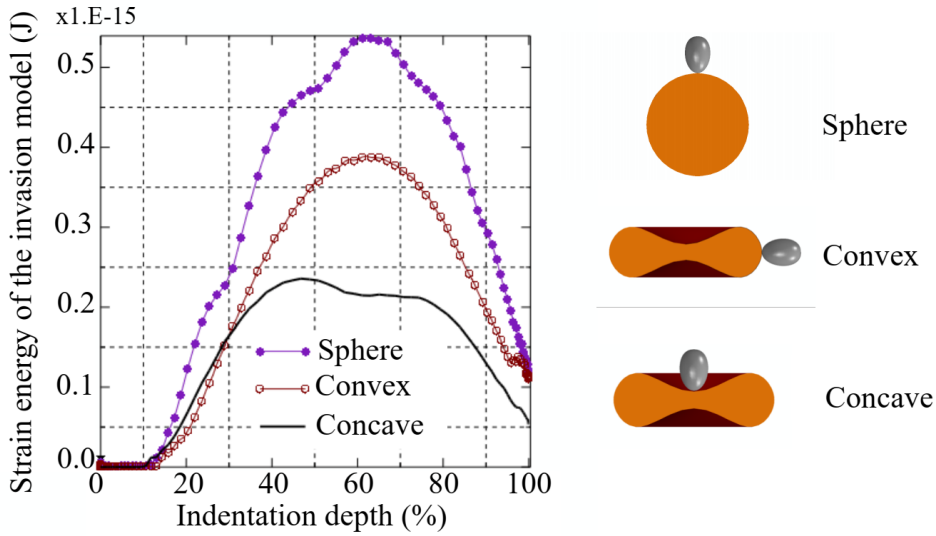


Figure 44: Strain energy of the invasion model representing the energy required to invaginate the malaria merozoite in the concave and convex regions of the erythrocyte and the spherocyte.

### 4.3.4 Impact of phosphorylation induced damage in the erythrocyte membrane on the merozoite invasiveness

The impact of malaria induced erythrocyte membrane damage on the invasiveness of the malaria merozoite is determined by the variation of the maximum indentation force required by the malaria merozoite to invade the erythrocyte, i.e. the maximum amount of force required to facilitate successful invagination of the malaria merozoite (see Figure 45). When the amount of damage increases by varying $\beta_1$, from 0 to 2.7, the maximum indentation force decreases (see Figure 45).

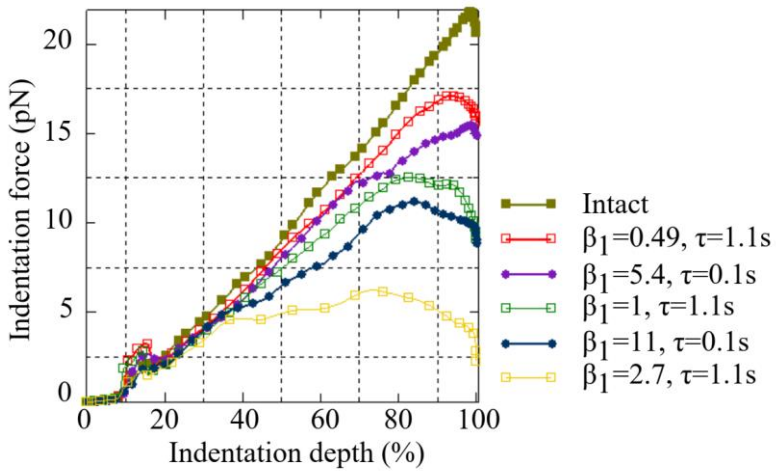


Figure 45: Indentation force vs indentation depth for varying degrees and timing of erythrocyte membrane damage.

When the erythrocyte membrane damage is induced for 9% (0–0.1 s) of the total simulation time ($\tau$ = 1.1 s), the observed maximum indentation forces are relatively lower than when an equal amount of erythrocyte membrane damage is induced for the entire simulation time (0–1.1 s) see Figure 45. For example, the amount of damage induced when $\beta_1$ = 0.49 for 0.1s is the same as when $\beta_1$ = 5.4 for 1.1 s. Similarly, equal damage is obtained when $\beta_1$ = 1 for 1.1s and when $\beta_1$ = 11 for 0.1s. The maximum indentation force for an intact erythrocyte membrane (22.4 pN) is larger than the maximum indentation force (17 pN) determined when damage is induced for the entire invasion process, i.e. when $\beta_1$ is set to 0.49 for 1.1 s. However, when an equal amount of erythrocyte membrane damage induced for the entire invasion process is induced for 0.1 s, the maximum indentation force (15 pN) is lower than the indentation force obtained when the damage parameter $\beta_1$ is set to 0.49 for 1.1 s. Similarly, the maximum indentation force determined when $\beta_1$ is set to 11 for 0.1 s is lower than when $\beta_1$ is set to 1 for 1.1 s. Hence, these results demonstrate that the malaria merozoite is more invasive when erythrocyte membrane damage occurs at the beginning of the invasion process.

### 4.3.5 Assessing the impact of local erythrocyte membrane on the global responses on the erythrocyte

#### 4.3.5.1 Erythrocyte compression

The compression forces versus compression displacement curves do not vary when damage is induced at damage locations 1 and 2 for a period of 0.1 s with $\beta_1 = 32$ (see Figure 46). This result shows that global indentation is insensitive to local damage induced in the erythrocyte membrane.

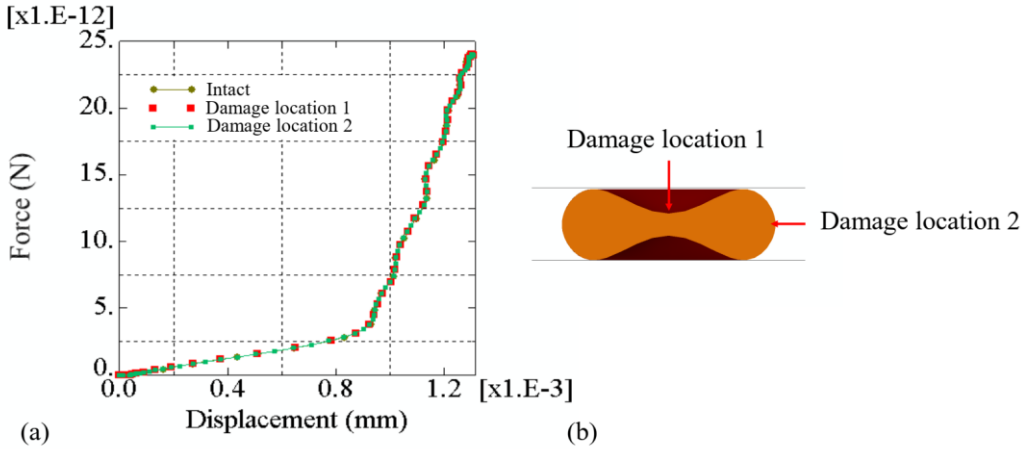


Figure 46: Compression force vs compression displacement data obtained from an intact erythrocyte and an erythrocyte damaged at damage locations 1 and 2.

#### 4.3.5.2 Erythrocyte nanoindentation

When the spherical indenter is displaced by 1.31 μm and no blood pressure is applied on the intact erythrocyte model, the erythrocyte membrane deforms such that the maximum principal logarithmic strain is 0.112 (see Figure 47a). However, when damage is induced at damage location 1, for 0.1 s, with $\beta_1 = 32$, the maximum principal logarithmic strain increases to 0.589 (see Figure 47b), but when damage is induced at damage location 2, the maximum principal logarithmic strain increases to 0.24 (see Figure 47c).

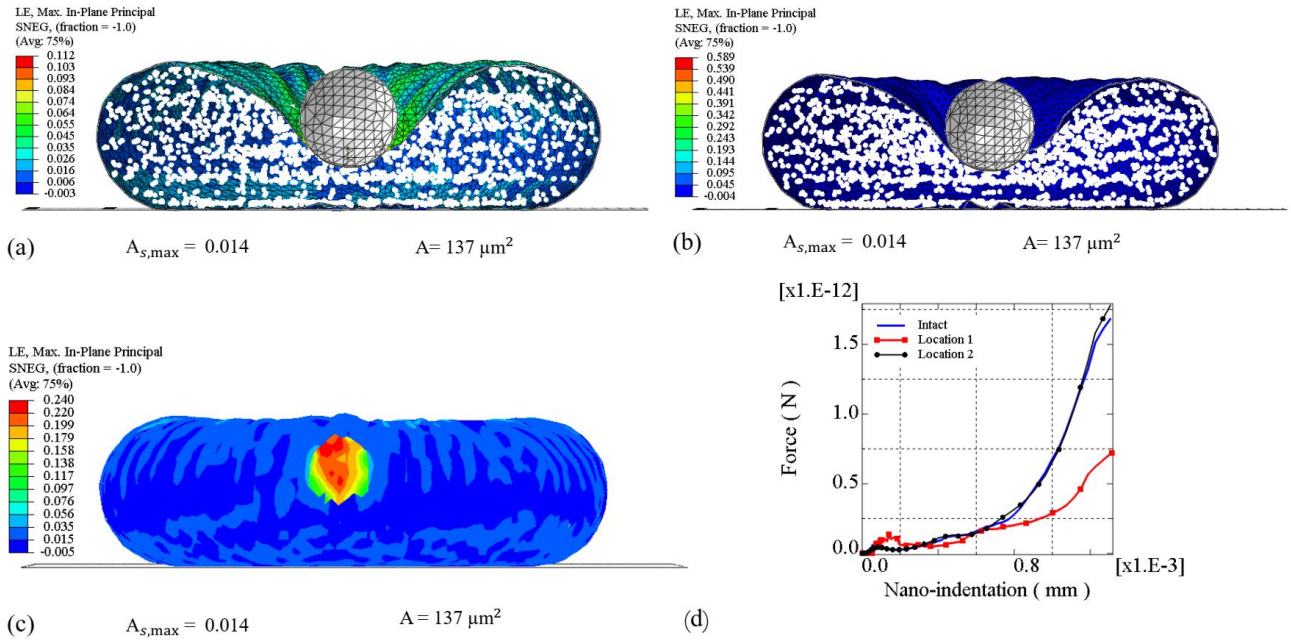


Figure 47: (a) Maximum principal logarithmic strain for the intact erythrocyte membrane (b) maximum principal logarithmic strain for the erythrocyte membrane obtained by inducing damage ($\beta_1$=32) for 0.1 s at damage location 1, where A and $A_{s,\,max}$ denotes the surface area and the areal ratio of the erythrocyte respectively, (c) maximum principal logarithmic strain in the erythrocyte membrane obtained by inducing damage for 0.1 s at damage location 2, where $\beta_1$ = 32, (d) indentation force vs nano-indentation for the intact erythrocyte membrane (blue), and when damage is induced at damage locations 1 (red), and 2 (black).

When the spherical indenter is displaced by 1.31 µm, the surface area of both intact and damaged erythrocyte increases from 135 µm$^2$ to 137 µm$^2$ such that the areal strain is 0.014 (see Figure 47 a, b, and c). When damage is induced at damage location 1 (the region of indentation), the maximum indentation force ($7.2\times10^{-13}$ N) is much lower than the indentation force ($1.78\times10^{-12}$ N) when damage is induced at damage location 2 (see Figure 47d). The maximum indentation force ($1.68\times10^{-12}$ N) required to deform an intact erythrocyte membrane and the erythrocyte membrane with damage at location 2 ($1.78\times10^{-12}$ N) are slightly different in magnitude (see Figure 47d).

## 4.4 Discussion

Although much progress has been achieved in understanding the factors that determine the invasiveness of the malaria merozoite, most of the previous studies do not address the collective role played by the biophysical factors of the erythrocyte deformability in the invasion process. Cell shape, cytoplasmic viscosity, membrane stability are the main factors determining the erythrocyte's deformability (Mohandas and Chasis 1993b, Mohandas and Evans 1994). To date, experimental data on the mechanical properties of a human erythrocyte is widely available. However, it remains unknown how these factors impact the invasiveness of the malaria merozoite. Hence, the current research aimed

to develop an in silico model for investigating the impact of erythrocyte morphology, malaria merozoite induced erythrocyte membrane damage on the invasiveness of the malaria merozoite.

### 4.4.1 Validation of the erythrocyte model

The developed erythrocyte model is a two-component model of the erythrocyte membrane and cytoplasm. The deformation of the intact erythrocyte membrane is modelled using the Mooney Rivlin law, which is equal to the developed erythrocyte membrane damage model when $\beta_1 = 0$. The deformation of erythrocyte cytoplasm makes use of the SPH formulation, which has been applied for the first time and hence the need to validate the developed erythrocyte model with experimental data. The diametric numerical data from the developed erythrocyte model is fitted with diametric data from the Mills *et al.* (2004) experiment to validate the developed erythrocyte model. The transverse diameters of the invasion model fit well with the transverse diameters from the Mills *et al.* (2004) experiment. However, the axial diameter of the developed erythrocyte model only fits the experimental data when the axial diameter does not exceed the threshold value of 0.0096 mm, which corresponds to the maximum principal logarithmic strain of the erythrocyte membrane of 1.81. Beyond this threshold value, the developed erythrocyte model has limited accuracy. For the invasion model, the maximum principal logarithmic strain of the erythrocyte membrane is 1.77, which is less than the threshold value of 1.81, thus indicating the erythrocyte model's deformation during the invasion process is within the determined accuracy range of the erythrocyte model.

### 4.4.2 Validation of the invasion model

The surface area of the erythrocyte from the Geoghegan *et al.* (2021) experiment where blood pressure was neglected agrees with the surface area of the developed erythrocyte FE model if blood pressure applied on the erythrocyte is neglected to mimic invitro experimental conditions. The surface area of the erythrocyte FE model is the region of the erythrocyte membrane that is not used to wrap the malaria merozoite. This surface area of the erythrocyte FE model decreases with time normalised over a step time of 1.1 s and is in good agreement with the surface area of the erythrocyte from experiments by Geoghegan *et al.* (2021). To allow direct comparison with the surface area of the developed invasion model, the surface area of the erythrocyte from Geoghegan *et al.* (2021) was normalised over a period of 49 s, which is the time when the malaria merozoite is entirely internalised (Geoghegan *et al.* 2021). The validated model is then used to predict the invasion process by applying in vivo conditions such as blood pressure which may be challenging in an in vitro experiment. The validation of the invasion model also allows the validation of the developed erythrocyte membrane damage model since the model predictions were in good agreement with experimental data when $\beta_1$ was set to 11 for 0.1 s.

Identifying the damage parameters enables the identification of the correct invasion forces required by the malaria merozoite to invade the erythrocyte.

### 4.4.3 Impact of the erythrocyte morphology on the merozoite invasiveness

The impact of erythrocyte membrane morphological variations on the invasiveness of the malaria merozoite was assessed by analysing the energetics for invasion in the concave and convex regions of the erythrocyte membrane. Additionally, the impact of shape variation between a healthy discoid erythrocyte and a spherocyte on the invasiveness of the malaria merozoite was also assessed. The malaria merozoite entry into the discoid erythrocyte requires lower invasion energy than the spherocyte. Reducing the erythrocyte's S/V ratio increases the sphericity of the erythrocyte and leads to the formation of the spherocyte. The relatively low energy requirement indicates that the malaria merozoite is more invasive when it invades a discoid shaped erythrocyte than when it invades a spherocyte. In other words increase in the sphericity corresponds to the increase in the energy required for the malaria merozoite to invade the erythrocyte. The surface area to volume ratio (S/V) of 1.44/m allows a healthy erythrocyte to undergo a large deformation of up to 230 % of its original dimension. Reducing the healthy erythrocyte's S/V ratio by 14% forms a spherocyte with a surface area of 98.5 $\mu m^2$ which is less than the surface area of a healthy erythrocyte. Hence the discoid shape provides approximately 36.5 $\mu m^2$ of excess surface area, 4.6 times the merozoite surface area of 8.0 $\mu m^2$ (Dasgupta *et al.* 2014), thus providing sufficient surface area to facilitate wrapping of the malaria merozoite. The maximum strain energy predicted with the FE invasion model is equivalent to the total indentation work described by the developed analytical model. The maximum strain energy of $38 \times 10^{-17}$ J and $23.8 \times 10^{-17}$ J predicted with the FE invasion model for invasion in the convex and concave erythrocyte membrane region is 50%  60% larger the total indentation work of $E_i = 1.40 \times 10^{-17}$ J predicted by the analytical model for $A_{s,max} = 51\%$. The higher strain energy of the FE invasion model may be due to the work done to deform the erythrocyte cytoplasm which is not considered in the analytical model.

Erythrocytes with membrane protein abnormalities such as hereditary spherocytosis are generally spherical and less deformable than normal discoid erythrocytes. However, to date, it is not known if these alterations may present the merozoite with a less ideal condition for invasion of erythrocyte by malaria merozoites. Spherocytes have been found to have a low susceptibility to invasion by a malaria merozoite. One of the reasons for low susceptibility is the genetic alteration of membrane proteins. However, from the current study, it has been determined that shape alteration of the erythrocyte to

spherical shape could be one of the contributing factors for the low susceptibility of spherocytes to infection by malaria merozoites.

### 4.4.4 Impact of phosphorylation induced damage in the erythrocyte membrane on the merozoite invasiveness

The impact of erythrocyte membrane damage on the invasiveness of the malaria merozoite was studied by inducing erythrocyte membrane damage locally. The amount of damage induced in the erythrocyte membrane model was regulated by varying damage parameters $\beta_1$ between 0.49 and 2.7 such that $\beta_1 = 0.49$ represented the minimum amount of damage while $\beta_1 = 2.7$ represented the maximum amount of damage. The invasiveness of the malaria merozoite was assessed by comparing the maximum indentation forces for each value of the damage parameter $\beta_1$.

The indentation forces decrease with the increasing amount of damage induced in the erythrocyte membrane model (see Figure 45). This demonstrates that the invasiveness of the malaria merozoite increases with the amount of damage. Malaria merozoite induced erythrocyte membrane damage research has received limited attention. To date, the stages of erythrocyte membrane remodelling or damage are unknown. in other words, it is not known whether this damage is only induced at the early stages of invasion or throughout the entire invasion process. However, to validate the developed invasion model, erythrocyte membrane damage was induced at the beginning of the invasion process i,e, when $\beta_1$ was set to 11 for 0.1 s. This finding suggests that erythrocyte membrane damage occurs during an early invasion process. The forces required by the malaria merozoite when damage is induced progressively throughout the entire invasion, i.e., for a period of 1.1 s, are larger than when damage is induced for a period of 0.1 s, i.e., at the beginning of the invasion process. These results demonstrate that the malaria merozoite is more invasive when damage is induced from 0 - 0.1 s than when induced progressively throughout the entire invasion process. Hence regulating the timing at which the malaria merozoite induces erythrocyte membrane damage could be a potential target for antimalarial compounds.

### 4.4.5 Assessing the impact of local erythrocyte membrane on the global mechanical responses of the erythrocyte

Compression test simulations investigated the impact of local erythrocyte membrane damage on a global scale. The compression tests indicate that the compression forces vary with compression depth but does not vary with local erythrocyte membrane damage because the compressive forces of an intact

and damaged erythrocyte have the same magnitudes. This result demonstrates that a compression experiment cannot be successfully used to investigate erythrocyte membrane damage.

The nano-indentation simulation predicted that the indentation force varies with the indentation depth and local erythrocyte membrane damage when both the indentation and local erythrocyte membrane damage occur in the concave region of the erythrocyte. However, when the indentation is applied in the concave region of the erythrocyte and erythrocyte membrane, the damage is applied in the convex region of the erythrocyte membrane; the indentation force only varies with the indentation depth but not with the local erythrocyte membrane damage. This result demonstrates that the local erythrocyte membrane damage only impacts the deformation of the erythrocyte locally and not globally. Hence nano-indentation experiments can only investigate the impact of erythrocyte membrane damage on the erythrocyte deformation locally and not globally.

The developed FE invasion model has only highlighted the importance of timing erythrocyte membrane damage on the invasiveness of the malaria merozoite. However, to further explore the impact of timing erythrocyte membrane damage experimentally, nano-indentation studies can be conducted to study the impact of various stages of erythrocyte membrane damage on the invasion energetics.

# 5 Conclusions, novel aspects, and recommendations

This PhD thesis aimed to (1) analytically and computationally investigate the mechanical factors that determine the invasiveness of a malaria merozoite during its entry into an erythrocyte and (2) evaluate the impact of local membrane damage on an erythrocyte's regional and global mechanical properties towards cell mechanics profiling of invasion blocking anti-malarial compounds that target erythrocyte membrane damage mechanism.

The following objectives were defined to achieve the above aims:

Objective 1: To develop an analytical model for establishing the major factors facilitating erythrocyte membrane wrapping of a malaria merozoite.

Objective 2: To develop an erythrocyte membrane damage model for simulating the malaria merozoite induced damage during the invasion process.

Objective 3: To develop a finite element model for evaluating the malaria merozoite's invasiveness during its entry into the erythrocyte.

Objective 4: To investigate computationally the sensitivity of cell mechanics tests, namely whole-cell compression and nanoindentation, to local erythrocyte membrane damage induced by malaria merozoites.

## 5.1 An analytical model of the mechanics of erythrocyte membrane wrapping during the active invasion of erythrocyte by the malaria merozoite

The analytical model was developed to study the mechanics of erythrocyte membrane wrapping of the malaria merozoite. With the developed analytical model, two sets of numerical solutions have been presented to describe the constitutive response of the erythrocyte membrane during erythrocyte membrane wrapping of the invading malaria merozoite. One set of numerical solutions was associated with a small areal strain ranging between 0-4%, and the other involved a sizeable areal strain ranging between 0-50%. Furthermore, the developed analytical model has established the relationship between the biophysical forces required to facilitate wrapping of the malaria merozoite and the areal strain of the erythrocyte membrane, i.e., small areal strain (between 0-4%) and finite areal strain (between 0-51%). The erythrocyte membrane stresses due to small (between 0-4%), and finite areal strain (between 0-51 %) have also been predicted. The effect of the malaria merozoite induced erythrocyte membrane skeleton dissociation on the biophysical forces and invasion energetics have been investigated. The numerical data from the developed analytical model suggests that the large

erythrocyte surface area due to its discoid shape increases the invasiveness of the malaria parasite and thus suggest its high susceptibility to infection by the malaria merozoites. The energetics of the invasion process have also been analysed. The data obtained from the developed analytical model shows that the energy required by the malaria merozoite reaches its maximum value during the middle stage of the invasion process but decreases during the late stages of the invasion process. This finding provides theoretical insights on how the malaria merozoite would utilise and regulate its energy to maximize its invasion efficiency. The developed analytical model has limitations, mainly due to the restriction to 2D analysis and the lack of experimental data for calibrating the 2D analytical model. However, the analytical model can be effectively used for parametric studies to assess the malaria merozoite's invasiveness. Additionally, the analytical model does not consider the cytoplasm, and hence the addition of the erythrocyte cytoplasmic domain is recommended for future analysis.

**Novelty**: This is the first analytic model that (a) predicts the malaria merozoites invagination forces generated by the merozoite actomyosin machinery, and (b) assess the invasiveness of the malaria merozoite based on mechanical aspects of the erythrocyte membrane.

## 5.2 A constitutive model for the remodelling erythrocyte membrane skeleton during the active invasion by the malaria merozoite

The erythrocyte membrane damage model was developed for studying the impact of the malaria merozoite induced damage on its invasiveness. To date, experimental investigations related to erythrocytes' invasion have predominantly focused on the role of parasite adhesins or signalling pathways and the identity of binding receptors on the erythrocyte cell surface. The erythrocyte membrane damage mechanics associated with the invasion process has received limited attention (Koch *et al.* 2017).

The erythrocyte membrane damage model was developed by modifying the Mooney Rivlin law, where the exponential damage variable function was incorporated to induce the remodelling effect. The developed damage model was implemented for finite element analysis application by using the user material subroutine. Despite limited knowledge of the malaria merozoite induced damage, the model allowed various amounts of damage to be induced. It was found that the malaria merozoite becomes more invasive with an increasing amount of damage. Various erythrocyte membrane constitutive responses obtained from the developed erythrocyte membrane damage model have been presented in terms of the Yeoh, Reduced polynomial, and Ogden model to easily implement the erythrocyte membrane damage model. The material parameters of the Yeoh, Reduced polynomial, and the Ogden

models and their stability thresholds have been presented in Appendix A. The main limitation of the damage model is the possible instability of the Mooney Rivlin law at low strain. Furthermore, the second invariant of the left Cauchy tensor of the Mooney Rivlin law can make the model unstable in certain loading conditions. However, the decrease of the erythrocyte membrane stability threshold predicted with the developed model for increasing damage amount corresponds with reports that the phosphorylation of key protein elements of the erythrocyte skeleton leads to an unstable erythrocyte membrane.

**Novelty**: The developed erythrocyte membrane damage model is the first to predict erythrocyte membrane damage induced by the malaria merozoite. With the damage model, various degrees and stages of damage have been studied for the first time to predict the invasiveness of the malaria merozoite.

## 5.3 A finite element model for the invasion of human erythrocytes by a plasmodium falciparum merozoite

The finite element invasion model was developed to investigate the malaria merozoite's entry mechanic. New insights obtained from the entry simulations of the malaria merozoite are aimed to guide the development of experimental investigations for assessing the invasiveness of the malaria merozoite. Human erythrocytes are often subjected to large deformations, and to accurately model the erythrocyte's cytoplasm, excessive mesh distortion should be allowed without causing any numerical errors. One way of coping with the excessive mesh distortions is by using the Lagrangian smoothed particle hydrodynamics formulation, a meshless approach that provides an excellent solution to the problem of extreme mesh distortions. The SPH formulation has been applied for the first time to model erythrocyte cytoplasm deformation. Hence required validation of the developed erythrocyte model against experimental data. Optical trap experimental data has been successfully used to validate the developed erythrocyte model. The accuracy threshold of the developed erythrocyte model has been established at a maximum principal logarithmic strain of 0.112. The accuracy of the invasion FE model was also validated with experimental data of merozoite invasion into a human erythrocyte from Geoghegan *et al.* (2021). With the developed FE invasion model, the impact of erythrocyte shape and erythrocyte membrane damage on the invasiveness of the malaria merozoite has been extensively investigated. The simulations have established that the increase in sphericity of the erythrocyte reduces the invasiveness of the malaria merozoite.

In contrast, an increasing amount of damage increases the invasiveness of the malaria merozoite. Additionally, the impact of timing merozoite's induced damage was investigated, and it was found that the malaria merozoite is more invasive when erythrocyte membrane damage is induced at an early stage of the invasion process. However, further nano-indentation experimental studies are required to investigate the impact of the timing erythrocyte's membrane damage on indentation force. The results from the nano-indentation simulation indicate the suitability of nanoindentation experiments to investigate erythrocyte membrane damage.

**Novelty**: The developed FE invasion model is the first model to predict the malaria merozoite's invasiveness based on factors that determine the erythrocyte's deformability. With the developed invasion model, the impact of erythrocyte shape, and erythrocyte membrane damage, on the invasiveness of the malaria merozoite have been studied for the first time. An increase in sphericity of the erythrocyte reduces the invasiveness, while the increase in the amount of erythrocyte membrane damage increases the invasiveness of the malaria merozoite. The force and the amount of erythrocyte membrane damage required by the malaria merozoite to successfully invade the erythrocyte have been predicted for the first time. The maximum force required by the malaria merozoite is 11 pN, with $\beta_1$ = 11 induced for 0.1 s representing the amount of damage induced by the malaria merozoite.

## Publication plan

The three manuscripts from the presented work will be submitted for journal publication within twelve months after submitting this thesis.

Manuscript 1: Analytical model of the mechanics of erythrocyte membrane wrapping during the active invasion by a plasmodium falciparum merozoite (based on thesis chapter 2)

Manuscript 2: Constitutive model for the remodelling erythrocyte membrane spectrin network during the active invasion by a malaria merozoite (based on thesis chapter 3)

Manuscript 3: Finite element analysis of the invasion of a human erythrocyte by a plasmodium falciparum merozoite (based on thesis chapter 4)

## Data availability

The data supporting this thesis can be accessed on the University of Cape Town's institutional data repository (ZivaHub) under the doi https://doi.org/10.25375/uct.17430329 from 1 March 2023 or upon request.

# References


Abdalrahman T, Franz T. *Analytical modeling of the mechanics of early invasion of a merozoite into a human erythrocyte*. J Biol Phys 2017a, **43**(4): 471-9.

Abdalrahman T, Franz T. *Analytical modeling of the mechanics of early invasion of a merozoite into a human erythrocyte*. Journal of Biological Physics 2017b, **43**(4): 471-9.

Arruda EM, Boyce MC. *A three-dimensional constitutive model for the large stretch behavior of rubber elastic materials*. Journal of the Mechanics and Physics of Solids 1993, **41**(2): 389-412.

Austrell P-E, Kari L, Eds. Constitutive Models for Rubber IV : Proceedings of the 4th European Conference for Constitutive Models for Rubber, ECCMR 2005, Stockholm, Sweden, 27-29 June 2005. Constitutive Models for Rubber. London, Taylor & Francis, 2005.

Balzani D, Schröder J, Gross D. *Simulation of discontinuous damage incorporating residual stresses in circumferentially overstretched atherosclerotic arteries*. Acta Biomaterialia 2006, **2**(6): 609-18.

Bergström J. *Elasticity/Hyperelasticity*. in Bergström J (Ed. Mechanics of solid polymers, William Andrew Publishing, 2015, https://doi.org/10.1016/B978-0-323-31150-2.00005-4: 209-307.

Bergstrom JS. Mechanics of solid polymers: theory and computational modeling, William Andrew, 2015.

Betz T, Lenz M, Joanny JF, Sykes C. *ATP-dependent mechanics of red blood cells*. Proceedings of the National Academy of Sciences of the United States of America 2009, **106**(36): 15320-5.

Bower A. *Applied mechanics of solids*, Taylor & Francis, Boca Raton, Florida, 2010.

Calvo B, Peña E, Martínez M, Doblaré M. *An uncoupled directional damage model for fibred biological soft tissues. Formulation and computational aspects*. International Journal for Numerical Methods in Engineering 2007a, **69**: 2036-57.

Calvo B, Peña E, Martinez MA, Doblaré M. *An uncoupled directional damage model for fibred biological soft tissues. Formulation and computational aspects*. International Journal for Numerical Methods in Engineering 2007b, **69**(10): 2036-57.

Chee CY, Lee HP, Lu C. *Using 3D fluid–structure interaction model to analyse the biomechanical properties of erythrocyte*. Physics Letters A 2008, **372**(9): 1357-62.

Chen MZ, Boyle FJ. *Investigation of membrane mechanics using spring networks: Application to red-blood-cell modelling*. Materials Science & Engineering C-Materials for Biological Applications 2014, **43**: 506-16.

Cohen P. *The regulation of protein function by multisite phosphorylation--a 25 year update*. Trends Biochem Sci 2000, **25**(12): 596-601.

Cohen P. *The origins of protein phosphorylation*. Nat Cell Biol 2002, **4**(5): E127-30.

Cowman AF, Crabb BS. *Invasion of red blood cells by malaria parasites*. Cell 2006, **124**(4): 755-66.

Dasgupta S, Auth T, Gov NS, Satchwell TJ, Hanssen E, Zuccala ES, Riglar DT, Toye AM, Betz T, Baum J, Gompper G. *Membrane-Wrapping Contributions to Malaria Parasite Invasion of the Human Erythrocyte*. Biophysical Journal 2014, **107**(1): 43-54.

Dimitrakopoulos P. *Analysis of the variation in the determination of the shear modulus of the erythrocyte membrane: Effects of the constitutive law and membrane modeling*. Physical review E: Statistical, nonlinear, and soft matter physics 2012, **85**(4 Pt 1): 041917-.

Discher DE, Winardi R, Schischmanoff PO, Parra M, Conboy JG, Mohandas N. *Mechanochemistry of protein 4.1's spectrin-actin-binding domain: ternary complex interactions, membrane binding, network integration, structural strengthening*. J Cell Biol 1995, **130**(4): 897-907.

Eber S, Lux SE. *Hereditary spherocytosis--defects in proteins that connect the membrane skeleton to the lipid bilayer*. Seminars in Hematology 2004, **41**(2): 118-41.

Fai TG, Leo-Macias A, Stokes DL, Peskin CS. *Image-based model of the spectrin cytoskeleton for red blood cell simulation*. PLOS Computational Biology 2017, **13**(10): e1005790.

Fedosov DA, Lei H, Caswell B, Suresh S, Karniadakis GE. *Multiscale Modeling of Red Blood Cell Mechanics and Blood Flow in Malaria*. PLOS Computational Biology 2011, **7**(12): e1002270.

Ferru E, Giger K, Pantaleo A, Campanella E, Grey J, Ritchie K, Vono R, Turrini F, Low PS. *Regulation of membrane-cytoskeletal interactions by tyrosine phosphorylation of erythrocyte band 3*. Blood 2011, **117**(22): 5998-6006.

Flannery EL, Chatterjee AK, Winzeler EA. *Antimalarial Drug Discovery: Approaches and Progress towards New Medicines*. Nature reviews Microbiology 2013, **11**(12): 849-62.

Geoghegan ND, Evelyn C, Whitehead LW, Pasternak M, Mcdonald P, Triglia T, Marapana DS, Kempe D, Thompson JK, Mlodzianoski MJ, Healer J, Biro M, Cowman AF, Rogers KL. *4D analysis of malaria parasite invasion offers insights into erythrocyte membrane remodeling and parasitophorous vacuole formation*. Nature Communications 2021, **12**(1): 3620.

Gilson PR, Crabb BS. *Morphology and kinetics of the three distinct phases of red blood cell invasion by Plasmodium falciparum merozoites*. International Journal for Parasitology 2009, **39**(1): 91-6.

Gingold RA, Monaghan JJ. *Smoothed particle hydrodynamics: theory and application to non-spherical stars*. Monthly Notices of the Royal Astronomical Society 1977, **181**(3): 375-89.

Guiguemde WA, Shelat AA, Bouck D, Duffy S, Crowther GJ, Davis PH, Smithson DC, Connelly M, Clark J, Zhu F, Jiménez-Díaz MB, Martinez MS, Wilson EB, Tripathi AK, Gut J, Sharlow ER, Bathurst I, El Mazouni F, Fowble JW, Forquer I, Mcginley PL, Castro S, Angulo-Barturen I,

Ferrer S, Rosenthal PJ, Derisi JL, Sullivan DJ, Lazo JS, Roos DS, Riscoe MK, Phillips MA, Rathod PK, Van Voorhis WC, Avery VM, Guy RK. *Chemical genetics of Plasmodium falciparum*. Nature 2010, **465**(7296): 311-5.

Harvey KL, Gilson PR, Crabb BS. *A model for the progression of receptor-ligand interactions during erythrocyte invasion by Plasmodium falciparum*. International Journal for Parasitology 2012, **42**(6): 567-73.

Hochmuth RM, Mohandas N, Blackshear PL. *Measurement of the Elastic Modulus for Red Cell Membrane Using a Fluid Mechanical Technique*. Biophysical Journal 1973, **13**(8): 747-62.

Ida Laila Ahmad MRA. *A two component red blood cell model for single cell mechanic*. Asian Research Publishing Network Journal of Engineering and Applied Sciences 2015, **10**(19): 8885-93.

Introini V, Marin-Menendez A, Nettesheim G, Lin Y-C, Kariuki SN, Smith AL, Jean L, Brewin JN, Rees DC, Cicuta P, Rayner JC, Penman BS. *The erythrocyte membrane properties of beta thalassaemia heterozygotes and their consequences for Plasmodium falciparum invasion*. Scientific Reports 2022, **12**(1): 8934.

Jaskiewicz E, Jodłowska M, Kaczmarek R, Zerka A. *Erythrocyte glycophorins as receptors for Plasmodium merozoites*. Parasites and Vectors 2019, **12**(1): 317.

Kachanov LM. *Rupture Time Under Creep Conditions*. International Journal of Fracture 1999, **97**(1): 11-8.

Kim B, Lee SB, Lee J, Cho S, Park H, Yeom S, Park SH. *A comparison among Neo-Hookean model, Mooney-Rivlin model, and Ogden model for chloroprene rubber*. International Journal of Precision Engineering and Manufacturing 2012, **13**(5): 759-64.

Koch M, Baum J. *The mechanics of malaria parasite invasion of the human erythrocyte – towards a reassessment of the host cell contribution*. International Journal for Parasitology 2016, **18**(3): 319-29.

Koch M, Wright KE, Otto O, Herbig M, Salinas ND, Tolia NH, Satchwell TJ, Guck J, Brooks NJ, Baum J. *Plasmodium falciparum erythrocyte-binding antigen 175 triggers a biophysical change in the red blood cell that facilitates invasion*. Proceedings of the National Academy of Sciences of the United States of America 2017, **114**(16): 4225-30.

Law R, Carl P, Harper S, Dalhaimer P, Speicher DW, Discher DE. *Cooperativity in Forced Unfolding of Tandem Spectrin Repeats*. Biophysical Journal 2003, **84**(1): 533-44.

Leitgeb AM, Charunwatthana P, Rueangveerayut R, Uthaisin C, Silamut K, Chotivanich K, Sila P, Moll K, Lee SJ, Lindgren M, Holmer E, Färnert A, Kiwuwa MS, Kristensen J, Herder C, Tarning J, Wahlgren M, Dondorp AM. *Inhibition of merozoite invasion and transient de-*

*sequestration by sevuparin in humans with Plasmodium falciparum malaria*. PLOS one 2017, **12**(12): e0188754.

Li F, Chan CU, Ohl CD. *Yield strength of human erythrocyte membranes to impulsive stretching*. Biophysical Journal 2013, **105**(4): 872-9.

Li H, Lu L, Li X, Buffet PA, Dao M, Karniadakis GE, Suresh S. *Mechanics of diseased red blood cells in human spleen and consequences for hereditary blood disorders*. Proceedings of the National Academy of Sciences 2018, **115**(38): 9574-9.

Li J, Lykotrafitis G, Dao M, Suresh S. *Cytoskeletal dynamics of human erythrocyte*. Proceedings of the National Academy of Sciences of the United States of America 2007, **104**(12): 4937-42.

Li X, Peng Z, Lei H, Dao M, Karniadakis GE. *Probing red blood cell mechanics, rheology and dynamics with a two-component multi-scale model*. Philos Trans A Math Phys Eng Sci 2014a, **372**(2021).

Li X, Peng Z, Lei H, Dao M, Karniadakis GE. *Probing red blood cell mechanics, rheology and dynamics with a two-component multi-scale model*. Philosophical Transaction A: Mathematical, Physical and Engeering Sciences 2014b, **372**(2021).

Lim CT, Zhou EH, Quek ST. *Mechanical models for living cells--a review*. Journal of Biomechanical Engineering 2006, **39**(2): 195-216.

Linderkamp O, Meiselman HJ. *Geometric, osmotic, and membrane mechanical properties of density-separated human red cells*. Blood 1982, **59**(6): 1121-7.

Machnicka B, Czogalla A, Hryniewicz-Jankowska A, Bogusławska DM, Grochowalska R, Heger E, Sikorski AF. *Spectrins: a structural platform for stabilization and activation of membrane channels, receptors and transporters*. Biochim Biophys Acta 2014, **1838**(2): 620-34.

Manno S, Takakuwa Y, Nagao K, Mohandas N. *Modulation of erythrocyte membrane mechanical function by beta-spectrin phosphorylation and dephosphorylation*. Journal of Biological Chemistry 1995, **270**(10): 5659-65.

Marckmann G, Verron E. *Comparison of Hyperelastic Models for Rubber-Like Materials*. Rubber Chemistry and Technology 2006, **79**(5): 835-58.

Mills JP, Qie L, Dao M, Lim CT, Suresh S. *Nonlinear elastic and viscoelastic deformation of the human red blood cell with optical tweezers*. Mechanics and Chemistry of Biosystems 2004, **1**(3): 169-80.

Mohandas N, Chasis JA. *Red blood cell deformability, membrane material properties and shape: regulation by transmembrane, skeletal and cytosolic proteins and lipids*. Seminars in Hematology 1993a, **30**(3): 171-92.

Mohandas N, Chasis JA. *Red blood cell deformability, membrane material properties and shape: regulation by transmembrane, skeletal and cytosolic proteins and lipids*. Semin Hematol 1993b, **30**(3): 171-92.

Mohandas N, Evans E. *Mechanical properties of the red cell membrane in relation to molecular structure and genetic defects*. Annu Rev Biophys Biomol Struct 1994, **23**: 787-818.

Mohandas N, Gallagher PG. *Red cell membrane: past, present, and future*. Blood 2008, **112**(10): 3939-48.

Mohandas N, Phillips WM, Bessis M. *Red blood cell deformability and hemolytic anemias*. Seminars in Hematology 1979, **16**(2): 95-114.

Monaghan JJ. *An introduction to SPH*. Computer Physics Communications 1988, **48**(1): 89-96.

Murakami S. Continuum damage mechanics: a continuum mechanics approach to the analysis of damage and fracture, Springer Science & Business Media, 2012.

Ogden RW. *Nearly isochoric elastic deformations: Application to rubberlike solids*. Journal of the Mechanics and Physics of Solids 1978, **26**(1): 37-57.

Ogden RW, Roxburgh DG. *A pseudo elastic model for the Mullins effect in filled rubber*. Proceedings of the Royal Society of London Series A: Mathematical, Physical and Engineering Sciences 1999, **455**(1988): 2861-77.

Omori T, Ishikawa T, Barthès-Biesel D, Salsac AV, Walter J, Imai Y, Yamaguchi T. *Comparison between spring network models and continuum constitutive laws: application to the large deformation of a capsule in shear flow*. Phys Rev E Stat Nonlin Soft Matter Phys 2011a, **83**(4 Pt 1): 041918.

Omori T, Ishikawa T, Barthès-Biesel D, Salsac AV, Walter J, Imai Y, Yamaguchi T. *Comparison between spring network models and continuum constitutive laws: application to the large deformation of a capsule in shear flow*. Physical review E: Statistical, nonlinear, and soft matter physics 2011b, **83**(4 Pt 1): 041918.

Ostoja-Starzewski M. *Lattice models in micromechanics*. Applied Mechanics Reviews 2002, **55**(1): 35-60.

Ostoja-Starzewski M, Sheng PY, Alzebdeh K. *Spring network models in elasticity and fracture of composites and polycrystals*. Computational Materials Science 1996, **7**(1-2): 82-93.

Paul AS, Egan ES, Duraisingh MT. *Host-parasite interactions that guide red blood cell invasion by malaria parasites*. Current Opinion in Hematology 2015, **22**(3): 220-6.

Peña E, Calvo B, Martínez M, Doblaré M. *On finite-strain damage of viscoelastic-fibred materials. Application to soft biological tissues*. International Journal for Numerical Methods in Engineering 2008, **74**(7): 1198-218.

Peña E, Peña JA, Doblaré M. *On the Mullins effect and hysteresis of fibered biological materials: A comparison between continuous and discontinuous damage models*. International Journal of Solids and Structures 2009, **46**(7): 1727-35.

Plouffe D, Brinker A, Mcnamara C, Henson K, Kato N, Kuhen K, Nagle A, Adrián F, Matzen JT, Anderson P, Nam T-G, Gray NS, Chatterjee A, Janes J, Yan SF, Trager R, Caldwell JS, Schultz PG, Zhou Y, Winzeler EA. *In silico activity profiling reveals the mechanism of action of antimalarials discovered in a high-throughput screen*. Proceedings of the National Academy of Sciences of the United States of America 2008, **105**(26): 9059-64.

Qi D, Kaur Gill N, Santiskulvong C, Sifuentes J, Dorigo O, Rao J, Taylor-Harding B, Ruprecht Wiedemeyer W, Rowat AC. *Screening cell mechanotype by parallel microfiltration*. Scientific Reports 2015, **5**: 17595.

Riglar DT, Richard D, Wilson DW, Boyle MJ, Dekiwadia C, Turnbull L, Angrisano F, Marapana DS, Rogers KL, Whitchurch CB, Beeson JG, Cowman AF, Ralph SA, Baum J. *Super-resolution dissection of coordinated events during malaria parasite invasion of the human erythrocyte*. Cell Host Microbe 2011, **9**(1): 9-20.

Rodriguez JF, Alastrue V, Doblare M. *Finite element implementation of a stochastic three dimensional finite-strain damage model for fibrous soft tissue*. Computer Methods in Applied Mechanics and Engineering 2008, **197**(9): 946-58.

Rottmann M, Mcnamara C, Yeung BKS, Lee MCS, Zou B, Russell B, Seitz P, Plouffe DM, Dharia NV, Tan J, Cohen SB, Spencer KR, González-Páez GE, Lakshminarayana SB, Goh A, Suwanarusk R, Jegla T, Schmitt EK, Beck H-P, Brun R, Nosten F, Renia L, Dartois V, Keller TH, Fidock DA, Winzeler EA, Diagana TT. *Spiroindolones, a new and potent chemotype for the treatment of malaria*. Science (New York) 2010, **329**(5996): 1175-80.

Saito M, Watanabe-Nakayama T, Machida S, Osada T, Afrin R, Ikai A. *Spectrin-ankyrin interaction mechanics: A key force balance factor in the red blood cell membrane skeleton*. Biophysical Chemistry 2015, **200-201**: 1-8.

Singh S, Alam MM, Pal-Bhowmick I, Brzostowski JA, Chitnis CE. *Distinct External Signals Trigger Sequential Release of Apical Organelles during Erythrocyte Invasion by Malaria Parasites*. PLOS Pathogens 2010, **6**(2): e1000746.

Sisquella X, Nebl T, Thompson JK, Whitehead L, Malpede BM, Salinas ND, Rogers K, Tolia NH, Fleig A, O'neill J, Tham WH, David Horgen F, Cowman AF. *Plasmodium falciparum ligand binding to erythrocytes induce alterations in deformability essential for invasion*. Elife 2017, **6**.

Skalak R, Tozeren A, Zarda RP, Chien S. *Strain Energy Function of Red Blood Cell Membranes*. Biophysical Journal 1973, **13**(3): 245-64.

Song H, Liu Y, Zhang B, Tian K, Zhu P, Lu H, Tang Q. *Study of in vitro RBCs membrane elasticity with AOD scanning optical tweezers*. Biomedical Optics Express 2017, **8**(1): 384-94.

Systemes D. *Abaqus 6.14 documentation–theory guide*. Providence, RI 2015.

Tomaiuolo G. *Biomechanical properties of red blood cells in health and disease towards microfluidics*. Biomicrofluidics 2014, **8**(5): 051501.

Unsain N, Stefani FD, Cáceres A. *The Actin/Spectrin Membrane-Associated Periodic Skeleton in Neurons*. Frontiers in Synaptic Neuroscience 2018, **10**.

Vieira AC, Marques AT, Guedes RM, Tita V. *Material model proposal for biodegradable materials*. Procedia Engineering 2011, **10**: 1597-602.

Villaggio P. Mathematical Models for Elastic Structures. Cambridge, Cambridge University Press, 1997.

Violeau D, Rogers BD. *Smoothed particle hydrodynamics (SPH) for free-surface flows: past, present and future*. Journal of Hydraulic Research 2016, **54**(1): 1-26.

Wang C, Wang Y, Peng C, Meng X. *Smoothed particle hydrodynamics simulation of water-soil mixture flows*. Journal of Hydraulic Engineering 2016, **142**(10): 04016032.

Weiss JA. *A constitutive model and finite element representation for transversely isotropic soft tissues*, The University of Utah, 1994.

White NJ, Pukrittayakamee S, Hien TT, Faiz MA, Mokuolu OA, Dondorp AM. *Malaria*. The Lancet 2014, **383**(9918): 723-35.

Ye T, Phan-Thien N, Lim CT. *Particle-based simulations of red blood cells—A review*. Journal of biomechanics 2016, **49**(11): 2255-66.

Zhang Z, Zhang X. *Mechanical behavior of the erythrocyte in microvessel stenosis*. Science China Life Sciences 2011, **54**(5): 450-8.

Zuccala ES, Baum J. *Cytoskeletal and membrane remodelling during malaria parasite invasion of the human erythrocyte*. British Journal of Haematology 2011, **154**(6): 680-9.

Zuccala ES, Satchwell TJ, Angrisano F, Tan YH, Wilson MC, Heesom KJ, Baum J. *Quantitative phospho-proteomics reveals the Plasmodium merozoite triggers pre-invasion host kinase modification of the red cell cytoskeleton*. Scientific Reports 2016, **6**: 19766.

# Appendix A: Supplementary data for chapter 3

The figure below belongs to section 3.3.1

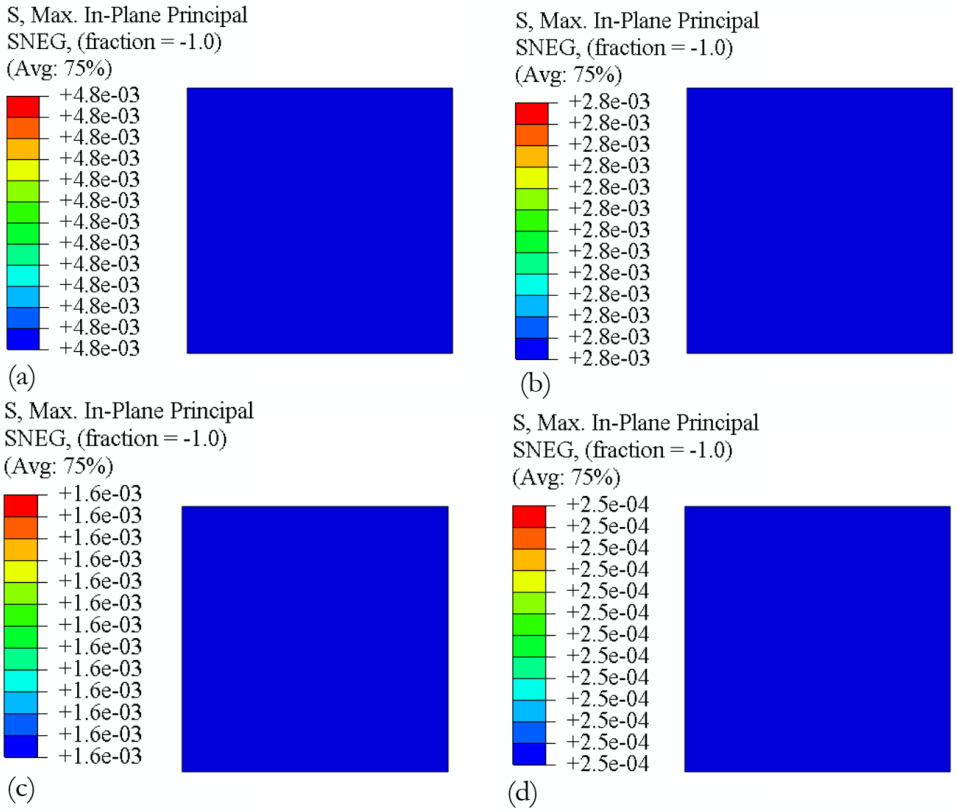


Figure A.1: Contour plots of maximum principal stress in a shell element without damage i.e $\beta_1 = 0$ (a) and a shell element with increasing damage with $\beta_1 = 0.49$ (b), $\beta_1 = 1$ (c), and $\beta_1 = 2.7$ (d).

The tables below belongs to section 3.3.2, Table A.1 to Table A.3, Table A.4 to Table A.6, Table A.7 to Table A.9, Table A.10 to Table A.12, presents the material parameters for Ogden, Yeah and Reduced polynomial model, when the damage parameter $\beta_1$ is equal to 0, 0.49, 1, and 2.7 respectively. The material parameters for the intact erythrocyte membrane are presented in Table A.13

Table A.1: Material parameters for the Ogden strain energy function of order three, evaluated from the developed damage model nominal stress-strain data when $\beta_1 = 0$.

| I | $\mu_i$ (N/mm$^2$) | $\alpha_i$ | $D_i$ (mm$^2$/N) |
|---|---|---|---|
| 1 | 1.79E-05 | 3.6 | 0 |
| 2 | -1.32E-05 | 4.5 | 0 |
| 3 | 2.3E-04 | -1.17 | 0 |

Table A.2: Material parameters for the Yeoh strain energy function of order three, evaluated from the developed damage model when $\beta_1 = 0$.

| i | $D_i$ (mm$^2$/N) | $C_{10}$ (N/mm$^2$) | $C_{20}$ (N / mm$^2$) | $C_{30}$ (N/mm$^2$) |
|---|---|---|---|---|
| 1 | 0 | 1.32E-04 | | |
| 2 | 0 | | 1.25E-05 | |
| 3 | 0 | | | -3.7E-07 |

Table A.3: Material parameters for the Reduced polynomial strain energy function of order six, evaluated from the developed damage model when $\beta_1 = 0$.

| $C_{10}$ (N/mm$^2$) | $C_{20}$ (N/mm$^2$) | $C_{30}$ (N/mm$^2$) | $C_{40}$ (N/mm$^2$) | $C_{50}$ (N/mm$^2$) | $C_{60}$ (N/mm$^2$) |
|---|---|---|---|---|---|
| 1.24E-04 | 3.23E-05 | -5.8E-06 | 5.9E-07 | -3E-08 | 5.95E-10 |

Additional material parameters for the reduced polynomial model are $D_1 = D_2 = D_3 = D_4 = D_5 = D_6 = 0$.

Table A.4: Material parameters for the Ogden strain energy function of order three, evaluated from the developed damage model when $\beta_1 = 0.49$.

| i | $\mu_i$ (N/mm$^2$) | $\alpha_i$ | $D_i$ (mm$^2$/N) |
|---|---|---|---|
| 1 | 5.1E-05 | 2.87 | 0 |
| 2 | -1.4E-09 | 13.4 | 0 |
| 3 | 1.7E-04 | -0.88 | 0 |

Table A.5: Material parameters for the Yeoh strain energy function of order three, evaluated from the developed damage model when $\beta_1 = 0.49$.

| i | $D_i$ (mm$^2$/N) | $C_{10}$ (N/mm$^2$) | $C_{20}$ (N/mm$^2$) | $C_{30}$ (N/mm$^2$) |
|---|---|---|---|---|
| 1 | 0 | 1.2E-04 | | |
| 2 | 0 | | 7.4E-06 | |
| 3 | 0 | | | -2.8E-07 |

Table A.6: Material parameters for the reduced polynomial strain energy function of order six, evaluated from the developed damage model when $\beta_1 = 0.49$.

| $C_{10}$ (N/mm$^2$ ) | $C_{20}$ (N/mm$^2$) | $C_{30}$ (N/mm$^2$) | $C_{40}$ (N/mm$^2$) | $C_{50}$ (N/mm$^2$) | $C_{60}$ (N/mm$^2$) |
|---|---|---|---|---|---|
| 1.17E-04 | 1.8E-05 | -2.9E-06 | 2.5E-07 | -1.1E-08 | 1.7E-10 |

Additional material constants for the reduced polynomial model, $D_1 = D_2 = D_3 = D_4 = D_5 = D_6 = 0$.

Table A.7: Material parameters for the Ogden strain energy function of order three, evaluated from the developed damage model when $\beta_1 = 1$.

| i | $\mu_i$ (N/mm$^2$) | $\alpha_i$ | $D_i$ (mm$^2$/N) |
|---|---|---|---|
| 1 | 1.02E-04 | 2.31 | 0 |
| 2 | -1.5E-10 | 15.7 | 0 |
| 3 | 1.1E-04 | -0.56 | 0 |

Table A.8: Material parameters for the Yeoh strain energy function of order three, evaluated from the developed damage model when $\beta_1 = 1$.

| i | $D_i$ (mm$^2$/N) | $C_{10}$ (N/mm$^2$) | $C_{20}$ (N/mm$^2$) | $C_{30}$ (N/mm$^2$) |
|---|---|---|---|---|
| 1 | 0 | 1.2E-04 | | |
| 2 | 0 | | 3.5E-06 | |
| 3 | 0 | | | -1.8E-07 |

Table A.9: Material parameters for the reduced polynomial strain energy function of order six, evaluated from the developed damage model when $\beta_1 = 1$.

| $C_{10}$ (N/mm$^2$) | $C_{20}$ (N/mm$^2$) | $C_{30}$ (N/mm$^2$) | $C_{40}$ (N/mm$^2$) | $C_{50}$ (N/mm$^2$) | $C_{60}$ (N/mm$^2$) |
|---|---|---|---|---|---|
| 1.1E-04 | 7.5E-06 | -9.09E-07 | 3.16E-08 | 1.03E-09 | -6.95E-11 |

Additional material parameters for the reduced polynomial model, $D_1 = D_2 = D_3 = D_4 = D_5 = D_6 = 0$.

Table A.10: Material parameters for the Ogden strain energy function of order three, evaluated from the developed damage model when $\beta_1 = 2.7$.

| i | $\mu_i$ (N/mm$^2$) | $\alpha_i$ | $D_i$ (mm$^2$/N) |
|---|---|---|---|
| 1 | 1.17E-04 | 0.63 | 0 |
| 2 | 1.6E-04 | 9.4 | 0 |
| 3 | -8.1E-05 | -4.7 | 0 |

Table A.11: Material parameters for the Yeoh strain energy function of order three, evaluated from the developed damage model when $\beta_1 = 2.7$.

| **i** | **$D_i$ ($mm^2/N$)** | **$C_{10}$ ($N/mm^2$)** | **$C_{20}$ ($N/mm^2$)** | **$C_{30}$ ($N/mm^2$)** |
|---|---|---|---|---|
| 1 | 0 | 7.72E-05 | | |
| 2 | 0 | | -2.1E-06 | |
| 3 | 0 | | | 2.8E-09 |

Table A.12: Material parameters for the reduced polynomial strain energy function of order six, evaluated from the developed damage model when $\beta_1 = 2.7$.

| **$C_{10}$ ($N/mm^2$)** | **$C_{20}$ ($N/mm^2$)** | **$C_{30}$ ($N/mm^2$)** | **$C_{40}$ ($N/mm^2$)** | **$C_{50}$ ($N/mm^2$)** | **$C_{60}$ ($N/mm^2$)** |
|---|---|---|---|---|---|
| 8.5E-05 | -1.0E-05 | -1.98E-06 | -2.27E-07 | 1.25E-08 | -2.63E-10 |

Additional material parameters for the reduced polynomial model, $D_1 = D_2 = D_3 = D_4 = D_5 = D_6 = 0$.

Table A.13: The material parameters of an intact erythrocyte membrane

| **$D_1$ ($mm^2/N$)** | **$C_{10}$ ($\mu N/mm^2$)** | **$C_{01}$ ($\mu N/mm^2$)** | **$\beta_1$** |
|---|---|---|---|
| 12 | 152 | 15.2 | 0 |